Calhoun: The NPS Institutional Archive

DSpace Repository

NPS Scholarship Theses

2024-03

METHODS FOR IMPROVING THE PERFORMANCE OF OUTDOOR VISIBLE LIGHT COMMUNICATION FOR LOW-COST VEHICULAR APPLICATIO

Barber, Don E., Jr.

Monterey, CA; Naval Postgraduate School

https://hdl.handle.net/10945/72676

This publication is a work of the U.S. Government as defined in Title 17, United States Code, Section 101. Copyright protection is not available for this work in the United States.

Downloaded from NPS Archive: Calhoun

Calhoun is the Naval Postgraduate School's public access digital repository for research materials and institutional publications created by the NPS community. Calhoun is named for Professor of Mathematics Guy K. Calhoun, NPS's first appointed -- and published -- scholarly author.

Dudley Knox Library / Naval Postgraduate School
411 Dyer Road / 1 University Circle
Monterey, California USA 93943

http://www.nps.edu/library

NAVAL POSTGRADUATE SCHOOL

MONTEREY, CALIFORNIA

DISSERTATION

METHODS FOR IMPROVING THE PERFORMANCE OF OUTDOOR VISIBLE LIGHT COMMUNICATION FOR LOW-COST VEHICULAR APPLICATIONS

by

Don E. Barber Jr.

March 2024

Dissertation Supervisors: John C. McEachen
Murali Tummala

Approved for public release. Distribution is unlimited.

THIS PAGE INTENTIONALLY LEFT BLANK

REPORT DOCUMENTATION PAGE

Form Approved OMB
No. 0704-0188

Public reporting burden for this collection of information is estimated to average 1 hour per response, including the time for reviewing instruction, searching existing data sources, gathering and maintaining the data needed, and completing and reviewing the collection of information. Send comments regarding this burden estimate or any other aspect of this collection of information, including suggestions for reducing this burden, to Washington headquarters Services, Directorate for Information Operations and Reports, 1215 Jefferson Davis Highway, Suite 1204, Arlington, VA 22202-4302, and to the Office of Management and Budget, Paperwork Reduction Project (0704-0188) Washington, DC, 20503.

1. AGENCY USE ONLY ***(Leave blank)***	**2. REPORT DATE** March 2024	**3. REPORT TYPE AND DATES COVERED** Dissertation

4. TITLE AND SUBTITLE
METHODS FOR IMPROVING THE PERFORMANCE OF OUTDOOR VISIBLE LIGHT COMMUNICATION FOR LOW-COST VEHICULAR APPLICATIONS

5. FUNDING NUMBERS
REKRG

6. AUTHOR(S) Don E. Barber Jr.

7. PERFORMING ORGANIZATION NAME(S) AND ADDRESS(ES)
Naval Postgraduate School
Monterey, CA 93943-5000

8. PERFORMING ORGANIZATION REPORT NUMBER

9. SPONSORING / MONITORING AGENCY NAME(S) AND ADDRESS(ES)
Naval Cyber Warfare Development Group, Suitland, MD

10. SPONSORING / MONITORING AGENCY REPORT NUMBER

11. SUPPLEMENTARY NOTES The views expressed in this thesis are those of the author and do not reflect the official policy or position of the Department of Defense or the U.S. Government.

12a. DISTRIBUTION / AVAILABILITY STATEMENT
Approved for public release. Distribution is unlimited.

12b. DISTRIBUTION CODE
A

13. ABSTRACT (maximum 200 words)

Visible light communication reuses illumination fixtures to communicate, augmenting wireless communications in congested radio frequency bands. Vehicular applications could increase safety and efficiency in transportation systems but must compete with strong background noise from daylight. This dissertation investigates means to mitigate solar noise and increase the received signal-to-noise ratio for outdoor visible light communication systems using low-cost cameras and vehicle headlights. We establish a statistical model of daylight noise from empirical measurements captured across a full solar day. Various techniques to improve received signal performance are tested, including the use of spectral and polarization filters, optics, and digital processing techniques for region of interest selection and multi-receiver aggregation. We find attenuating filters help combat quantization noise in bright scenes. Polarization filtering provides selective gain by rejecting background light more than the signal. Using optics, data transmissions at 1.6 km were achieved from a car LED headlight to a smartphone camera as a receiver—four times farther than other outdoor visible light communication in the literature. Demonstrated signal-to-noise ratio enhancements allow improved performance in speed and range for all outdoor visible light communication systems being developed, supporting progress toward safer roadways, lower costs, and reduced radio frequency crowding.

14. SUBJECT TERMS
visible light communication, intelligent transportation systems, array gain, noise mitigation, solar irradiance

15. NUMBER OF PAGES
199

16. PRICE CODE

17. SECURITY CLASSIFICATION OF REPORT Unclassified	**18. SECURITY CLASSIFICATION OF THIS PAGE** Unclassified	**19. SECURITY CLASSIFICATION OF ABSTRACT** Unclassified	**20. LIMITATION OF ABSTRACT** UU

NSN 7540-01-280-5500

Standard Form 298 (Rev. 2-89)
Prescribed by ANSI Std. 239-18

THIS PAGE INTENTIONALLY LEFT BLANK

Approved for public release. Distribution is unlimited.

METHODS FOR IMPROVING THE PERFORMANCE OF OUTDOOR VISIBLE LIGHT COMMUNICATION FOR LOW-COST VEHICULAR APPLICATIONS

Don E. Barber Jr.
Commander, United States Navy
BS, United States Naval Academy, 2004
MS, Electrical Engineering, Naval Postgraduate School, 2009

Submitted in partial fulfillment of the
requirements for the degree of

DOCTOR OF PHILOSOPHY IN ELECTRICAL ENGINEERING

from the

NAVAL POSTGRADUATE SCHOOL
March 2024

Approved by: John C. McEachen
Department of Electrical
and Computer Engineering
Dissertation Supervisor
Dissertation Chair

Murali Tummala
Department of Electrical
and Computer Engineering
Dissertation Supervisor

Chad A. Bollmann
Department of Electrical
and Computer Engineering

Keith R. Cohn
Department of Physics

Owens Walker, USNA

Approved by: Douglas J. Fouts
Chair, Department of Electrical and Computer Engineering

James B. Michael
Vice Provost of Academic Affairs

THIS PAGE INTENTIONALLY LEFT BLANK

ABSTRACT

Visible light communication reuses illumination fixtures to communicate, augmenting wireless communications in congested radio frequency bands. Vehicular applications could increase safety and efficiency in transportation systems but must compete with strong background noise from daylight. This dissertation investigates means to mitigate solar noise and increase the received signal-to-noise ratio for outdoor visible light communication systems using low-cost cameras and vehicle headlights. We establish a statistical model of daylight noise from empirical measurements captured across a full solar day. Various techniques to improve received signal performance are tested, including the use of spectral and polarization filters, optics, and digital processing techniques for region of interest selection and multi-receiver aggregation. We find attenuating filters help combat quantization noise in bright scenes. Polarization filtering provides selective gain by rejecting background light more than the signal. Using optics, data transmissions at 1.6 km were achieved from a car LED headlight to a smartphone camera as a receiver—four times farther than other outdoor visible light communication in the literature. Demonstrated signal-to-noise ratio enhancements allow improved performance in speed and range for all outdoor visible light communication systems being developed, supporting progress toward safer roadways, lower costs, and reduced radio frequency crowding.

THIS PAGE INTENTIONALLY LEFT BLANK

Table of Contents

List of Figures

List of Tables

THIS PAGE INTENTIONALLY LEFT BLANK

List of Acronyms and Abbreviations

API	application programming interface
AWGN	additive white Gaussian noise
BER	bit error rate
CAD	computer aided design
CCD	charge coupled device
CFA	color filter array
CIE	International Commission on Illumination (Commission intertnationale de l'eclairage)
CMOS	complementary metal oxide semiconductor
CRI	color rendering index
DC	direct current
DFT	discrete Fourier transform
DMX	digital multiplex
DSNU	dark signal non-uniformity
FOV	field of view
FPS	frames per second
FSK	frequency shift keying
FSOC	free space optical communications
GPIO	general purpose input/output
IMDD	intensity modulation, direct detection
IR	infrared
ISI	inter-symbol interference
ITS	intelligent transportation system
LED	light emitting diode

LiFi	light-fidelity
LOS	line of sight
MIMO	multiple input, multiple output
OCC	optical camera communication
OFDM	orthogonal frequency division multiplexing
OOK	on-off keying
PC	phosphor coated
PCB	printed circuit board
PDF	probability density function
PLA	polylactic acid
PRNU	photo response non-uniformity
PSD	power spectral density
PWM	pulse width modulation
QAM	quadrature amplitude modulation
RF	radio frequency
ROI	region of interest
SNR	signal-to-noise ratio
SQNR	signal-to-quantization-noise ratio
V2V	vehicle-to-vehicle
V2X	vehicle-to-everything
VLC	visible light communication
VVLC	vehicular visible light communication
WAVE	wireless access in vehicular environment
WiFi	wireless-fidelity
USB	universal serial bus
USFOOK	undersampled frequency on-off keying
UV	ultraviolet

Executive Summary

Visible light communication (VLC) reuses illumination fixtures to communicate, augmenting wireless communications in congested radio frequency bands. VLC has great potential for vehicular applications but must contend with tremendous amounts of ambient background light. Over the past year, several papers have demonstrated vehicle-to-vehicle communication, using visible light as a control channel to enhance radio frequency communications [1] and even sending data directly via existing vehicle lights [2]. This dissertation explores means of mitigating background noise to boost the received signal-to-noise ratio (SNR), enhancing these cutting-edge applications of VLC.

Improved range, robustness, and data rates are overarching goals for enabling vehicle-to-vehicle communication. Rather than increasing transmitted signal power, we focus on noise mitigation as a primary technique to increase SNR and enable greater communication distances. Some literature ascribes a maximum feasible range for outdoor LED-based visible light communication of around 125 m [3]–[5]. Greater distances have been achieved outdoors, but not with the direct aim of vehicular application. The farthest we are aware of is a 400 m visible light communication system, using a commodity camera sensor and telescope [6].

Focusing on noise mitigation, this dissertation addresses the critical gap of improving range and robustness in outdoor settings while avoiding any distraction to vehicle operators. Achieving sufficient SNR allows communication at longer distances and offers the potential to employ modulation schemes transmitting more bits in less time. However, visible light communication constraints — both minimizing distraction and ensuring eye safety — preclude simply increasing transmit power to increase SNR. This dissertation addresses how to mitigate noise in daylight to increase overall SNR for outdoor vehicular visible light communication. Increasing SNR allows for improved utilization of all the existing research on visible light communication waveforms and geometries.

An overview of a basic VLC channel and the SNR improvement techniques that this dissertation explores is shown in Figure 1. A VLC transmission from a car headlight or taillight is degraded through spreading losses, atmospheric attenuation, and additive noise before reaching the receiver. With a goal of utilizing existing vehicle lights, we focus on noise reduction at the receiver to improve SNR. The use of optical filters and magnification in conjunction with a low-cost, commodity complementary metal-oxide semiconductor (CMOS) sensors is explored. Leveraging the CMOS pixel matrix, spatial selectivity to optimize SNR and the integration of scenes from two separate cameras is also investigated. Attenuation is found to reduce quantization noise in many outdoor scenarios, polarization filters selectively suppress noise increasing SNR in all cases, and multi-pixel array again, using magnification at long distances, allowed communication at 1.6 km.

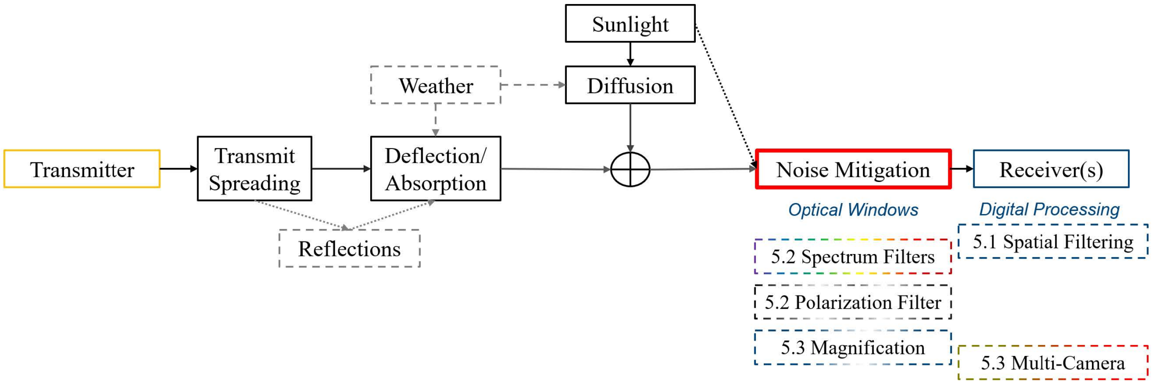

Figure 1. Basic channel model including transmitter, channel impacts, and receiver. Noise mitigation techniques including optics, filters, and processing are assessed.

Modeling Daylight Noise

A key challenge for outdoor VLC is the sheer amount of solar noise present in the background. As an intuitive example of the challenge of detecting subtle lights during the day, the stars are always shining, but it is nearly impossible to see them during the day. To improve SNR by reducing noise, we begin by establishing a statistical model of daylight noise from measurements captured across a full solar day. The Sony IMX363 EXMOR RS was used as an exemplar CMOS camera sensor. It has a broad market share and is used in the Pixel 3, Pixel 4, Pixel 5, and Pixel 6 lines. Our test devices are Pixel 6a camera phones. Using this sensor, a static target was recorded to establish a noise baseline. Recordings were taken hourly over a single day, from 0700 to 2100. Throughout the day, the location of the black and white target and camera remained constant, while sun angle and intensity varied from early morning through solar noon and into civil twilight.

Observing black and white areas on the target, average output values are consistent over the day, despite significant variation in overall scene luminance. White areas on the target typically have a quantized output of around 225 (out of 255) throughout daylight hours. Conversely, black pixels have an average value of around 70. As expected, black pixels are significantly darker. However, when assessing noise power — that is how much pixel values moved up and down despite no actual change in the scene — black pixels have nearly twice as much noise as white pixels.

Testing Signal-to-Noise Ratio Improvements

While photodiodes are used as receivers in 88% of VLC research [4], we focus on CMOS cameras as receivers — like those already available in many cars for lane-assistance and backup functions. For transmission, we also leveraged vehicle lighting fixtures, with an LED headlight bulb in a headlight housing modulated by an Arduino microcontroller.

Various techniques to improve received signal performance were tested, including the use of spectral and polarization filters, optics, and digital processing techniques for region-of-interest selection and multi-receiver aggregation. We found attenuating filters help combat quantization noise in bright scenes. Polarization filtering provides additional selective gain by rejecting background light more than the signal. Using compact optics, we achieved data transmissions at 1.6 km from an LED car headlight to a smartphone camera receiver — four times farther than other outdoor visible light communication in the literature. Figure 2 shows the receiving Pixel 6a camera phone mounted on a tripod, the transmitting headlight, and the geometry of our longest-range test.

Figure 2. Overview of components used in experimentation, including the receiving Pixel 6a camera phone mounted on a tripod, the geometry of the 1650 m test over Monterey Bay, and the transmitting LED headlight. Adapted from [7].

Based on the results of data collection, the dominant factors impacting SNR — and in turn achievable range of an outdoor VLC system — were validated. In daylight, internal camera noise is negligibly small, and atmospheric attenuation is dramatically lower than other range-driven loss factors. Both noise components can be simplified from engineering approximations. The most significant parameters enabling greater SNR are pixel fill and relative scene brightness. At moderate ranges, averaging across more pixels provides gain compensating for inverse squared losses. At a long range, 1.6 km, optical magnification allows multi-pixel array gain to lift the signal out of the noise floor, increasing SNR by nearly 13 dB. We also found that signal-to-quantization-noise decreases proportionally to the ratio of signal versus scene brightness. When the received signal is clipped by the upper quantization bound, the use of filters to attenuate the received signal increases the granularity of quantization bins, increasing the received SNR.

Findings and Contributions

With an understanding of the noise contending with VLC signals in an outdoor environment, we tested numerous methods of improving received SNR via filtering and processing at the receiver. We leveraged the types of fixtures most likely to be ubiquitously deployed on vehicles since maintaining low cost will be critical to reaching the market saturation needed to allow all vehicles to intercommunicate. Working toward outdoor VLC with commodity hardware, our contributions include:

1. Collection of a baseline quantifying noise across an entire day.
2. Discovery of performance gains employing polarization filtering.
3. Successful VLC at an unprecedented range of 1.6 km.
4. Identification of key performance enhancements for SNR in outdoor VLC systems.

Future work toward vehicular VLC in intelligent transportation systems will involve marrying these enhancements with the system design and the development of standardized communication protocols for interoperability. Demonstrated SNR enhancements will improve the speed and range for all outdoor visible light communication systems being developed in current research, moving toward safer roadways, lower costs, and reduced radio frequency crowding.

List of References

[1] N. Okasha, A. Zekry, and F. Newagy, "Car To Car Communication Using RF Cognitive Radio with VLC Common Control Channel," In Review, preprint, July 2023. Available: https://doi.org/10.21203/rs.3.rs-3196449/v1

[2] M. Plattner and G. Ostermayer, "Camera-based Vehicle-to-Vehicle Visible Light Communication - A Software-Only Solution for Vehicle Manufacturers Camera-based Vehicle-to-Vehicle Visible Light Communication - A Software-Only Solution for Vehicle Manufacturers," in *2023 32nd International Conference on Computer Communications and Networks (ICCCN)*. Honolulu, HI, USA: IEEE, July 2023, pp. 1–7. Available: https://doi.org/10.1109/ICCCN58024.2023.10230125

[3] L. E. M. Matheus, A. B. Vieira, L. F. M. Vieira, M. A. M. Vieira, and O. Gnawali, "Visible Light Communication: Concepts, Applications and Challenges," *IEEE Communications Surveys & Tutorials*, vol. 21, no. 4, pp. 3204–3237, 2019. Available: https://doi.org/10.1109/COMST.2019.2913348

[4] R. Huang and T. Yamazato, "A Review on Image Sensor Communication and Its Applications to Vehicles," *Photonics*, vol. 10, no. 6, p. 617, May 2023. Available: https://doi.org/10.3390/photonics10060617

[5] E. El-Mokadem, N. Tawfik, M. H. Aly, and W. El-Deeb, “Design and performance evaluation of vehicular visible light communication system under different weather conditions and system parameters,” *Opto-Electronics Review*, Apr. 2023. Available: https://doi.org/10.24425/opelre.2023.145580

[6] E. Eso, S. Teli, N. Bani Hassan, S. Vitek, Z. Ghassemlooy, and S. Zvanovec, “400 m rolling-shutter-based optical camera communications link,” *Optics Letters*, vol. 45, no. 5, p. 1059, Mar. 2020. Available: https://doi.org/10.1364/OL.385423

[7] “Google maps.” Imagery ©2023 AMBAG, Airbus, Data CSUMB SFML, CA OPC, Maxar Technologies, USA/FPAC/GEO. https://www.google.com/maps/place/Naval+Postgraduate+School/@36.6103149,-121.8889425,4460m/ (accessed Sep. 27, 2023).

CHAPTER 1:
Introduction

Visible light communication (VLC) has great potential for vehicular applications but must contend with tremendous amounts of ambient background light. Low data rate optical camera communication (OCC), a subset of VLC using commodity optical cameras for light communication, was first proposed for vehicular applications in 2017 [1]. Over the past year, several papers have demonstrated vehicle-to-vehicle (V2V) communications using VLC as a control channel to enhance radio frequency (RF) communications [2] and even communicate sending data via existing vehicle lights [3], [4]. This dissertation explores methods of mitigating background noise to boost received signal-to-noise ratio (SNR). We use SNR as our metric for increased performance, which informs the potential to enhance cutting-edge applications of VLC. Higher SNR enables all communication system implementations to provide faster, more robust data transmission.

We achieve outdoor VLC data throughput with commodity hardware at unprecedented distances. Expanding on current literature, we provide a measured baseline of daylight background noise across an entire day. Moving beyond blue filters, we explore a range of possible other spectral improvements and provide new insights employing the first known polarization filtering in conjunction with vehicular visible light communication (VVLC). Incorporating the results of experimental data, we establish bounds for practical OCC systems using existing fixtures in vehicles.

1.1 Intelligent Transportation Systems

An intelligent transportation system (ITS) uses computing algorithms informed by communications among vehicles and infrastructure to manage and direct resources. Growing demands on limited transportation infrastructure are driving the development of ITSs to increase both safety and efficiency for vehicular traffic. The case for V2V communication was emphatically laid out by the NHTSA [5], estimating V2V communications will “prevent hundreds of thousands of crashes and prevent over one thousand fatalities annually.” ITSs are a necessity of future transportation. Road traffic fatalities are the eighth leading cause of death worldwide and the number one cause of death in children over five years of age and adults under 30 [6]. Transportation infrastructure is increasingly congested and the ability to simply build more roads has reached an impasse. At the same time, growing awareness of climate challenges requires more efficient use of automotive energy resources.

An ITS has many advantages, including improving safety and helping to manage traffic flow while minimizing emissions. Late-model cars can sense the distance to the vehicle immediately in front of them, enabling adaptive cruise control and emergency braking. Moving beyond that, vehicles proactively communicating about their own speed and braking, as well as traffic conditions and the acceleration of vehicles farther down the road will enable driver assistance to optimize fuel consumption and better manage safety margins. Feasibility studies for ITSs have been ongoing globally since the 1980s, with product development rapidly advancing alongside other computer and communication technologies from the late 1990s to the present [7]. The U.S. Department of Transportation has established a program office for ITSs, which touts preliminary experiments increasing per passenger revenue, reduced winter weather accidents, and reduced environmental impacts at intersections [8].

Supporting any ITS, communications among vehicles and transportation infrastructure are essential. The NHTSA proposal suggests the use of dedicated short-range RF communications [5], in line with the IEEE 802.11p standard for wireless access in vehicular environment (WAVE), initially approved in 2010. 802.11p builds on previous wireless-fidelity (WiFi) with adaptions for increased delay spread in vehicular applications [9]. V2V communication techniques proposed in the IEEE 802.11P standard [10] and by the U.S. Department of Transportation [8] specify the use of radio frequency (RF) communications in the 5 GHz range. This is a proven and cost-effective solution but faces challenges with congestion in the RF environment.

Beyond the financial costs associated with licensing RF bands, the proliferation of smart and connected devices has led to a scarcity of RF spectrum to support communication. In areas of congested vehicle traffic, many users competing for the same set of channels will cause congestion. Congestion causes backups reducing throughput, similar to the throughput loss in heavily loaded WiFi networks [11]. Recent advances in vehicle headlight technology suggest a low-cost alternative for V2V communication.

1.2 Spectrum Availability and Visible Light

While RF is a well-understood and ubiquitous means of communication, much like road systems, the RF spectrum has become saturated. VVLC provide a means of complementing RF communications, limiting RF congestion and automatically prioritize adjacent vehicles due to the line of sight (LOS) propagation characteristics. VLC has been specifically included in recent proposals for vehicular communications to prevent accidents [12].

As the RF spectrum continues to become more congested, demand for bandwidth has continued to push communications to higher frequencies even in purely RF systems. A major technological innovation of 5G cellular technology was to expand into a new frequency band above 24 GHz [13]. Developing future 6G networks, terahertz frequencies are already being considered to overcome the data rate limits in the 5G millimeter wave band [14]. As demands on the spectrum continue to grow, including an ever-increasing number of connected personal devices and linked intelligent systems, the frontier of viable frequencies continues to climb higher — to include visible light. Numerous heterogeneous RF and VLC systems have been proposed in just the last year [15]–[18].

VVLC could complement RF communication, reducing RF congestion and providing a prioritized communications path for adjacent vehicles. In typical usage, RF networks — like WiFi — experience performance degradation as more users try to communicate on the network. In a congested traffic scenario, dozens or more vehicles could be in close proximity, creating congestion in RF V2V networks. This design constraint was considered in RF development, with an eye toward minimizing message sizes [11]. Unlike omnidirectional 5 GHz RF signals that are received by any antenna in range, the strong line of sight characteristics of the visible light spectrum allow imaging sensors to isolate and prioritize signals with a direct line of sight while rejecting cochannel interference from other V2V communications. While not targeted at WAVE specifically, IEEE 802.15.7 defines standards for short-range optical wireless communications [19] that have been tested for vehicle-to-everything (V2X) applications at ranges up to 50 m [20].

Over the last two decades, light fixtures have been rapidly shifting from incandescent to light emitting diode (LED) technology due to the tremendous energy efficiency advantages of LEDs. The shift from heated filaments and energized gasses to LEDs offers many practical advantages in power and weight savings. LED lights also enable rapid digital modulation, allowing data to be encoded in visible light. The concept of modulating LED lights to provide simultaneous dual use for illumination as well as data transmission arose at the turn of the century [21]. Standards to leverage this opportunity have been established in IEEE 802.15.7 [19], 802.11bb [22] and the commercial light-fidelity (LiFi) standard [23].

There is a growing body of research highlighting the value of leveraging the visible light spectrum for communication [24]. Using the visible spectrum rather than RF for communications offers the potential for cost savings not having to compete for expensive licensed communication bands. Currently, the U.S. FCC has only allocated frequencies up to 275 GHz for all terrestrial and space radio communications [25]. At a width of over 300 THz, the visible light band is over 1000 times as wide as all allocated RF frequencies. The capacity of a communication channel is determined by bandwidth and, at light frequencies, bandwidth is plentiful. Further, cost savings can be achieved by repurposing existing light fixtures to not only provide illumination but also transmit data. Plentiful emitters already exist in the environment, ranging from basic overhead lights to ubiquitous screens.

In the development of the vast majority of VLC systems, including LiFi, data transmission is limited to an indoor environment. Indoor applications of VLC have many advantages. They do not interfere with other RF-sensitive electronics, they provide security by being well confined within the walls of a space, and they make dual use of existing illumination fixtures to save on infrastructure and energy costs. With the right design characteristics, encoding data into these sources allows enhanced efficiency, fulfilling the intended purpose of illumination while also transmitting digital data. Broad research is ongoing to employ more advanced modulation techniques, such as orthogonal frequency division multiplexing (OFDM), to deliver higher bandwidth via VLC. OFDM-VLC have been demonstrated above 3.5 Gb/s at 3.5 m [26]. Even optical multiple input, multiple output (MIMO) has begun to be explored in controlled indoor settings [27]. While the rich body of research and techniques for indoor VLC have valuable applications, the indoor environment has very low background brightness and relatively short propagation distances compared to outdoor applications.

1.3 Daylight Noise Mitigation

There is a clear need for ITSs to increase the safety and efficiency of our transportation systems. As the RF spectrum has become congested, VVLC offers a means to complement it, better enabling ITS. However, despite the promise of VLC, there are significant challenges to its implementation outdoors. While many studies have touted high-speed VLC, few of them have evaluated its use outdoors, and even fewer at ranges relevant to enabling VVLC. In a survey of VVLC challenges, Căilean and Dimian [28] identified seven overarching challenges, foremost including increasing robustness to noise and increasing communication ranges.

The extensive research studying indoor VLC and LiFi has addressed detectability and high data rates in ways that are generally not robust enough to operate in daylight, especially at long distances. Any communication channel is limited by the SNR [29], which becomes the driving design constraint for any outdoor VLC system. Environmental noise is orders of magnitude higher in daylight conditions. As an intuitive example of the challenges of observing subtleties in visible light, the stars are always shining, but it is nearly impossible to see them during the day. Căilean and Diminan's survey of VLC found that "despite being an active research area, the outdoor VLC applications, in general, and vehicular VLC applications, in particular, attracted a smaller research effort compared to indoor VLC applications" [28].

With significantly more noise and greater distances, the application of VLC to outdoor and inter-vehicle communication remains an active research area. VLC with commodity cameras rather than photodiodes — also sometimes called OCC — represents only a small fraction of ongoing VLC research [30]. Focusing on noise mitigation, this dissertation addresses the critical gap of improving range and robustness in outdoor settings while minimizing any distraction to vehicle operators. Achieving sufficient SNR allows communication at longer distances and offers the potential to employ modulation schemes transmitting more bits in less time. However, the constraints of VLC — both minimizing distraction and ensuring eye safety — preclude simply increasing transmit power to increase SNR. This dissertation addresses how to mitigate the noise from daylight by shrinking the denominator to increase overall SNR for outdoor VVLC. This approach to improving SNR has broad applicability to other VLC use cases, facilitating improved performance across VLC waveforms and geometries.

1.4 Related Literature

To put this research in context, we briefly touch on some highlights in other existing literature. We focus our research on improving the range and performance of outdoor VLC for vehicular communication using low-cost, commodity sensors and existing lights. Huang and Yamazato conducted a review of vehicular OCC finding only 12% of VLC literature focused on image sensor communication and less than a quarter of that on outdoor applications [30].

As mentioned, recent publications by Plattner and Ostermayer [3], [4] demonstrated a functional V2V system using taillights to transmit data between vehicles. This work affirms that a software-only solution can work with existing light fixtures to transmit data. Our research continues in this vein, focusing on employing existing vehicle lights and low-cost complementary metal oxide semiconductor (CMOS) sensors. While Plattner and Ostermayer tested a functional system out to 60 m, they highlight further distances as out of scope. Similarly, Shen and Tsai demonstrated a V2V test case using taillights and photodiodes up to 45 m in driving scenarios [31]. Building on these proven foundations, this dissertation further investigates techniques to improve SNR and increase communication range with existing vehicular hardware.

Some literature ascribes a maximum feasible range for outdoor LED-based VLC of around 125 m [30], [32], [33]. Greater distances have been achieved, but not with a direct aim of vehicular application. Eso et al. [34] demonstrated a 400 m visible light communication system using OCC. They noted the longer exposure time and larger overall photosensitive area of a CMOS imaging sensor improves SNR. Their paper focused on increased speed at long distances, leveraging a telescope and defocusing the image to fill the sensor, which allows the application of rolling shutter techniques to improve bit rate. We will seek to achieve ranges even greater than 400 m and avoid the use of large telescope-sized optics which would not be conducive to vehicular applications. Rather than defocusing to fill pixels, when we leverage optical magnification we do so to minimize included noise. Seeking to achieve greater ranges, this dissertation remains focused on improving SNR which provides the opportunity for improved speed, greater robustness, or a combination of the two.

Communication in noise has been a perennial challenge from Nyquist's work to Shannon's seminal paper [35]. While the impact of daylight noise has been highlighted in many surveys [28], [32], few papers have made a deliberate effort to find ways to mitigate it. Costanzo et al. attempted to interleave noise sampling and subtraction via signal processing but limited their experiments to 8 m [36]. Islim et al. conducted outdoor experiments employing blue filters [37]. Using photodiodes, they found significant gains using off-the-shelf blue filters. This, and their detailed treatment of solar position, informs our more detailed work across multiple color filters and times of day. In a similar attempt to counter sunlight noise, Eso et al. [38] proposed an infrared (IR) vehicular VLC system, and demonstrated ranges up to 89 m. IR transmitters are outside the scope of this dissertation since modern car lights using LED bulbs produce very little power in the near IR portion of the spectrum.

1.5 Dissertation Outline

The remainder of this dissertation begins, in Chapter 2, by exploring light communications, building to a focus on SNR as a key metric. Chapter 3 then develops a statistical model for the daylight noise that interferes with outdoor VLC, presenting new empirically collected measurements. Having established a noise model, Chapter 4 outlines our experimental method for testing the transmission of visible light signals from an LED headlight to a commodity CMOS camera in daylight conditions at ranges unprecedented in previous literature. The tests and results employing various spatial filtering, spectral and polarization filtering, optical magnification, and multi-receiver configurations are presented in Chapter 5. Chapter 6 provides a quantitative derivation of SNR achieved at increasing ranges and highlights the key parameters influencing system performance grounded in the empirical findings from Chapter 5. Chapter 7 includes our conclusions, highlighting the successes of polarization filtering and the potential for relatively fast transmissions and successful transmissions over 1.6 km.

THIS PAGE INTENTIONALLY LEFT BLANK

CHAPTER 2:
Light Communication

In this chapter, we provide background on the history and application of communicating with visible light, building toward a focus on SNR to improve modern VLC performance. Light communications have ancient roots. From signal fires in ancient Greece and China, they evolved into signal flags and then signal lanterns. New technologies, including lasers and LEDs have enabled faster modulation. In this dissertation, we focus specifically on the application of V2V communication using LED lights in strong background light during the day.

This dissertation focuses on using existing fixtures and low-cost cameras, but we begin by exploring other recent visible light communication techniques — including indoor applications, such as LiFi, to outdoor laser-based communication. These technologies set the stage for further development and highlight the challenges that we face attempting to communicate at greater distances with stronger background noise. We highlight SNR as the key metric for communication performance improvements. Ultimately, the speed and robustness of any modulation scheme is fundamentally limited by SNR as laid out by Shannon in 1948 [29]. We present a brief communications system model and conclude our background work with an overview of SNR.

2.1 Evolution of Systems

Communication in the visible light spectrum has ancient roots and yet still presents new opportunities for cutting-edge technological applications. Before delving deeper into the driving technical parameters specific to V2V applications of VLC, historic context and an overview of other existing light communication systems inform the solution space.

Although ancient fires lacked high data rates and subtlety, historic examples illustrate the value and potential for signaling at long distances. An explosion of research into laser communications half a century ago demonstrated high data rates, but was expensive and very sensitive to alignment and atmospheric issues. More recently, the broad deployment of LED light fixtures has spawned significant interest in indoor VLC. These systems make dual-use of illumination fixtures for communication, saving both hardware cost and RF bandwidth, but are not generally robust to interference present in outdoor environments.

2.1.1 Communicating with Natural Light

The human visual system is highly evolved, capable of collecting color, brightness, and depth information across a huge range of lighting conditions. The perceived visible spectrum consists of wavelengths ranging from approximately 400–700 nm. Visual processing integrates disparate pieces of information over tens of milliseconds to provide a cohesive cognitive representation of still and moving objects in the environment. Sight provides an opportunity to communicate at far greater distances than sound, and people have leveraged the visual spectrum to communicate since the dawn of history.

Communication with visible light in various forms far predates the modern electronic communication revolution. People around the world have relied on basic signal fires for millennia. Primitive signaling fires provided a robust way to rapidly communicate messages over great distances. Requiring neither infrastructure nor messengers, they offer many of the advantages of modern wireless communication, albeit with drastically lower throughput. In the 3rd century B.C.E., the ancient Greeks enhanced visible communication by leveraging multiple torches to convey a set of pre-coordinated messages, rather than solely relying on the binary message of a beacon fire being lit or not [39].

At sea, navies have also relied on communication in the visible spectrum. Ships relied on signal flags to communicate combat maneuvers from ancient fleets through the pivotal Battle of Jutland during the First World War. While the advent of RF communications has overshadowed the predominant role of visible signaling at sea, light communication schemes persist to this day. Not only are signal flags and symbols used on military and civilian craft, but the use of signaling lanterns continues to offer communication via light [40]. Similar to signal fires, shuttered lights flashing Morse code signals offer point-to-point communications from ship to ship while avoiding many of the risks associated with adversaries collecting RF transmissions.

Beyond the above techniques, which relied on human sight to receive messages, there are also historic examples of encoding data in the visible light spectrum, notably including Bell's photo-phone in 1880 [41]. Bell transmitted an audio signal over 200 m by modulating the intensity of light as it reflected off a vibrating membrane. At the receiving end, this modulated light was focused on a selenium crystal, converting changes in light intensity to changes in electrical resistance, allowing the recovery of the source sound.

2.1.2 Laser Communications

As technology evolved through the 20th century, more focused and coherent light sources emerged. Lasers allow selectivity in wavelength and focusing the direction of light transmission. The basic concept of modulating the intensity of light to transmit information, pioneered by Bell using reflected sunlight, continues to underpin most modern optical communications systems, from pulses of light in fiber optic cable to free space optical communications (FSOC). FSOC systems implemented with lasers have fascinating historic and modern applications. During the 1960s, a laser communication transmitter was used on Gemini-7 [42] and NASA has continued laser communications research to provide faster data rates to distance spacecraft. Google's parent company, Alphabet, also developed laser communications to enable Internet access via high-altitude balloons and has pivoted this work to provide terrestrial laser-based Internet backhaul in sub-Saharan Africa [43].

While FSOC provide high data rates at long ranges, they leverage purpose-built hardware and require careful alignment to maintain function. In contrast, a typical infrared remote used to control a television set uses inexpensive infrared diodes in a non-directional manner but achieves only very low data rates. The use of white LEDs for communication networks was proposed at the turn of the century [21] and continuing research seeks to use commodity lighting to achieve high data rates.

2.1.3 Visible Light Communication

While FSOC using lasers provides high data rates at a substantial range, it tends to be expensive and extremely sensitive to alignment and the environment. In the late 1990s, cost-effective white LEDs were introduced and began proliferating as efficient light sources in commercial applications over the next decade [44]. LED bulbs not only produce less waste heat but can be turned on and off much more rapidly than legacy incandescent and halogen bulbs. Modulating LED bulbs provides a way to embed data in light, and research began in earnest in 2007 to take advantage of this capability [45].

Unlike a dedicated laser source in FSOC, VLC takes advantage of existing illumination fixtures to transmit data. Leveraging existing light fixtures to communicate digital data from overhead lights to laptops and cell phones, or even from vehicle headlights to other vehicles, allows us to capture synergies of a shared emitter — saving on power, cost, and space. However, it also introduces new constraints on the channel that were less pronounced in the RF band, most notably including impacts on human perception. The radio waves and the infrared signals from television remotes are invisible to humans. However, flickering visible lights can cause numerous problems from distraction and annoyance to headaches for people in proximity to the light source.

Indoor VLC has continued to innovate to augment WiFi at short ranges in controlled environments but is not robust enough to operate outdoors or at long ranges. This gap informs the direction of our research, investigating ways to capture the low cost and ubiquity of LED lights to more robustly deliver signals amid background optical noise at longer ranges.

2.1.4 Vehicular Visible Light Communication

As VLC has continued to mature, less than a quarter of the research into VLC addresses outdoor applications [30]. Recent research has begun to improve the performance of VLC outdoors. Range results, as summarized in Table 2.1, are in line with our early experimental findings [46], with stable links out to 50 m and distances of 100 m requiring greater error correction coding. Other recent authors have also framed VVLC as being limited to the range of 40–50 m [47]. Of course, FSOC systems using lasers can provide high data rates at long distances, but they are both expensive and demand pointing and stabilization that would be challenging to implement in a V2V environment.

Table 2.1. Outdoor VLC Ranges in the Literature [4], [31], [34], [36]–[38], [46], [48]–[75]

Title	First Author	Year	Distance (m)	Reference
Experimental Outdoor Visible Light Data Communication System Using Differential Decision Threshold with Optical and Color Filters	Kim	2015	0.1	[48]

Continuation of Table 2.1

Title	**First Author**	**Year**	**Distance (m)**	**Reference**
The Impact of Solar Irradiance on Visible Light Communications	Islim	2018	0.14	[37]
Vehicular Visible Light Communications with LED Taillight and Rolling Shutter Camera	Ji	2014	0.4	[49]
Multi-Level Optical Signal Reception by Blur Curved Approximation for Optical Camera Communication	Lee	2017	0.5	[50]
A New Automotive VLC System Using Optical Communication Image Sensor	Goto	2016	1.5	[51]
Efficient Optical Filtering for Outdoor Visible Light Communications in the Presence of Sunlight or Artificial Light	Chung	2013	2	[52]
Performance Evaluation of High-Speed Visible Light Communication Combining Low-Speed Image Sensor and Polygon Mirror in an Outdoor Environment	Imai	2016	4	[53]
Visible Light Communication System Based on Software Defined Radio: Performance Study of Intelligent Transportation and Indoor Applications	Martinek	2019	5.5	[54]
A Noise Mitigation Approach for VLC Systems	Costanzo	2019	8	[36]
Outdoor Visible Light Communication for Inter-Vehicle Communication Using Controller Area Network	Kim	2012	20	[55]
Adaptive Real-Time Speed Limit Broadcasting for Autonomous Driving Applications Using Visible Light Communication	Ghabboun	2023	20	[56]
The Uplink Visible Light Communication Beacon System for Universal Traffic Management	Yamazato	2017	25	[57]
Increasing Vehicular Visible Light Communications Range Based on LED Current Overdriving and Variable Pulse Position Modulation: Concept and Experimental Validation	Beguni	2023	25.2	[58]
Image Sensor Based Visible Light Communication	Haruyama	2015	30	[59]
Demonstration of Vehicular Visible Light Communication Based on LED Headlamp	Yoo	2016	30	[60]
Experimental Demonstration of a Visible Light Communications Crosswalk Assistance System	Beguni	2022	40	[61]
Testing Vehicle-to-Vehicle Visible Light Communications in Real-world Driving Scenarios	Shen	2017	45	[31]
A New Tracking Method Using Image Sensor and Photo Diode for Visible Light Road-to-Vehicle Communication	Saito	2008	48	[62]

Continuation of Table 2.1

Title	**First Author**	**Year**	**Distance (m)**	**Reference**
Average Channel Capacity Bounds of a Dynamic Vehicle-to-Vehicle Visible Light Communication System	Alsalami	2023	49	[63]
Novel Receiver Sensor for Visible Light Communications in Automotive Applications	Căilean	2015	50	[64]
Camera-Based Vehicle-to-Vehicle Visible Light Communication - A Software-Only Solution for Vehicle Manufacturers	Plattner	2023	60	[4]
Image-Sensor-Based Visible Light Communication for Automotive Applications	Yamazato	2014	70	[65]
Detection Algorithm for Overlapping LEDs in Vehicular Visible Light Communication System	Huynh	2019	70	[66]
Fundamental Analysis of Vehicular Light Communications and the Mitigation of Sunlight Noise	Eso	2021	89	[38]
On-Vehicle Receiver for Distant Visible Light Road-to-Vehicle Communication	Okada	2009	100	[67]
Non-Flickering 100 m RGB Visible Light Communication Transmission Based on a CMOS Image Sensor	Chow	2018	100	[68]
Noise Mitigation Using Adaptive Filtering Algorithm for Long-Range VLC System Based on FPGA	Wang	2020	100	[69]
Position-Dependent MIMO Demultiplexing Strategy for High Speed Visible Light Communication	Li	2022	100	[70]
Optical Camera Communication System for Internet of Things Based on Organic Light Emitting Diodes	Chavez-Burbano	2019	120	[71]
A 160 m Visible Light Communication Link Using Hybrid Undersampled Phase-Frequency Shift On-Off Keying and CMOS Image Sensor	Atta	2019	160	[72]
Impacts on Multi-Pulse Pulse Position Modulation Visible Light Communication from Outdoor Daylight Conditions	Barber	2023	192	[46]
Sandstorm Effect on Experimental Optical Camera	Matus	2021	200	[73]
Optical Camera Communication for Smart Cities	Chavez-Burbano	2017	328	[74]
400 m Rolling-Shutter-Based Optical Camera Communications Link	Eso	2020	400	[34]
550 m Low Power Outdoor Visible Light Communication System Using Polarized Light	Barber	2023	550	[75]

End of Table

The longest reported range for any other author's outdoor VLC system was 400 m, achieved by employing a telescope and defocusing of the lens to fill the imaging sensor [34]. This result set an upper bound on ranges in the literature, the majority of which are less than 50 m. However, to achieve this range, they used a very bright LED (approximately 72 W, which would output luminance in the range of a 150 W high-pressure sodium lamp or 400 W incandescent) and constrained field of view (FOV) similar to a FSOC system. The 328 m results in [74] were similarly impressive, using fewer optics but transmitting from a colored 48 cm × 48 cm LED array. In all systems, performance declined with increasing range as inverse-square losses reduced received power and using more initial transmit power improved performance.

2.2 Challenges

Building toward V2V light communications, several design constraints must be balanced, including range, cost, and throughput. In Figure 2.1, laser-based FSOC, (a), provides high data rates at multiple kilometers, but requires dedicated hardware and precise alignment. At the other end of the spectrum, indoor VLC, (c), supports higher data rates without precise alignment but is range-constrained and limited by interference. Somewhere in the middle, outdoor VLC to enable ITS, (b), must offer a wide FOV, reasonable range, and robust performance with strong background light. In designing an outdoor VVLC system, extremely high data rates are not necessarily required. The goal of an ITS is not backhaul or content distribution and messages can be short to allow timely transmission at lower data rates and longer ranges [11].

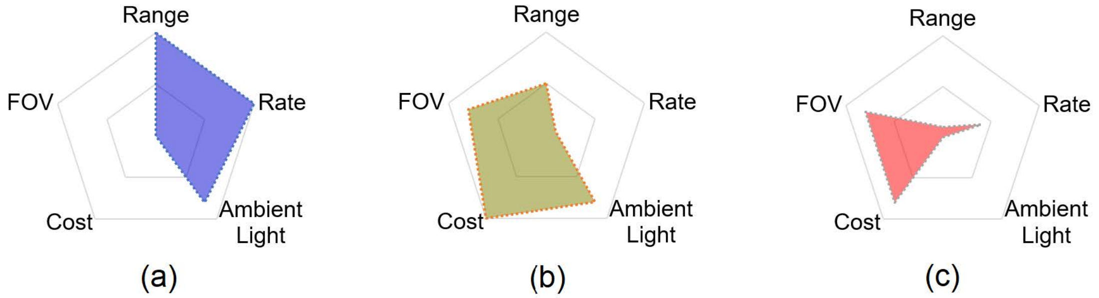

Figure 2.1. Comparison of attributes for (a) FSOC, (b) V2V, and (c) indoor VLC systems

Many of the parameters associated with the transmitter and channel may be outside the control of the system designer (limited by VLC constraints or nature itself), so we focus on noise mitigation techniques at the receiver. Increasing robustness to noise and increasing communication ranges have been identified as top challenges for VVLC [28], [32].

The engineering trade space requires balancing competing objectives. Many of these trade-offs — balancing FOV, more efficient detectors, and wavelength selectivity — have been assessed for VVLC [58]. Narrower bandwidths and specific colors make it easier to use filters to separate the signal from other noise, and the use of laser diodes instead of LEDs has been shown to more than double the achievable communication range [33]. However, lasers preempt the reuse of existing illumination fixtures to save on cost, size, weight, and power. Faster cameras and photodiodes can receive shorter symbols, but the use of commodity cameras supports dual utilization of receivers in the vehicle. While only a small fraction of VLC research, recently OCC has garnered interest as a pragmatic, low-cost option [30], [76]. OCC allows for spatial filtering and tracking in the receiving device itself and longer frame periods provide integration that limits noise.

Focusing on the trade space of leveraging existing, low-cost hardware, we are confronted by the VLC challenge of avoiding flicker and glare that may distract drivers. Commodity cameras and light bulbs have been engineered to operate only within the limits of human perception. For example, camera frame rates are just fast enough for videos to appear smooth through human persistence of vision. This does not leave a significant amount of excess bandwidth to temporally embed information a person would not be able to perceive. To avoid heat waste, light bulbs are being engineered to produce as much visible light as possible while minimizing energy in other spectra. In optimizing bulbs and cameras, many opportunities to embed data outside human perception have been drastically reduced.

On top of this, daylight interference in VLC has been noted as a particularly hard problem to solve [28], [32]. Solar down well and atmospheric scattering during the day produce orders of magnitude more ambient light than observed indoors or at night. Of course, the constraints of system design, both for human safety and power utilization, preempt trying to outshine the sun.

The challenge of daylight impacting VLC is significant enough that in 2018, Islim et al. specifically wrote a paper “to address the perception that visible light communication

(VLC) systems cannot work under the presence of sunlight" [37]. Their 2018 paper, in turn, demonstrated a capability at 14 cm, theoretically extendable to 3 m. In 2022, Li et al. [70] achieved higher data rates at night "without the intense background solar noise" and found their VLC system to be SNR-limited at distances of 50 m or more.

2.3 System Model

In this section, we present a broad schematic framework and overview of transmitter and receiver technology which allows a systematic assessment of the constraints and opportunities for optimization. Focusing on the data link and physical layers, information sources and network routing above the VLC link are abstracted away. At the lowest layer, a transmitter sends data through a channel to a receiver. The channel constraints in both directions are illustrated in Figure 2.2. The channel introduces loss and noise, degrading the signal arriving at the receiver. Accounting for observers and other users of the channel, such as vehicle operators, there are also constraints on detectability. As a baseline, it is generally required that operating in the visible spectrum should not adversely impact human perception. Tighter constraints on detectability may even suggest steganographic "optical stealth communications" [77].

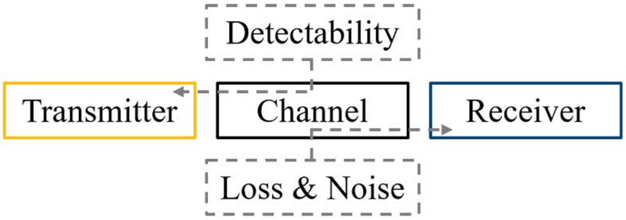

Figure 2.2. VLC system overview.

The five blocks in Figure 2.2 bound the space of exploration, looking to transmit data quickly and reliably while minimizing interference, detectability, and the costs of transmit and receive hardware.

2.3.1 Transmitters

Cars have used electric lights in various forms since the beginning of the twentieth century. Beginning in the 1940s, the use of dual-filament tungsten bulbs became ubiquitous, with halogen and later high-intensity discharge lights being introduced on high-end vehicles in the 1960s and 1990s respectively. Since the early 2000s, LEDs have continued to rapidly advance and expand market share in vehicle lighting [78].

Incandescent bulbs generate light through the electrical heating of a tungsten filament. Halogen bulbs also send current through a tungsten filament, but the bulb is filled with an inert gas, halogen, which increases light output and bulb longevity. However, both traditional and halogen incandescent bulbs are very inefficient at converting electrical energy into visible light, with typically only about 10% of the electrical energy converted to visible light and the remaining 90% lost as heat [79]. Given the inefficiency of incandescent bulbs, countries around the world have begun to ban them in general use [80], [81].

Florescent bulbs operate on a different mechanism with significantly higher efficiency. Florescent bulbs do not use a filament. Instead, the supplied electricity excites gas of vaporized mercury which emits ultraviolet (UV) light; this in turn causes a phosphor coating in the bulb to fluoresce, producing visible light. This conversion of electric to UV and then visible light by fluorescence is nearly 85% efficient [79]. The drastically higher efficiency of fluorescent bulbs has made them standard in many corporate and institutional settings. Compact fluorescent bulbs also initially supplanted many incandescent bulbs, but environmental concerns around mercury and the rapid maturation of LEDs have begun to shift most applications — growingly including vehicular applications — to LED.

LED bulbs are even more efficient than fluorescent, approaching 90% efficiency [79] in smaller, lighter form factors without the risks associated with mercury. The first mass-market white LED worked somewhat like fluorescent bulbs and leveraged a phosphor coating to create broad-spectrum visible light. In a phosphor coated (PC) LED, a strong blue LED is filtered through a phosphor coating that absorbs some of the blue light and fluoresces broadly across the visible spectrum, providing a visibly white light [82].

Figure 2.3 shows the spectrum produced by the bulb technologies with sunlight as a reference for typical visible white light outside. PC LEDs show a spike from the blue LED and the rounded-out spectrum generated by the phosphor coating. The spectrum of incandescent bulbs trends toward red and waste heat in the infrared and longer wavelengths. Compact fluorescent bulbs produce a mix of spikes as a result of gas excitation and phosphor interactions.

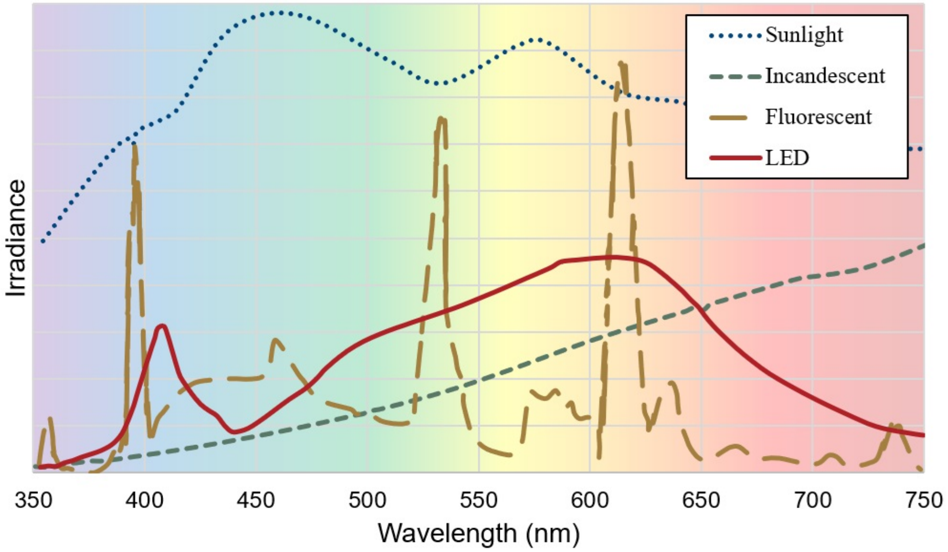

Figure 2.3. Spectra of various bulb technologies and sunlight. Adapted from [83].

Of note, each of these bulb technologies produces unique spectral shapes that are distinguishable from sunlight, presenting potential opportunities for filtering to aid in separating outdoor VLC signals from background sunlight.

Most bulbs aim to produce something that is visibly white as measured by a color rendering index (CRI), but "visibly white" is an artifact of the human visual system and not a consistent frequency distribution. Human vision is modeled with a tri-stimulus model aligning to peak sensitivity at green, followed by red and blue. A mixture of just red, green, and blue can appear to be any point in the color continuum of the visible spectrum, often illustrated via the International Commission on Illumination (Commission intertnationale de l'eclairage) (CIE) horseshoe diagram. All modern displays use a closely spaced grid of primary color pixels, mixing red, green, and blue to present all possible colors. Some new LED bulbs even use closely space red, blue, and green sources presenting an overall white appearance rather than the blue-with-filter approach used in PC LEDs.

2.3.2 Receivers

The goal of the receiver is to collect signal energy and where possible reject noise introduced by the channel. Ideally, if a receiver could counteract all the effects of the channel so that only a scaled, time-delayed version of original the signal was received, it would be possible to fully recover the transmitted signal. This section provides an overview of the basic technology used to capture signal energy, the commodity configuration we intend to utilize — CMOS — and filtering as it relates to color imaging and possible noise rejection.

Receivers for VLC fall into two broad categories, photodiodes and imaging sensor arrays. Sensor arrays themselves are simply arrays of multiple – often millions – of individual photodiodes. Single photodetectors are often employed in FSOC and other scenarios with controlled alignment since they are supported by relatively simple circuits and sample received photon counts very quickly. CMOS sensor arrays are widely used in cameras using a matrix of photodiodes enabling image generation with low-cost hardware. This section will provide a brief overview of the underlying principles of optical sensors and their implementation in cameras.

Fundamentally, an optical sensor is designed to convert light into an electrical signal. A basic optical sensor relies on an incoming photon having a high enough energy to excite an electron across the band gap of a semiconductor to build up a charge or enable current to flow, as shown in Figure 2.4. Once electrons have moved across the band gap, the change in charge or mobility is measured using amplification and processing by additional circuitry.

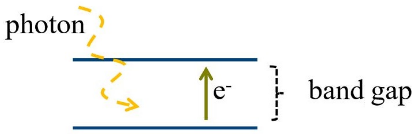

Figure 2.4. Photon exciting electron across band gap

Photodetectors generate electric current proportional to the square of the optical field striking the surface. The quantum efficiency of a detector is defined as

$$\eta_{qe} = \frac{\mathrm{e}^-_{out}}{\gamma_{in}} \tag{2.1}$$

where e^-_{out} are the number of electrons produced by the number of arriving photons, γ_{in}. Quantum efficiency can be derived in more detail based on the reflectivity of the photodetector surface and the portion of electron-hole pairs that contribute to current [84]. Due to inverse-squared losses, the wavefront reaching the photodetector is likely to be very weak and photodetectors are thus designed to be very sensitive. Response at varying wavelengths depends on the specific semiconductors employed, with silicon having a response curve across the visible light spectrum and gallium-arsenide semiconductors being biased toward peak response in the IR. For a photon to excite an electron across the band gap to generate an electron-hole pair, the incident photon's energy must exceed the energy gap. The energy gap for silicon is approximately 1.17 eV. The maximum wavelength, in μm, that a detector can receive is given by

$$\lambda_{cut} = \frac{hc}{E_{gap}} = \frac{1.24}{E_{gap}} \tag{2.2}$$

with E_{gap} given in eV, and h and c being Plank's constant and the speed of light respectively [84]. For silicon, this provides a maximum wavelength of approximately 1060 nm, well into the IR and sufficient to cover the visible light spectrum.

Camera Sensors

Typical camera sensors use a matrix of photodiodes to capture light at individual pixels which will comprise the image. The circuitry supporting the readout from this array classifies the sensor as either a charge coupled device (CCD) or a CMOS sensor.

In a CCD, the charge from the photodetectors is accumulated and transferred column by column before being converted to a voltage and read off the chip. CCD tend to offer high uniformity and efficiency but are more difficult to integrate with other circuits, draw more power, and have limited frame rates for large sensors [59].

In contrast, while a CMOS sensor also employs an array of photodetectors, the charge-to-voltage conversion occurs at each individual pixel site and values are read off by row and column, similar to reading out digital memory. This can allow for increased frame rates if only a subsection of the CMOS matrix is sampled. This configuration also allows for CMOS sensors to be integrated more directly with other circuit components, including the digital clock and analog-to-digital converters, reducing overall cost and leading to their widespread adoption in most commodity commercial applications, from cameras to phones [59].

The ubiquity of CMOS makes it a viable choice for VVLC. Beyond economic consideration, using a matrix of photodiodes in a CMOS sensor provides an opportunity for imaging and spatial filtering that an individual photodiode would not allow. Imaging provides an immediate boost in SNR since the background can be ignored while focusing on pixels that contain signal. It also allows wider FOV, permitting a vehicle to receive communication from any other vehicle or infrastructure in frame without the need for tracking and alignment needed to support FSOC.

While using cameras for sensors is both cost-effective and allows for spatial filtering, the limited sampling rate of image sensors remains a challenge. As with all communication and signal processing, the Nyquist rate requires sampling at least twice the rate of the maximum frequency of the signal to eliminate ambiguity in the signal spectrum, providing a significant limitation on throughput for VLC. Using commodity sensors, frame rates are limited to 240 Hz, and often only 30 or 60 frames per second (FPS).

It is possible to only read out some of the lines of a CMOS matrix to increase speed. This technique is employed in high-speed cameras, but not always broadly supported in commodity cameras used in typical OCC. Other techniques that have been used to speed up OCC include leveraging the line-by-line scan of the rolling shutter sensor readout — which can have a multiplicative effect on throughput — if multiple lines of the sensors are illuminated by the signal [85]. Spatially multiplexing transmitters can also increase throughput; separating distinct areas from within the pixel matrix of a CMOS sensor allows for simultaneous data streams.

Of the high-level system components, in Figure 2.2 we have the most control over the receiver. Understanding the transmitter and channel is informs our knowledge of the signal arriving at the receiver. In our efforts to increase SNR, we focus on filtering and processing at the receiver as a means to recover transmitted messages against bright backgrounds at long distances.

2.4 Received Signal-to-Noise Ratio

An overarching goal to enable VVLC is improving range, robustness, and data rates. The critical metric quantifying the capability of a system to convey data is SNR. This section provides an intuitive overview of SNR and explains why we focus on it as a metric rather than throughput or bit error rate (BER). More detailed computation of SNR continues in Section 4.5.

Foremost, SNR is simply defined as

$$\text{SNR} = \frac{\text{signal power}}{\text{noise power}} \tag{2.3}$$

and most often presented in a decibel form

$$\text{SNR}_{dB} = 10 \log_{10} \text{SNR} \tag{2.4}$$

which allows both straightforward additive calculations and compact notation for values covering a very wide dynamic range.

For any modulation technique, there is a minimum SNR required to decode symbols with the needed reliability. This can be visualized in many ways. For narrow-band RF communications, one can envision a bumpy background noise in the frequency domain. To receive data, the carrier frequency of the signal must spike higher than the bumps in the noise. Then, a filter can be applied to ignore all energy below the noise floor and process only spikes of energy containing the signal. The larger the spike of signal energy is compared to the random perturbations of the noise, the easier it is to properly decode the signal. SNR provides a means to quantify the difference in height between the signal and noise as the quotient of signal power divided by noise power.

Another way of visualizing SNR is the width of the traces in an eye diagram. Noise riding on the signal traces squeezes the gap between the symbols. As the amount of noise becomes commensurate with signal separation, the eye collapses and symbol errors occur.

From both these visualizations, we can intuit SNR as a buffer or allowable margin of error. If there is a large excess of gap space, significantly more signal than noise, it is possible to use multiple signaling levels and transmit more data. Rather than just detecting a high or a low in the eye diagram — or at frequency spike at one amplitude or location — a system could be built that used a high, a low, and a middle value. Including another possible output increases how much information the system can send at any instance, but also halves the buffer space between each level increasing the risk of an error due to noise.

The Shannon-Hartley theorem establishes that the maximum theoretical capacity of a channel to carry information — in additive white Gaussian noise (AWGN) — is

$$C = W \log_2(1 + \mathrm{SNR}) \tag{2.5}$$

where C is the channel capacity in bits per second and W is the bandwidth of the channel in Hz [86]. The higher the SNR, the more information a system can send.

Focusing on received power alone tends to drive solutions toward higher transmitter power. While higher transmit power compensates for channel losses due to spreading and absorption, it is contrary to the core VLC tenets of using existing fixtures without impacting the primary purpose of the fixture or harming people in the environment. Rather than increasing transmitted signal power, we focus on noise mitigation as a primary technique to increase SNR and, in turn, enable greater communication distances and data rates.

Higher SNRs allow faster, more robust communication. Most modern wireless communication systems have predefined modulation schemes depending on the level of noise to provide the best bit rate that conditions allow. When SNR is high and signal dominates noise, multi-level quadrature amplitude modulation (QAM) is used. When SNR is low, the system backs off to binary communications. Having observed high noise from daylight, we will focus our initial experimentation on binary messages. Without loss of generality, SNR improvements found can extend communication ranges or enable faster multi-level signaling to increase data rates. We will continue to expand on the calculation of SNR in Section 4.5 when we present our method for measuring SNR, but first begin by empirically measuring and statistically approximating the channel noise in daylight.

CHAPTER 3:
Empirically Quantifying Noise

A key challenge for outdoor VLC is the sheer amount of solar noise present in the background. As an example, it is very easy to see stars at night but during the day it is almost impossible to see the stars through the blue sky of our atmosphere. There are, of course, shades to this challenge for both astronomical observation and VVLC. Light pollution can make it harder to see stars at night and competing lights at night can interfere with VLC [87]. Likewise, with sufficient integration time and precise tracking, the light from stars can be found even through daytime skies. This chapter explores noise in the same way. To achieve sufficient SNR, transmit power or integration time can be increased to collect more signal power at the receiver. This presents obvious challenges for VLC needing to operate with existing fixtures and transmit data in reasonable periods of time. Subsequently, in Chapter 5, we will look at means to suppress noise to increase SNR by decreasing noise rather than increasing signal power. In this chapter, we begin by investigating the noise.

3.1 Components of Noise

To counter or mitigate noise, we must first establish a model. Often the easiest assumption is that of AWGN, which offers some mathematical simplicity. Shannon noted the entropy model of AWGN is representative of a worst-case scenario [35]. However, the actual noise in a VVLC using a camera as a receiver is an aggregate of noise sources from both the environment and the camera itself. It has been noted that a traditional Gaussian receiver performs suboptimally in non-Gaussian noise [88]. Daylight noise cannot have a perfect bell-shaped probability density function (PDF) because there are no negative photon values received[1] and the camera itself creates additive electrical and quantization noise. Nonetheless, from the experimental results presented in this chapter, we still find that AWGN is a good engineering approximation.

---

[1] We assume no negative photons, although negative frequencies can exist in optics [89].

3.1.1 Channel Noise

Expanding the channel block from Figure 2.2, Figure 3.1 enumerates more of the effects impacting the signal along the path to the receiver. While an ideal channel would simply produce a time-delayed copy of the transmitted signal scaled by an attenuation factor, atmospheric propagation is more complicated. Particle interactions scatter the signal while injecting light energy from other light sources into the channel. The superposition of signal and ambient light includes a smaller ratio of signal to ambient light the brighter the scene is. Turbulence causes dynamic shifts in focus, so the mixing ratios are not constant over time. The combination of these effects makes outdoor VLC particularly challenging.

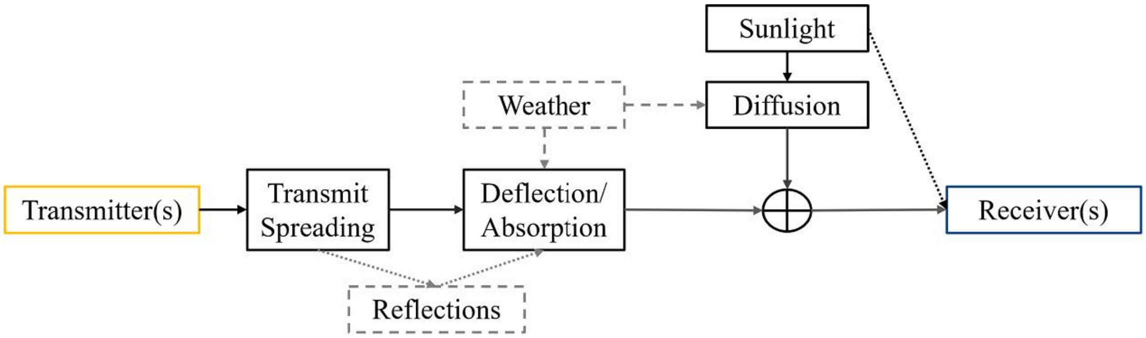

Figure 3.1. Effects in the channel reducing received signal power and introducing additional noise.

Signal Attenuation

Even before considering added noise, several factors degrade the received optical signal. Spreading attenuates signal power per the inverse-square law. Weather and other factors that cause absorption and scattering of light also reduce the amount of signal reaching the receiver. Finally, while optical frequencies tend to follow a predominate LOS path, they may have some Rician components where reflections can create multipath propagation. Multipath propagation leads to time-delayed versions of the signal smeared in time at the receiver.

As light energy propagates, it spreads in space, as illustrated in Figure 3.2. Considering a point source of light, at any distance from the source, the light energy is spread over the surface of a sphere with an area $4\pi r^2$. Many sources will have some directional gain, such as a parabolic reflector behind the light, but the gain from directionalized light is a constant multiple of the initial field. Holding the 4π and gain factors constant, the far-field loss can be approximated simply as $1/r^2$ [46].

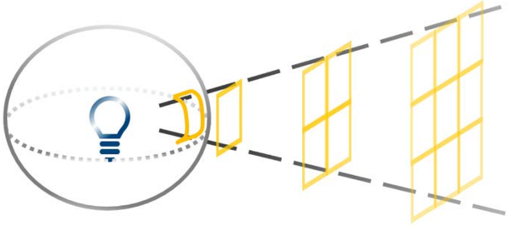

Figure 3.2. The inverse-squared law — optical power spreading. Source: [46].

Inverse-square law impacts on VLC are particularly pronounced due to the dimming constraint. An exemplar 10% dimming margin is shown in Figure 3.3. This fairly large margin not only challenges the constraint of avoiding operator distraction at short range but is also hard for the receiver to differentiate at greater distances. Without a dimming constraint, historic techniques — like shuttered signal lamps — can achieve communication at long ranges since the entire received power amplitude can be modulated and used to establish SNR at the receiver. With a dimming constraint on the modulation, the sliver of signal margin in Figure 3.3 must compete with noise, which becomes increasingly challenging as distances increase.

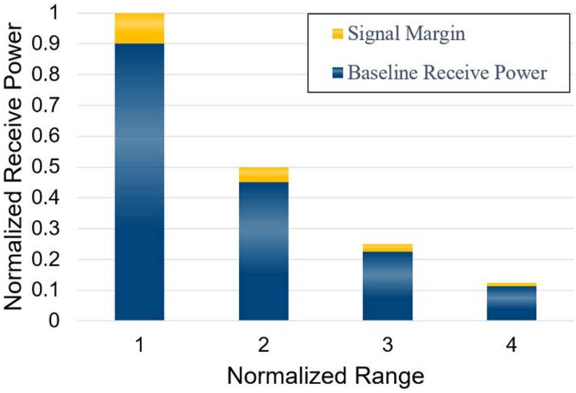

Figure 3.3. Fixed dimming margin offers lower detectable difference between signal and baseline as distance from the source increases.

Signal Scattering and Interference

Intuitively, weather and atmospheric particles can also significantly impact signal light before it reaches the sensor. Beyond spreading, some of the signal will be lost to atmospheric absorption and scattering. Often in weather forecasts, a visibility range is provided as a baseline for how far away a black object can be seen during the day.

A meteorological range is essentially equivalent, but defined by measurable quantities rather than subjective human observations. The horizontal meteorological range, H_{vis}, is defined as the distance where the intrinsic target to background contrast, $C_0 = 1$, is reduced to 2% at a central optical wavelength of 550 nm (a green near the center of human perception). Contrast is measured as the luminance of an object less the luminance of the background, relative to the background intensity

$$C_O = \frac{O - B}{B}. \tag{3.1}$$

where O and B are the luminance of an object and background respectively. Contrast attenuation is calculated as

$$C = C_0 \, e^{-\beta r} \tag{3.2}$$

where β is the extinction coefficient [90],on the order of 0.1 km^{-1} for clear air and around 2 km^{-1} for hazy or thin fog [91].

Scattering also introduces noise and increases with range. As the signal is scattered, not all the wavefront on the LOS path to the receiver reaches the receiver. Dust and fog, generally modeled as Mie scattering from spherical particles, deflect light and reduce received signal power. Scattering from other light sources also introduces additional noise energy into the path. Beer's law provides an approximation of transmittance — the ratio of power received, P_{Rx}, to power transmitted, P_{Tx} — through the atmosphere:

$$T_a(r) = \frac{P_{Rx}}{P_{Tx}} = e^{-a_e r} \tag{3.3}$$

where a_e is the extinction coefficient for power loss based on particle concentration and range [92]. Equations 3.2 and 3.3 have the same structure. They share equivalent constants, β and a_e, and range terms reflecting the reciprocity of the channel.

Lesser perturbations caused by pockets of air with varying temperature and humidity act as a series of prisms, causing beam spreading and loss. While this effect especially affects lasers in FSOC, it can still impact non-coherent light propagation in VLC. Numerous studies have aimed to quantify these perturbations, up to and including the use of machine learning [92], [93]. Generally, lasers can be focused to deliver tightly focused energy to about 2 km. In excess of 7 km, diffraction makes point delivery of energy infeasible [94]. However, minor variance in the laser wavefront does not prohibit communications. Rather, it drives the system designer to increase transmit power and primarily use intensity modulation, direct detection (IMDD) at the receiver (for both lasers and VLC). As light propagates both amplitude and phase fluctuate, making coherent detection challenging, so direct detection is employed in most free-space optical links [84].

Adaptive techniques to counter these perturbations attempt to flatten out deformation in the received wavefront with software or optics based on a known point in the image. Adaptive optics used in astronomical observations and FSOC employ mirrors that are deformed to counteract the deformation in the wavefront through the atmosphere. Adaptive filtering techniques attempt to reach a similar result without complex optics by convolving an approximation of the inverse of the channel with the received image. Application of a Wiener filter to correct for turbulence and aerosols has been employed to correct images, like those produced by a CMOS sensor, for atmospheric aberrations [95].

A detailed, controlled study of the impacts of taillight-based V2V VLC was conducted in [54] using a 5 m enclosed plexiglass chamber. Propagating an optical signal through thermal turbulence, simulated rain, and fog, each respectively increased attenuation and BER. Digital models of the impact of smoke and fog on outdoor VLC have also been developed showing minimal attenuation from light mist to ranges up to 1 km. Interestingly, scattering from atmospheric particles sometimes improves receive performance by spreading the signal over more of the receive sensor [73].

Another signal impairment occurs when the signal reaches the receiver via multiple paths. For example, a headlight could be visible both directly and through a reflection off the road surface. A simplified road reflection model — assuming a Lambertian order of one — leads to reflected radiant intensity, $\mathcal{R}$, of

$$\mathcal{R}(\phi) = \rho \frac{\cos \phi}{\pi} \tag{3.4}$$

where ϕ is the polar angle and ρ is the diffuse reflectivity [96].

Photodiodes typically have an area covering millions of square optical wavelengths. This provides inherent spatial diversity and, as such, Doppler effects are not generally pronounced in VLC [97]. Varying path length between a LOS and reflected signal reaching a photodetector may introduce some inter-symbol interference (ISI) from time lag, limiting the transmission speeds. However, at typical bit rates for VVLC, on the order of ten or less of Mbps, ISI is typically not an issue [96].

Atmospheric Turbulence

Turbulence in the channel is a significant consideration for FSOC using lasers. Denoted C_n^2, turbulence results from the motion of various pockets of air with different temperatures and humidities. Turbulence creates varying diffraction along the beam path leading to beam wander [98]. Given the alignment constraints of a FSOC, if energy wanders off the sensor the link fades or drops.

While there is a rich body of research that aims to quantify, model, and mitigate the impacts of turbulence [93], [98]–[102], Eso et al. found that in VVLC using incoherent light sources and cameras as receivers, link performance was not significantly impacted by amplitude fluctuations introduced by turbulence (with a C_n^2 of up to $1.1 \times 10^{-10}\ \text{m}^{-2/3}$) [103].

Additive Channel Noise

Piling on to the challenges of optical communication at range due to signal degradation, the atmosphere injects additional noise. Rayleigh scattering occurs when waves encounter particles much smaller than their wavelength, including the individual gas molecules of the atmosphere. The sky appears blue as nitrogen and oxygen molecules scatter more high-energy blue photons than longer-wavelength red photons. At sunset, as light passes through more atmosphere causing more scattering of blue light, red light becomes the dominant visible color, illuminating the sky in reds and oranges. Of course, this scattering occurs for all light, not just sunlight. All radiating and reflecting surfaces contribute to light being scattered in the direction of the sensor. Numerous techniques to counter this scattering have been developed for remote sensors, from detailed atmospheric physics models to simply calibrating images by setting the darkest areas to black [104].

The most powerful source of optical noise for daytime outdoor communication is sunlight scattered throughout the atmosphere. Sampling with a lux meter, the light energy arriving in the shade outdoors is still an order of magnitude higher than that of a brightly lit room indoors, and sensor readings in sunlight are yet another order of magnitude higher than outdoor shade. Before considering any other competing signals or moving objects in the V2V environment, the sun contributes substantial optical energy raising the noise floor for communication. Several physics and table-based models have been validated to approximate the atmospheric spectrum at varied locations, including MODTRAN [105], SMARTS2, and SPCTRAL2 [106]. SPCTRAL2 has been compared to measured values and validated for use in modeling channel noise for outdoor VLC [87], [107]. Of note, while any individual interaction of light with particles exhibits some directionality, multiple scatterings through the atmosphere tend to produce a net uniform distribution of scattering directions.

Compared to the daylight use case, the nighttime use case is significantly easier to tackle. However, the strong spectral components of artificial lights present different challenges than the sheer volume of noise from sunlight. Research has assessed the impact of artificial light sources which could impact outdoor V2X communication, including lighting, static advertisements (for example neon signs), and dynamic LED signs and billboards [87]. The spectral components of these different lights can vary significantly, and there is no standardized model, like SPCTRAL2, to account for man-made nighttime channel impacts. However, most lighting generally produces frequency components that match the power source at 60 Hz[2] and harmonics decay rapidly within several kHz. Lights employing electronic ballasts can have frequency components up to tens of kilohertz. Dynamic LED signs can have more complicated driving circuitry, potentially generating spectral interference at higher frequencies, even reaching hundreds of kHz, and potentially interfering with VLC signals [87]. Unlike natural light, it has been shown that the interference from artificial

---

[2] For North America and some of South America, or 50 Hz for most of Europe, Asia, and Africa.

sources is deterministic and filtering may help to reject this noise at the receiver [108]. Harkening back to the visibility of stars during the daytime and reduced visibility of stars at night where there is high light pollution, increased background noise from artificial light further raises the noise floor, obscuring yet more stars from view.

During the day, noise power from sunlight dominates outdoor VLC. Characterizing it to seek mitigation techniques is a focus of our research. While there are several empirically validated models of solar irradiance, most are focused on overall down well through the atmosphere and not scattering over horizontal paths near ground level. It has been observed that as solar radiation propagates down through the atmosphere, multiple repeated isotropic scatterings by atmospheric particles result in a diffused light field [91]. Given this repeated scattering, it may be reasonable to approximate the interfering sunlight as AWGN, accepting this is an imperfect approximation since we know the sky is blue and there is some angle-dependent polarization [109]. Table 3.1 shows approximate background sky luminance values in candela per square meter[3] [110], which vary significantly throughout the day but are always quite significant. For comparison, a study of peak low beam headlight intensities found values ranging from 2.2 $\times 10^4$ to 4.3 $\times 10^4$ cd [111].

Table 3.1. Approximate Background Sky Luminances. Adapted from [110].

Source	**Luminance, cd/m^2**
Sun, observed at zenith from Earth's surface	1.6×10^9
Sun, observed from Earth surface near horizon	6.0×10^6
Horizon sky, sunlit clouds	3.4×10^4
Horizon sky, clear day	3.4×10^3
Horizon sky, overcast	3.4×10^2
Clear night, moon lit	3.4×10^{-2}
Clear night, no moon	3.4×10^{-4}

Given that the power of background daylight is commensurate with the power of the transmitters, we hope to capitalize on the correlated nature of the transmitted signal to create gain across the receive array while the uncorrelated background is less amplified

---

[3] An overview of lights units is included in Appendix A.

by the signal correlation process. The atmosphere is assumed to be a homogeneous mix of air molecules [91], mostly nitrogen and oxygen. The respective molecule sizes are 155 and 152 pm (10^{-12} m), which is three orders of magnitude smaller than the wavelengths of interest and at least four orders of magnitude smaller than pixel sizes, so no specific array spacing to mitigate particle effects across the sensor is immediately apparent. Linear, arithmetic averaging across selected pixels is used.

3.1.2 Receiver Noise

While less than solar irradiance in outdoor VLC, receiver noise is still present in all optical communication systems. For low-cost OCC, quantization noise is particularly significant. Solar noise, while powerful, is relatively uniform. A DC offset is easily handled in signal processing. Removing the mean allows for modulation to be more easily detected. There will be limits to how much DC noise can be accommodated as it impacts the exposure and ability of a camera to quantize and discern differences between signal levels. As long as receiver saturation and quantization issues can be avoided, the result of the direct current (DC) bias is trivial, and variations, including internal noise introduced by the camera, may become a significant source of noise interfering with the signal.

Photoelectric imaging systems experience noise both from photon-to-electron conversion and the random thermal agitation in the circuits that acquire and process data from the sensor. Photoelectron noise can occur in two statistical cases. At very low light levels, photoelectrons emitted are governed by Bose-Einstein statistics (often approximated by a Poisson distribution). At higher light levels, the output can be modeled by a Gaussian distribution with a standard deviation equal to the square root of the mean [112]. Circuit thermal noise is generally considered white [113], [114]. Miller and Childers note that white assumption breaks down at optical frequencies, and direct application of a kTB noise figure based on the 300 THz optical bandwidth is invalid [114]. However, thermal noise calculations based on frequencies related to processing images in the camera are still relevant.

Internal Camera Noise and Quantization

While ideally the only noise in a photodetector would be from the packetized quantum nature of light itself, noise is also intrinsic in the receiver. Shot noise, from the quantized arrival of photons, occurs in a Poisson distribution. However, the overall brightness in VLC systems means large photon counts are received, making the Poisson distribution functionally Gaussian [115]. There is also always some current in the semiconductor, even in the absence of light, setting a floor for the minimum detectable signal. Noise equivalent power quantifies the minimum detection threshold of a photodetector. Also impacting the receive circuitry, background radiation and Johnson noise caused by the random movement of electrons contribute to overall noise received [84]. If the ambient light is negligible, the primary source of noise in the receiver pre-amplifier is thermal noise [97]. The camera processing circuitry itself will add some noise degrading SNR, often cumulatively captured as a noise figure where

$$\mathrm{SNR}_{out} = \frac{\mathrm{SNR}_{in}}{F} \tag{3.5}$$

and the noise figure, F, is a value greater than or equal to one.

However, in the outdoor use case, we expect the dominant noise source will remain channel noise from sunlight and internal camera noises will tend to be relatively small. Beyond the thermal noise and other factors that contribute to the noise figure before digitization, the process of quantizing the sensor data introduces its own artifacts. A signal-to-quantization-noise ratio (SQNR) measures the impacts of the additional quantization noise introduced by rounding all received values to a digital output bin. SQNR is defined analogously to SNR

$$\mathrm{SQNR} = \frac{P_{sig}}{P_Q} \tag{3.6}$$

where P_Q is the quantization noise power based on a uniform distribution of error.

Assuming the source signal is continuous and uniformly distributed across the quantization range, every quantized value will have an error uniformly distributed in a range $\pm 1/2$ the width of a quantization bin. The width of a quantization bin can be found as

$$\Delta = \frac{A}{N/2} \tag{3.7}$$

where A is the maximum amplitude of a unipolar signal and N is the number of quantization steps. In all practical digital systems, N will always be a power of two, so we can substitute $N = 2^b$ where b is the number of bits used. Recalling the variance of a uniform distribution is

$$\sigma_Q^2 = \frac{\Delta^2}{12} \tag{3.8}$$

we can substitute in to find the quantization noise variance [116]. Equivalently, quantization noise power (as will be expanded on in Section 4.5), is

$$\sigma_Q^2 = P_Q = \frac{A^2}{3 \times 2^{2b}} \ . \tag{3.9}$$

For a squared wave of amplitude A, power is A^2, so

$$\text{SQNR} = A^2 \times \frac{3 \times 2^{2b}}{A^2} = 3 \times 2^{2b} \tag{3.10}$$

or in decibels

$$\begin{aligned} \text{SQNR} &= 10 \log_{10} \left(3 \times 2^{2b}\right) \\ &= 10 \log_{10} 3 + 10 \times 2b \log_{10} 2 \\ &= 4.77 + 6.02b \end{aligned} \tag{3.11}$$

providing an approximation that each bit of quantizer resolution in a uniformly distributed quantizer allows for 6 dB of SQNR. Assuming a typical 8-bit quantizer, this limits maximum SNR to approximately 48 dB.

Since we are extracting signals not from raw sensor data, but rather videos stored to memory, digital storage noise — beyond quantization noise — will also be introduced. Recent flagship smartphones allow shooting still pictures in RAW format, where the actual pixel readings are directly stored before any demosaicing or compression. While RAW images can be stored, RAW videos cannot. There are neither sufficient compute nor memory resources to write such large files to storage. Assuming the dual-use of camera sensors in a VVLC implementation, it is likely signal extraction will need to rely on compressed videos. The compression process introduces some additional noise artifacts. In demosaicing, adjacent colors from the camera color filter array (CFA) are blended to produce a color value at each pixel. With sufficient pixel fill, this is a non-issue for a white light source. In fact, this smoothing may actually help level off noise in any individual pixel. However, as pixel fill decreases, demosaicing may errantly blend bits of background into the signal pixels. Beyond this inherent pixel mixing, the compression of video leverages blocks that are processed through a discrete cosine transform and then quantized (similar to JPEG compression), resulting in the potential for further spatial blurring.

Analysis with the IMX363 Sensor

Beyond frame rate limitations and setting aside clock synchronization for precise symbol period alignment, our digital receiver is limited in both detection sensitivity and resolution. To facilitate assessment, we will leverage the Sony IMX363 EXMOR RS as an exemplar sensor. It has broad market share and is used in the Pixel 3, Pixel 4, Pixel 5, and Pixel 6 lines. Our test devices are Pixel 6a camera phones. Validating computerized models of camera performance, Lyu et al. [117] laid out their researched parameters for the IMX363 sensor as shown in Table 3.2.

Table 3.2. Sony IMX363 Sensor Specifications. Source: [117]

Properties	**Parameters**	**Values (units)**
Geometric	Pixel Size	[1.4,1.4] (μm)
	Fill Factor	100(%)
Electronics	Well Capacity	6000 (e^-)
	Voltage Swing	0.4591 (volts)
	Conversion Gain	0.1707 (dv/e^-)
	Analog Gain	1
	Black Level Offset	64 (dv)
	Quantization Method	10 (bit)
Noise Sources @ Analog Gain =1	DSNU	0.038 (mV)
	PRNU	0.54 (%)
	Dark Voltage	0.02 (mV/sec)
	Read Noise	0.226 (mV)

The pattern noise values in Table 3.2, dark signal non-uniformity (DSNU) and photo response non-uniformity (PRNU), represent fixed noise patterns in the sensor that do not average out over time like shot noise. However, using an array gain approach to level noise across multiple pixels, these noise artifacts affecting columns and pixels in the scene will average down across more of the array.

With a 10-bit on-chip quantizer, 1024 possible digital read-out values are possible. With a maximum well capacity of 6000 electrons, approximately every 6 electrons converted can facilitate movement to the next quantization step. Black level offset slightly compresses dynamic range, but allows for other noises in the camera. Using 64 digital values as black offset accounts for 6% of the quantization bins, while read noise is only 0.5% of the total voltage swing of the output. Sensor noise itself is remarkably low.

However, while the IMX363 has a 10-bit quantizer, our processing and analysis are generally limited to 8 bits — 256 values — of dynamic range. The maximum luminance value of a 256-bit range is 65536, or in decibels $10 \log_{10}(65536) = 48.16$ dB, in near perfect alignment with the approximation derived in Equation 3.11. The 6 dB step size will mask most least-significant-bit noise in the sensor, but in boundary cases result in large jumps between quantization levels. Though an additive component of overall noise, intrinsic camera shot and thermal noise are relatively small in the overall system, they can introduce jitter which will be amplified in quantization. Ultimately, while sunlight and ambient background contribute the most extraneous power to the system, all the smaller noise effects play a subtle role as they can agitate even steady scene areas between quantization levels:

$$\mathbb{E}\left[P_N\right] = \mathbb{E}\left[P_{sun} + P_{amb} + P_{atm} + P_{cam} + P_Q + P_{comp}\right] \tag{3.12}$$

with $\mathbb{E}$ denoting the expectation operator, where the total expected noise, P_N, is the sum of the expected power from solar noise, P_{sun}, ambient background lights and scene movement, P_{amb}, atmospheric turbulence and scintillation, P_{atm}, internal camera noise, P_{cam}, quantization noise, P_Q, and other processing and compression noise, P_{comp}.

In a darkened environment — such as at night — the ambient light power approaches zero and we can neglect some noise terms. More importantly, lower background brightness helps constrain the maximum amplitude the quantizer must account for, making each quantization step, Δ, smaller and increasing the sensitivity to smaller changes in the received signal. In this case, our simplifying assumption that camera noise is negligible may no longer hold, and camera noise will actually limit how dim a signal we can amplify and extract meaningful data from. The effects of sensor noise were clearly apparent in previous-generation smartphone cameras where dimly lit scenes introduced significant graininess and speckling in pictures. In the outdoor VLC case, sunlight dominates and masks internal sensor noise. We cannot simply amplify a minuscule received signal power, since doing so would cause the power from the sunlight to drive the receiver into saturation.

3.2 Baseline Noise Measurements

Given the theoretical baseline for noise sources established in Section 3.1 we proceed to empirically quantify noise in the channel and receiver through measurements conducted over a full solar day. Using the same receiver hardware that we use to assess noise mitigation techniques in Chapter 5, we recorded a static target with no embedded signal — only noise —

to establish a baseline. Recordings were taken hourly over a single day, from 0700 until 2100. Throughout the day, the location of the black and white target and camera remained constant while sun angle and intensity varied from early morning through solar noon into civil twilight.

3.2.1 Varying Noise Throughout the Day

Recordings of a static scene, without a modulated transmitter, were used to establish a baseline for noise. Working toward the realization of a commodity camera-based OCC system, the Pixel 6a with the Sony IMX363 EXMOR sensor was the primary sensor for these baseline collections.

Initially, a large projector screen was used as a baseline flat white surface. When exposed to wind outdoors, minor luffing in the surface contributed to the noise signal received and experimentation was moved to a more rigid noise target. The noise target consisted of a piece of plexiglass painted with 11×11 cm square areas of white, black, and white along with gray shaded borders backed by solid white paint, as seen in Figure 3.4(a). The surface of the plexiglass retained a shine similar to what we would expect from a vehicle light housing. This shininess allowed it to reflect ambient light and glare as would be seen in a vehicular use case. The target board was mounted nearly vertically to the ground and perpendicular to the direction of the camera.

The receiver was a Pixel 6a smartphone, running the stock Android 13 camera application. The camera phone was mounted in a custom 3D printed holder, allowing it to be affixed to a tripod as well as hold various colored lenses. The tripod was placed 25 m from the target with no obstructions in the line of sight, as shown in Figure 3.4(b). The Pixel 6a was set to record video at 2× optical zoom and a 1/8× speed slow motion, equivalent to 240 frames per second. Atmospheric conditions — including sun angle, temperature, humidity, cloud cover, and visibility — were recorded and can be found in Table 3.3. A Sekonic LiteMaster Pro luminance meter captured the average brightness from the tripod in the direction of the target at each time of day.

Table 3.3. Recorded brightness, sun angle, and atmospheric conditions during noise baseline testing on 14 July 2023. Line of bearing from the camera to the noise target was 107.8° (true).

Time (Local)	**Ambient Brightness (lx)**	**Sun Alt (°)**	**Sun Dir (°)**	**Temp (C)**	**Humidity (%)**	**Wind (km/h)**	**Wind Dir**	**Vis. (km)**	**Cloud Cover (%)**	**Ceiling (m)**	**Description**
0700	2200	10	70	12	92	3	NNW	3	100	853	Morning fog
0800	6800	22	78	12	94	3	NNW	0	100	488	Morning fog/minimal mist
0900	17000	34	87	13	94	3	NW	2	20	8016	Reducing fog
1000	24000	46	96	13	92	3	NW	14	76	1158	Clearing
1100	30000	57	108	14	94	5	WNW	5	76	11887	Clearing, breezy
1200	44000	68	128	14	88	8	WNW	14	89	2774	Overcast, sun penetrating
1300	27000	75	170	15	90	8	WNW	16	79	2377	Mostly clear, overcast sky
1400	24000	72	218	15	88	8	WNW	14	48	6096	Mostly clear, overcast sky
1500	20000	62	245	15	88	8	WNW	16	47	12192	Mostly clear, overcast sky
1600	18000	51	259	15	88	10	WNW	16	24	12192	Mostly clear, overcast sky
1700	13000	39	269	14	89	8	WNW	16	76	5243	Mostly clear, overcast sky
1800	6800	27	278	14	89	8	WNW	14	92	9296	Haze returning
1900	2700	15	286	14	89	6	WNW	14	80	9266	Returning fog
2000	500	4	294	13	92	6	W	13	87	9266	Increasing fog
2100	0	-7	303	13	92	–	–	11	89	1372	Fog/misty

(a) (b)

Figure 3.4. Noise baseline collection set up with a black and white target board (a) shown up close and (b) viewed through and past the Pixel 6a collecting at 25 m.

Average values of black and white pixels at each time of day are recorded in Figure 3.5. White areas on the target have a typical value on the quantizer of around 225 out of 250. Conversely, black pixels have an average value of around 70 out of 250. As expected, black pixels are significantly darker. However, they are not as close to the lower quantization rail as the white pixels are to the top.

Camera processing is non-linear. Exposure compensation attempts to logarithmically spread out quantization bins around a middle gray level in the image. This produces a gamma curve — similar to μ-law companding in telephony — where input values are mapped to logarithmically-spaced output values. In turn, looking at noise power — that is, how much pixels values moved up and down despite no actual change in the scene — black pixels have more noise than white pixels, as shown in Figure 3.6. This asymmetry of the binary channel is important for optimizing error probability and will be revisited later in Chapter 4.

While the values of black and white areas in the scene are fairly consistent, the number of photons arriving at the camera is not. As seen in Table 3.3, the brightness varies greatly across the day, getting brighter until midday and then falling off again. The illuminance from a white or black areas are likewise varying, but in forming the picture their proportional intensity remains constant. This is only a static scene. Later, when we analyze signals embedded in these scenes, the change in scene brightness becomes impactful. VLC in bright daylight is challenging. A bright background can suppress the signal from a transmitter with fixed intensity, like a vehicle headlight.

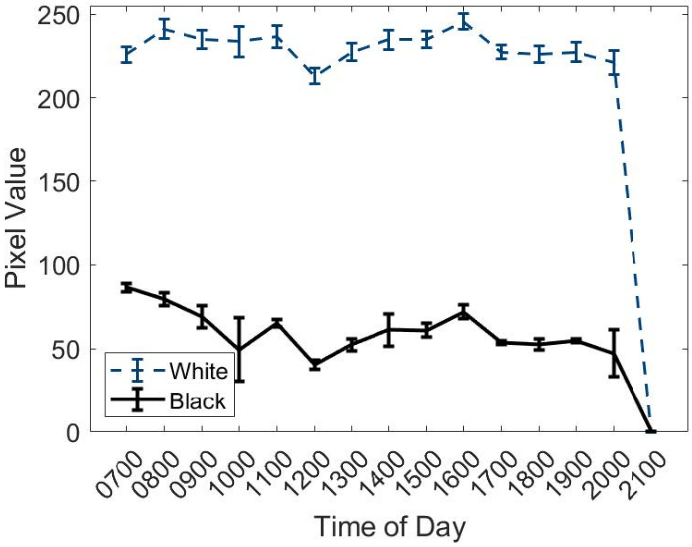

Figure 3.5. Mean value of static white and black pixels (over a minimum of 14 400 pixel values per point) measured hourly throughout the day. White areas on the target measure toward the top of the quantizer bins, while black areas on the target are farther from the quantization floor.

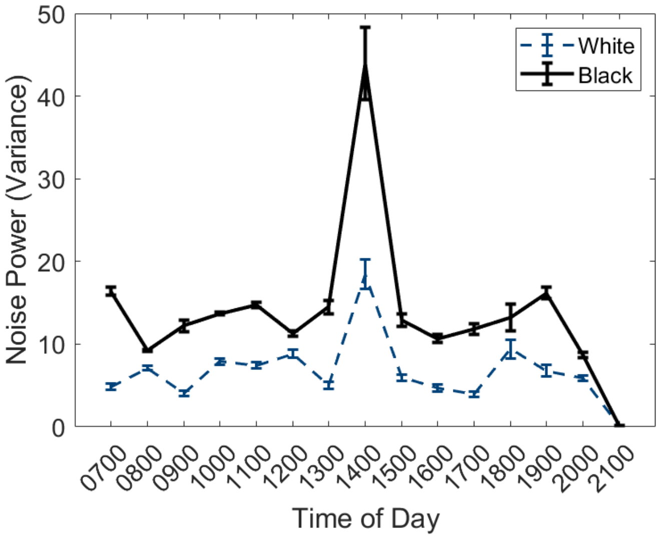

Figure 3.6. Noise power measured hourly throughout the day from the same sample points used in Figure 3.5. Readings from black pixels on the target board are often two times noisier than readings from white pixels.

Beyond directly recording with the Pixel 6a, baseline measurements with red, green, and blue colored filters were collected from the same positions at the same intervals. The mean values for filtered white pixels across the day are captured in Figure 3.7, while the noise power of the filter white pixels is shown in Figure 3.8. Across the board, the average white pixel values track very closely with the recordings without any filters. We do not see any effect where using a red or blue filter — utilizing only a quarter of the Bayer CFA — drastically drops the quantized illuminance value. Rather, the cumulative effect of quantization and encoding compression is that overall luminance of the white areas on the static target stays nearly the same regardless of spectral filter. With filters attenuating the received image, the quantizer adjusts to the dynamic range. This automatic scaling is similar to the effect we saw with varying brightness at different times of day. However, under-utilizing the pixels in the CFA, we do see an increase in noise. There are twice as many green pixels as red or blue pixels, and the scene viewed through a green optical window has noise that hues close to the unfiltered case. As more sub-pixels are included demosaicing and compression provide some smoothing, reducing noise across the adjacent pixels in the CFA.

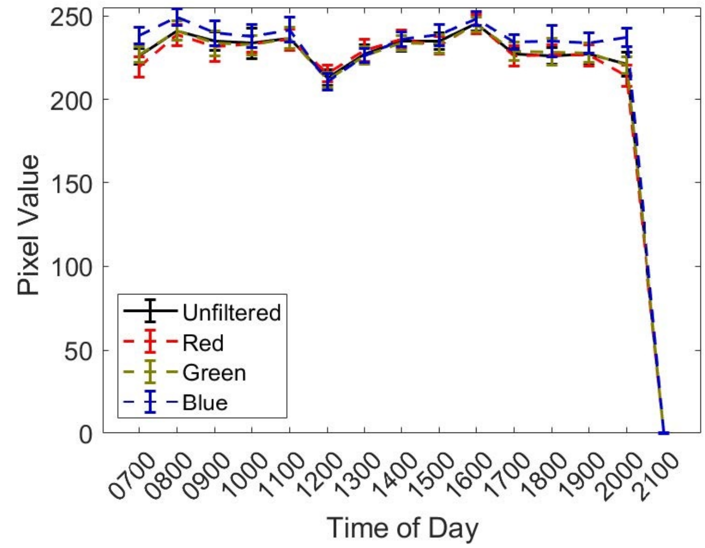

Figure 3.7. Mean value of static white pixels measured hourly throughout the day with various colored filters, using 19 200 samples per point.

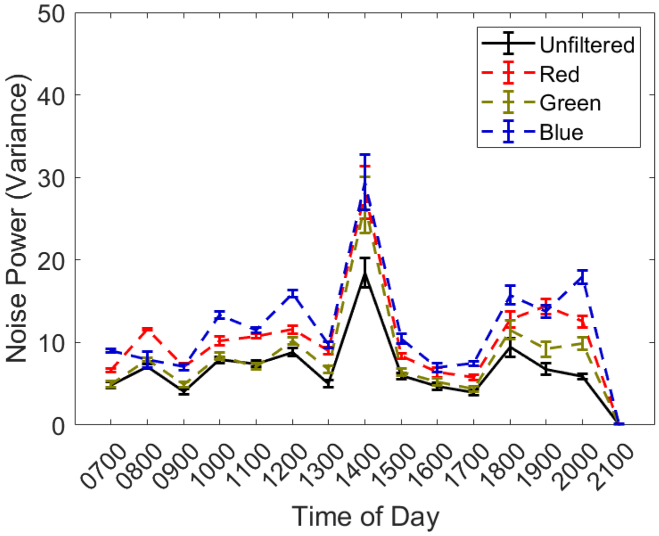

Figure 3.8. Noise power measured hourly throughout the day based on readings from white pixels recorded through various colored filters with the sample count as Figure 3.7.

3.2.2 Impact of Frame Rate on Noise

Noting the relatively consistent shape of mean values and noise throughout the day, we also considered the impact of frame rate on noise. Using a Chronos high-speed camera — rather than the Pixel 6a — we explored faster frame rates. While the Pixel 6a is limited to 240 frames per second, the Chronos camera is capable of thousands of frames per second [118]. Generally, in photography, longer exposure times lead to clearer pictures, and very fast shutter speeds with high light sensitivity values lead to more graininess of the images. With low-photon intensity images, stacking multiple short-duration frames increases the overall SNR of the image by the square root of the number of frames averaged [119]. For data throughput, shorter symbol durations are desired, but our focus remains on applying low-cost commodity sensors more similar to the smartphone, so we are bounded by an upper FPS limit. Nonetheless, it is worth considering the impact of integration time on noise in a VVLC system.

Using the Chronos high-speed camera, the same fixed target was recorded at frame rates of 15 FPS to nearly 2000 FPS with the results shown in Figure 3.9. The results tend along the square root improvement approximation from [119], with the overarching result that longer integration times reduce noise. However, we also see that the increase in variation is relatively low compared to the increase in frame rate and is generally constrained within one quantization bin. If it were necessary to get communications through in a very noisy environment, it would be possible to improve SNR by transmitting bits extremely slowly, much like finding stars during the daytime through persistent integration with precise pointing. However, shorter frame times will increase channel capacity by allowing more bits, including error-correcting bits, to pass through the channel.

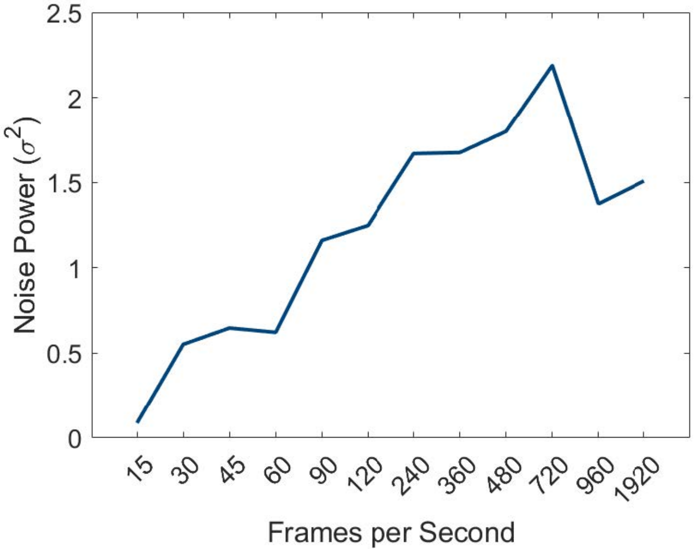

Figure 3.9. Average noise power over a ten-second recording versus frame rate using Chronos high-speed camera. Longer integration times tend to reduce noise.

3.3 Statistical Model

Capturing noise power as the variance of the baseline signal, we found a normal distribution to be a reasonable model of the noise. Using 24 400 white data points collected at one o'clock local, near the solar noon, a PDF for noise was developed. Applying numerous possible PDF fits in MATLAB, as shown in Figure 3.10, we see that a normal distribution is a reasonable approximation of the noise signal observed. Similar distributions such as the Rician and Gamma fits perform no better than a straightforward normal distribution. The skew of Poison and Weibull distributions is unwarranted given the symmetric bell shape of the data.

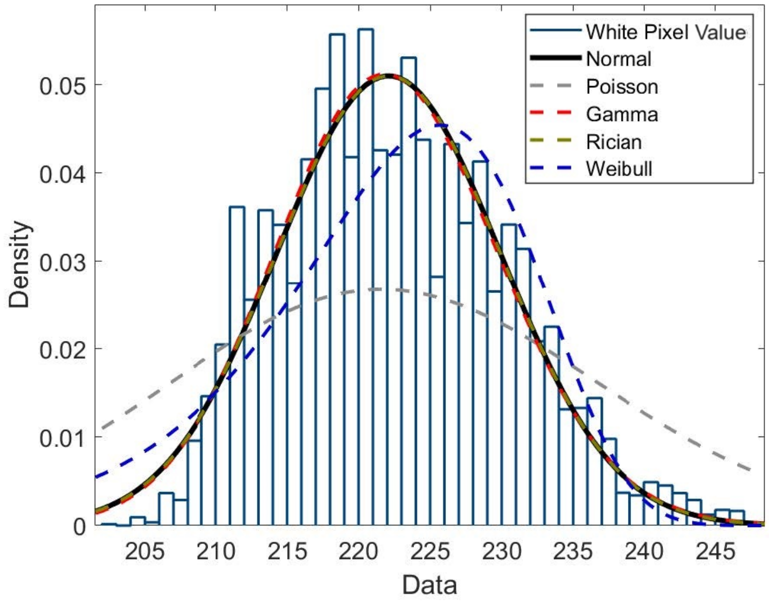

Figure 3.10. PDF fits for noise collected from 24 400 white sample points at one o'clock in the afternoon. A normal Gaussian distribution provides a reasonable approximation.

As noted earlier, the raw data itself cannot be purely Gaussian because there are no negative values and quantization bins are finite. The normal distribution has a PDF of

$$f(x) = \frac{1}{\sigma_0\sqrt{2\pi}} e^{-\frac{1}{2}\left(\frac{x-\mu_0}{\sigma_0}\right)^2} \tag{3.13}$$

where μ is the mean and σ is the variance. While PDF for a normal distribution is defined from $-\infty$ to ∞, the quantizer can only output values between 0 and 255. The normal distribution fit in Figure 3.10 has a mean of 222 and a variance of 61. Integrating the PDF of the normal distribution, in Equation 3.13, from $-\infty$ to ∞ the total probability is one. However, integrating Equation 3.13 from 0 to 255 with $\mu = 222$ and $\sigma = \sqrt{61}$ is approximately 0.99999. Since the mean value of white pixels is nearer the upper quantization bound, it is more likely to be clipped. At the upper bound, α_{255}, 10^{-5} is truncated from a true Gaussian distribution. The truncation below zero, α_0, only removes about 5×10^{-178} from the lower tail of a pure Gaussian distribution. This truncated Gaussian distribution is shown in Figure 3.11. To create a valid PDF, with a total probability of one, all probability values between 0 and 255 would need to be scaled by a factor of $1/(\alpha_0 + \alpha_{255})$ — approximately 1.00001. Similarly, for a black pixel with $\mu = 70$ and $\sigma = \sqrt{122}$, the truncated sides are reversed, but the truncation is also reduced since the mean is more centered between 0 and 255. The total probability contained in the black pixel normal PDF between 0 and 255 is approximately 0.9999999999. In both cases, the tails of the Gaussian approximation decay rapidly enough that a normal model is a good fit for engineering analysis with the scaling constant approximately unity.

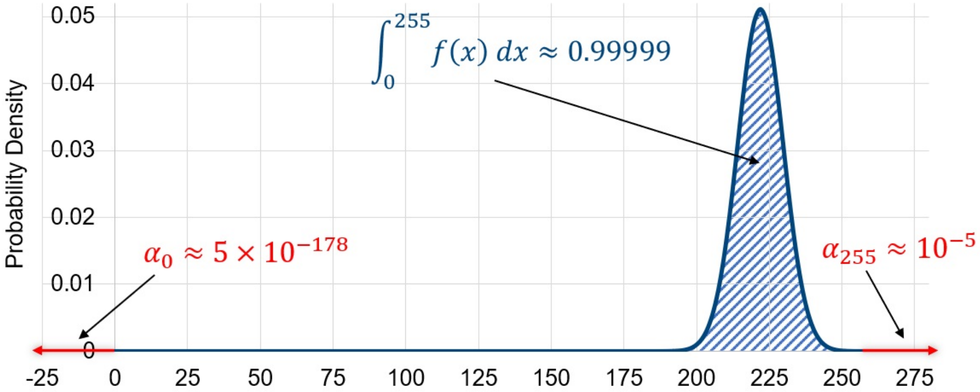

Figure 3.11. A Gaussian distribution with $\mu = 222$ and $\sigma = \sqrt{61}$, matching the normal distribution fit in Figure 3.10. Since the quantizer can only produce values between 0 and 255, the areas marked in red (α_0 and α_{255}) are truncated. To normalize the truncated Gaussian producing a statistically valid PDF, a scaling constant of $1/(\alpha_0 + \alpha_{255}) \approx 1.00001$ is needed.

Further assessing the AWGN approximation, an autocorrelation of the noise in time was assessed. Through all our data collection, we consistently find a very low-frequency component of noise that must be removed to help us establish a clean DC offset level. This frequency is typically in the range of less than two hertz and does not interfere with data transmission. Having removed any of these extremely low-frequency fluctuations, the remaining frequencies show no correlation as time progresses. That is, noise in one instant is not dependent on noise in any other future or past instant. This property means the noise is effectively white. The result of the autocorrelation of the noise with itself in time is shown in Figure 3.12, with output similar to the delta we would expect from white noise.

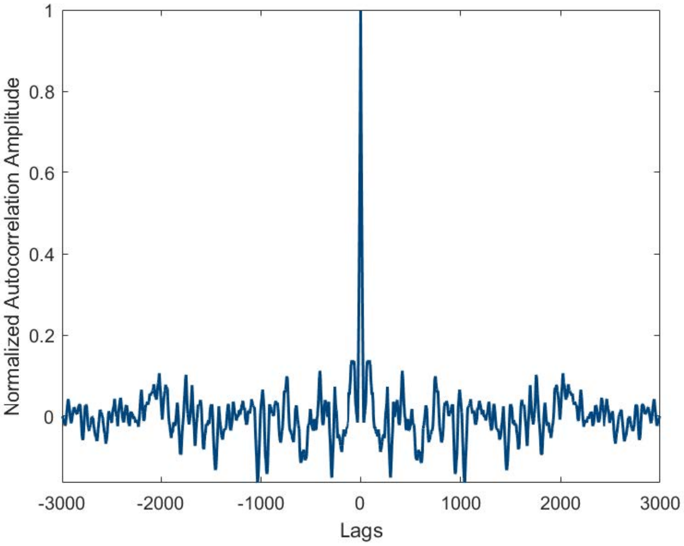

Figure 3.12. Autocorrelation of noise. The large spike at zero lag indicates that the noise is mostly white.

THIS PAGE INTENTIONALLY LEFT BLANK

CHAPTER 4: Method for Signal Generation and Detection

This chapter outlines our method for generating and testing a visible light signal in daylight conditions at increasing distances. The broad employment of LED fixtures has catalyzed recent research on VLC but does not completely define the space. As introduced in Section 2.3.1, there are various light sources that could be modulated to encode data, but LEDs offer a significant speed advantage over legacy light sources. While other technologies could be employed, after accounting for their slower transition times, our experiments leverage an LED headlight. LED headlights are the market trend for late-model vehicles and allow for the greatest precision in controlling the timing of light pulses.

The vast majority of VLC research, 88%, leverages photodiodes for receivers [30], but we use a camera. While photodiodes can be sampled faster to increase bit rate, we believe that the trade-off in spatial resolution and the ability to reuse existing camera hardware in vehicles is beneficial. Reusing existing forward-looking lane assist and rear-facing backup camera allows fielding of a VVLC system at low cost with no additional hardware, as illustrated by Plattner and Ostermayer's software only demonstration [4].

Our focus, both for transmission and receiving data, is on low-cost, commodity hardware. While there are clearly opportunities for other systems leveraging greater power, selectivity, or sensitivity, wide adoption will demand the utilization of low-cost and existing fixtures. Reducing the barrier to entry is critical for any ITS. Meaningful saturation in the market must be achieved in order to extract any systemic benefit or value. For a VVLC system to work, most all vehicles need to be able to communicate with each other in a standardized way.

4.1 Transmitter for Experiment

As stated, we used an LED car headlight in our experimentation. Many late-model cars include LEDs as part of the stock fixtures. LED bulbs are also available as retrofits for older existing incandescent and halogen headlight housings. We used such a replacement bulb in the headlight housing for a Ford Taurus as our test transmitter. The headlight housing had two primary reflector areas; we leveraged the smaller, outer reflector for our testing. The smaller size is in line with a typical daytime running light. Using the primary headlight fixture would have also worked, but daytime running lights are more likely to be on and available for VVLC during the day. Details of the bulb retrofit to allow modulation while mounted in the housing are provided in Appendix B.

With the LED in the housing, modulation was controlled via an Arduino Uno microcontroller. The Arduino was found to produce more precise control of pulse timing than other methods explored, as discussed in Appendix C. General purpose input/output (GPIO) output pin 13 was modulated with the data via a simple on-off keying scheme. This 5 V GPIO output was used as a control input to a femtobuck toggling on/off a constant current of 660 mA to the LED bulb.

The transmitted sequence consisted of a preamble of 32 high and low pulses (for a total of 64 symbol slots) and then 128 bits of data after a brief pause. For most of our experimentation, the symbol period was set to 30 ms. LED switching speeds can easily exceed 500 MHz [120], but the clock on the Arduino is limited to 16 MHz. For intensity-based OCC, transmit speed is driven by the frame rate of the camera. The transmitted signal can be seen in Figure 4.1.

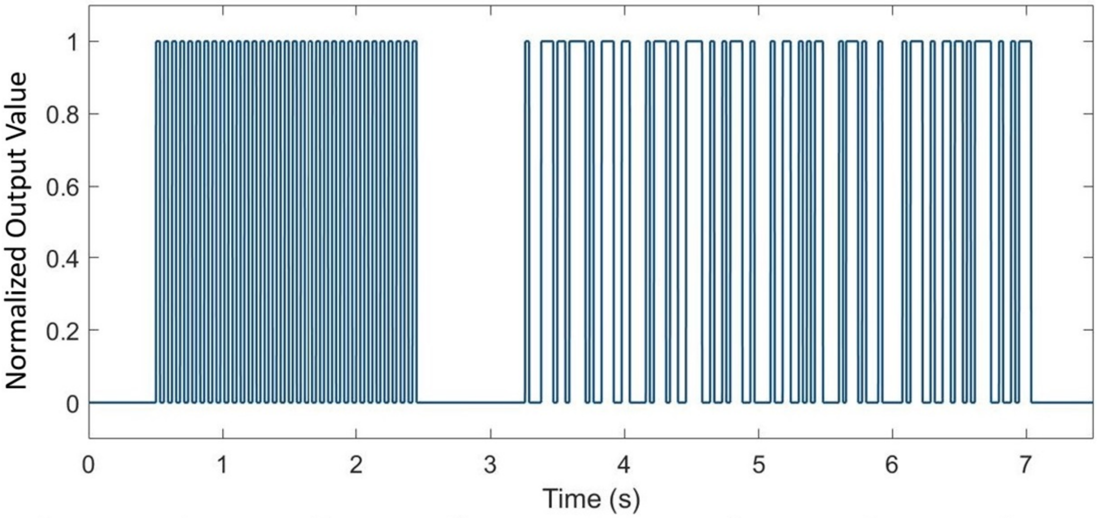

Figure 4.1. The transmitted signal, including preamble, gap, and data bits consisting of 16 bytes of ASCII encoded characters.

The overall transmit assembly configured for outdoor experimentation consisted of the LED bulb mounted in the headlight fixture on a metal cart. A portable lithium-ion battery was used to provide 12 V to the femtobuck headlight drive circuit as well as 5 V to the Arduino microcontroller via a built-in USB A port. A small fan was also powered, to ensure neither of the aforementioned components overheated in direct sun exposure. No thermal issues were encountered throughout testing — and the fan could have been omitted — but the precaution ensured we were able to conduct multiple days of testing without the potential for thermal complications. Figure 4.2 shows the wiring on the test cart as well as the transmitter as viewed from the direction of collection.

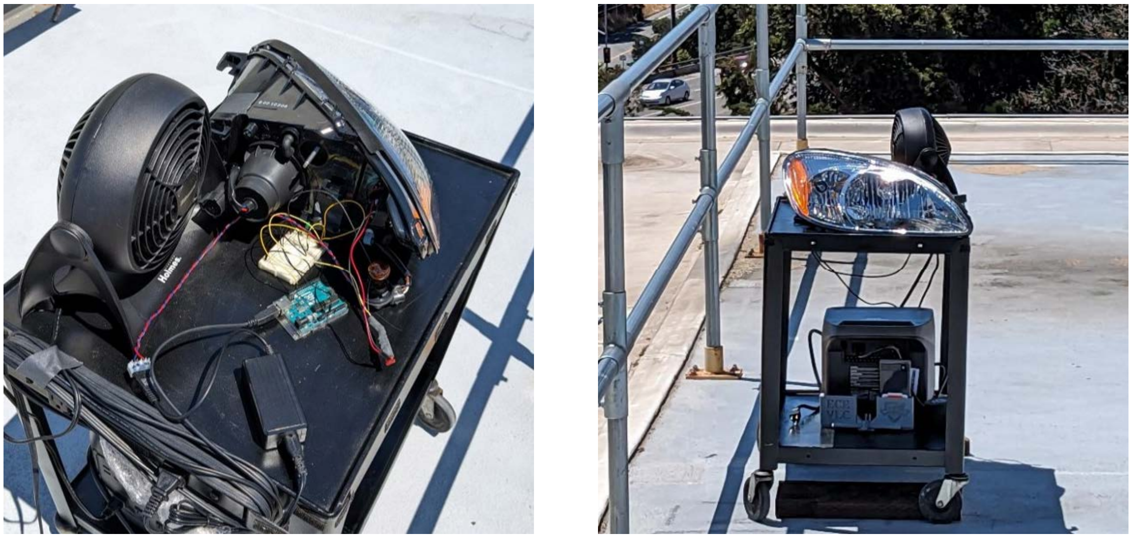

(a) (b)

Figure 4.2. The transmitting headlight set up viewed from (a) above and (b) the direction of collection.

4.2 Receiver for Experiment

Consistent with our focus on low-cost hardware, our receiving camera was a Pixel 6a smartphone leveraging the IMX363 sensor as outlined in Section 3.1.2. In order to focus on noise mitigation techniques rather than deal extensively with other complications of VVLC — such as target movement tracking — custom 3D printed mounts were made to fix the camera phones to a tripod, as seen in Figure 4.3. Focusing on noise mitigation, channel noise and atmospheric turbulence were of greater interest than tracking. In vehicular implementation, tracking and stabilization (including the use of optical flow methods to correct for movement) will be important. For baseline noise mitigation, additional tracking and stabilization add excessive complexity. As will be seen in Chapter 5, movement was still an issue, especially at longer distances, even with relatively stable mounts. If small pointing errors caused the signal to move outside of the pixels of interest selected for processing, SNR would go to zero as the signal was lost. While human vision is robust in tracking objects, in vehicular implementation a combination of optical flow tracking and repeated preambles will be required for the receiver to track signals across the frame. In our experimentation, we avoid these complications in the receiver software by focusing on cases where the signal was relatively static.

Assessing simple low-cost modifications to the camera phone, wavelength (color) and polarization filters were mounted in front of the smartphone. A 3D printed bracket (see Appendix D for details) accepting a 55 mm camera lens suspended the filters directly in front of the Pixel 6a camera sensor. To support multiple receive camera configurations, an additional 3D printed mount that could hold two Pixel 6a camera phones simultaneously on the same tripod. For very long-range communications — in excess of 1.6 km — a Celestron Outland X 20× monoscope was used for magnification. This monoscope is only 16 centimeters long and could be fitted in a vehicle. In vehicular deployment configuration, a more compact lens configuration could be used as some camera phones can already approach 15× magnification organically [121].

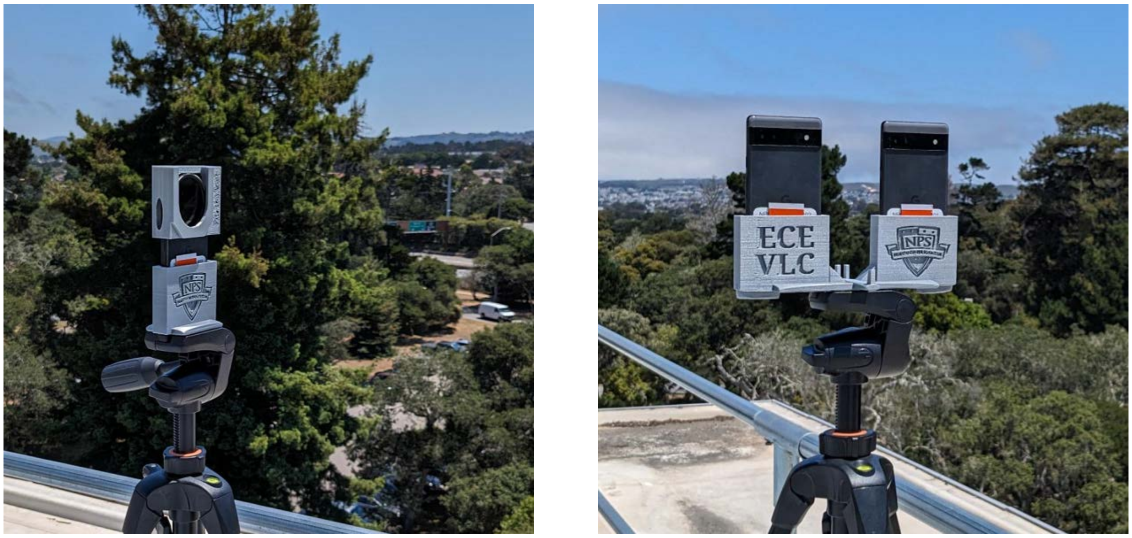

(a) (b)

Figure 4.3. (a) Single and (b) dual mounts for collection on the roof of the engineering building.

4.3 Test Geometry and Atmospheric Conditions

A key requirement of VVLC communication is functionality outdoors in sunlight at longer ranges than can be achieved in a lab. We conducted testing along the roof of the Naval Postgraduate School engineering building, facilitating ranges up to 130 m in broad daylight. To reach ranges slightly over half a kilometer, we transmitted from the roof of the engineering building across the campus. This range of 550 m is beyond what has been reported in any other outdoor VLC literature to date and is far enough to meaningfully pass critical information between vehicles such as speed or the need for upcoming emergency braking. We found that at 550 m, using 2× zoom natively in the phone, our headlight filled less than one pixel. Stepping up to 20× magnification, which does not require unreasonably large optics, we established communications at over 1.6 km from the roof of the engineering building to a wharf across Monterey Bay. This geometry is shown in Figure 4.4.

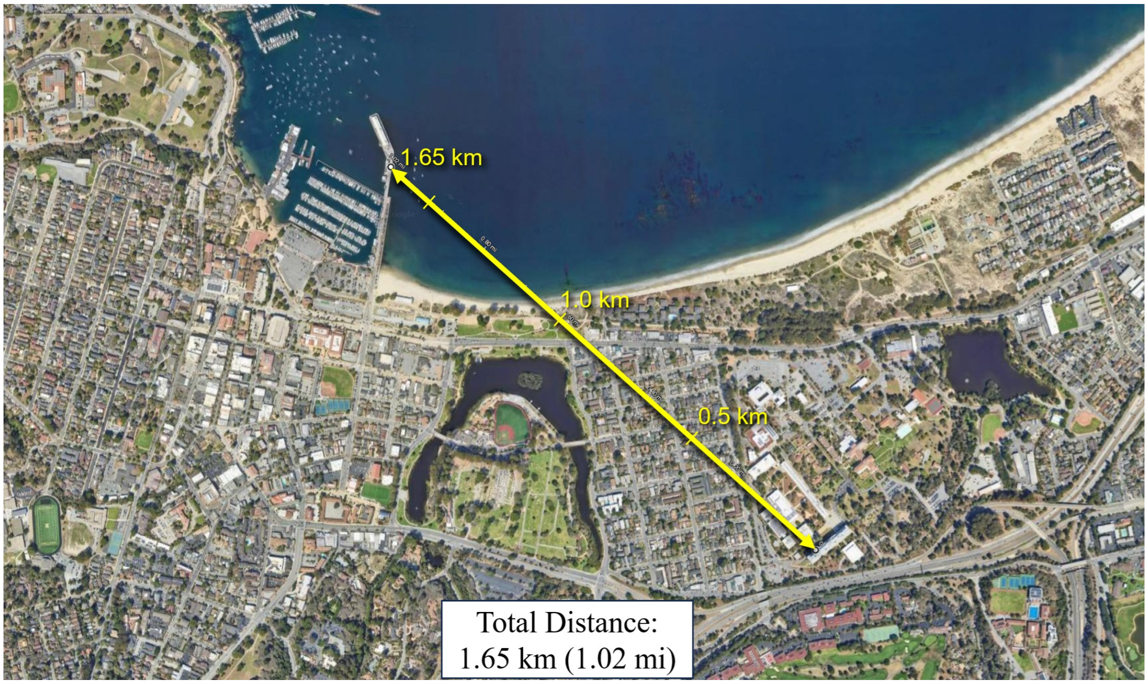

Figure 4.4. The 1.65 km test range from the roof of the engineering building to the municipal wharf in Monterey. Adapted from [122].

4.3.1 Range and Resolution

As range increases, more of a scene can be seen by a camera. The angle defining what is included in this cone of vision is called the angle of view and the ultimate resulting scene is contained in the FOV. The size of the image plane — the sensor in the camera — and the focal length between the optical center of the lens assembly and the image plane defines a similar triangle with the field of view at any given range, as shown in Figure 4.5.

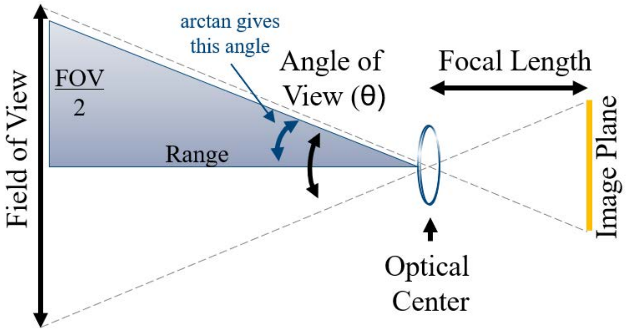

Figure 4.5. The field of view includes more scene area as the subject moves farther from the camera.

From the Pixel 6a specifications, the IMX363 sensor is 4032×3024 pixels, at a pixel pitch of 1.4 μm, for a total width of about 5.645 mm [123]. Google Support provided a focal length of 4.38 mm [124]. From these two numbers, we calculated the angle of view,

$$\theta = 2 \arctan \left(\frac{\text{Image Plane}}{2 \times \text{Focal Length}} \right), \tag{4.1}$$

as 1.145 radian (about 66°). A typical value for natural-looking images is around 70°, and the result is consistent with expectations. To validate our calculation, we measured the distance from the Pixel 6a camera to a meter stick, until the edges of the meter stick filled the entire frame as shown in Figure 4.6. The default camera mode requires a range of 80 cm for a meter stick to fill the Pixel 6a screen. Again applying Equation 4.1, this gives an angle of view of 63°, within 3° of our calculation even given the imprecision in the meter stick method. Shifting to video recording mode with 2× zoom — which still preserves a one-to-one optical pixel fill at 1080p without requiring digital stretching — we measured the angle of view to be 30°.

Figure 4.6. Calibrating the Pixel 6a FOV by recording a meter stick.

In order to calculate the scene area included in any given pixel, $\mathcal{P}_{FOV}$, we can apply the similar triangles concept from Figure 4.5 and subdivide the FOV by the number of pixels across the image plane

$$\mathcal{P}_{FOV} = \frac{\text{FOV}}{W_{\mathcal{P}}} \tag{4.2}$$

where FOV is calculated from the range and angle of view as described in Equation 4.1 and the $W_{\mathcal{P}}$ is the number of pixels across the image plane.

Using the Pixel 6a recording video at 2× zoom, we conveniently find that $\sin(30^\circ) = 1/2$. As such, the FOV in this recording mode is simply half of the range. Subdividing the FOV by the number of pixels — 1920 being the greater dimension of a 1080p recording — we can find $\mathcal{P}_{FOV}$ by applying Equation 4.2

$$\mathcal{P}_{FOV} = \frac{130 \times \sin(30^\circ)}{1920} = 0.03385 \text{ m/px}, \tag{4.3}$$

which shows that 3.385 cm of scene is included in each pixel.

The transmitting crescent-shaped area of our headlight was about 8 × 6.5 cm, and as seen in Figure 4.7, roughly aligning with a 3 × 2 area, which at 3.385 cm/px gives an area of 10 × 6.77 cm.

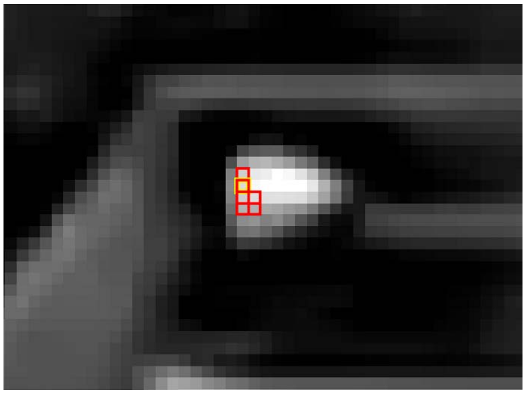

Figure 4.7. The pixels filled by the transmitting area of the headlight at 130 m align with FOV calculations based on the measured 30° observed in the recording configuration. Note that the bright white area to the right of the highlighted pixels is not the headlight transmitting, but simply glare from the ambient sunlight.

Given a known transmitter size, we can manipulate Equation 4.2, setting $\mathcal{P}_{FOV}$ equal to the size of the transmitter to normalize the equation,

$$\mathrm{Tx}_{size} = \frac{r \times \sin\theta}{W_{\mathcal{P}}} \tag{4.4}$$

and then number of pixels filled on the camera sensor, $\mathcal{P}_{fill}$, at any range can be determined from

$$\mathcal{P}_{fill} = \frac{\mathrm{Tx}_{size} \times W_{\mathcal{P}}}{r \sin\theta} \tag{4.5}$$

where r is the distance from the camera, θ is the angle of view, and $W_{\mathcal{P}}$ is the length of the sensor in pixels along the longer dimension.

In engineering an optimal communication system, we may need a minimum number of pixels to support noise mitigation (see Section 5.1.1) or allow a tolerance for movement in the scene. If we know the minimum number of pixels that must be filled to retain reliable communication, we find the maximum range at which we support communication as

$$r_{max} = \frac{\mathrm{Tx}_{size} \times W_{\mathcal{P}}}{\mathcal{P}_n \times \sin\theta} \tag{4.6}$$

where $\mathcal{P}_n$ is the number of pixels needed in a row or column of the image.[4]

4.4 Signal Localization

Having established the size of the signal on the receiver array we still need to localize the signal in time and space in order to recover the transmitted data. For purposes of experimentation, we assume a fairly stable scene foregoing the complications of tracking mechanically with gimbals or digitally through video processing with optical flow. Even assuming that the transmitter is not moving in the scene, we still need to find it in the received pixel matrix.

4.4.1 Spatially Localizing the Signal

Localizing the transmitter in space is a nontrivial challenge. In some previous literature, it was assumed that simply selecting the brightest point in the scene would always capture the transmitting light source [125]. However, outside in daylight conditions, there may be many competing sources of brightness — from clouds to glare and reflection — and a peak brightness method of detection and tracking is unreliable. Beyond peak brightness, one could look for peak spectral content. The entropy of encoded data produces detectable frequency components. A detector designed to localize peak entropy, rather than peak brightness, was successfully demonstrated in indoor conditions to isolate malicious optical transmitters [126].

---

[4] We have used linear pixel counts throughout this derivation. If application code instead focuses on area, for example needing 16 pixels in a 4×4 area, a square root would be needed to account for the difference between linear units and square units.

Challenging this technique, the outdoor environment contains numerous frequency sources, some with very strong components throughout the camera sampling frequency spectrum. Branches sway and leaves rustle in trees. Mirages rise from hot surfaces and water shimmers with waves. Solid structures have high contrast edges, so slight movement on the image plane from turbulence in the air or minuscule camera shake creates lines of strong frequency components at the edge of solid objects.

Ultimately — rather than seeking frequency content alone — we focus on detecting the very specific frequencies included in our data preamble. This technique is robust to other bright sources in the environment and rejects most other frequency content including nearly all the natural noise discussed above. Leveraging the preamble consisting of 32 cycles of high and low intensity at 30 ms per bit, a spectral energy detector scanned for pixels with large 16.667 Hz components.

We processed videos in MATLAB to map spectral components. First, MP4 files directly recorded on the Pixel 6a were imported. Then the three color channels were flattened into a single gray scale luminance value for each frame. From the 1920×1080 image, an 80×60 chip was selected and stored for further processing steps. This technique provides significant savings in compute time. Processing only chips — rather than the whole video frames — requires less memory and processor cycles. Chipping areas of interest most likely to contain signals is a viable approach for VVLC, where we anticipate receiving signals from other cars somewhere along the roadway. Using a larger sensor area allows more tolerance for safety on curves in the road and handling vehicles both near and far away, while sampling chips of the scene is likely sufficient to spatially isolate signals.

Within each chip, spectral energy at the preamble frequency was assessed at each pixel. The vector containing the pixel luminance values for the entire duration of the video was dot multiplied by a sine and cosine at the preamble frequency, and the sum of the squares of the two dot products outputs was used to capture total energy at the preamble frequency

$$\varepsilon = \left(\overrightarrow{P_x} \cdot \overrightarrow{C}\right)^2 + \left(\overrightarrow{P_x} \cdot \overrightarrow{S}\right)^2 \tag{4.7}$$

where P_x is a vector of pixel luminances and C and S are equal length vectors of $\cos(f)$ and $\sin(f)$ respectively, with f as the preamble frequency. Since we are only handling one video at a time, there was no need to normalize by the length of the video, which was consistent across all pixels.

Figure 4.8 shows an exemplar result of plotting these values across all pixels in a chip as a mesh. The shape of the transmitting area of the headlight rises steeply above the background noise floor at the preamble frequency, with a small roll-off around the corona of the light.

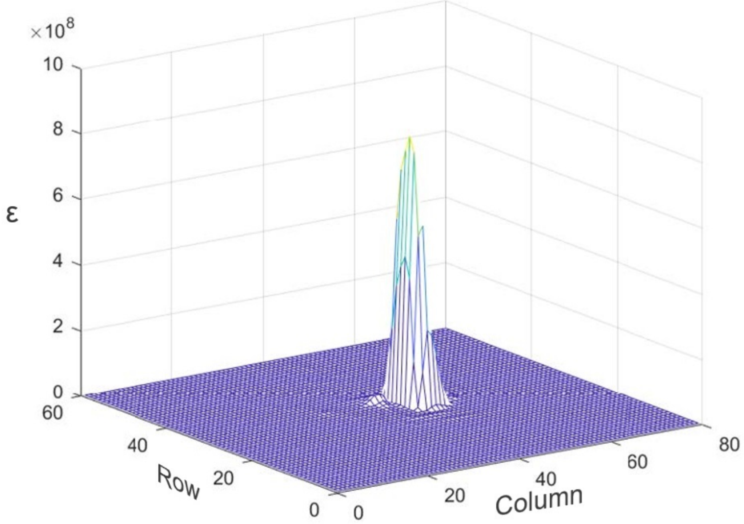

Figure 4.8. Meshing showing the 16.667 Hz energy in a chip of a scene at 130 m.

Overlaying these results on the chip from the scene itself in Figure 4.9, we see the transmitting area of the headlight very well localized. The yellow box marks the peak energy at the preamble frequency, in the center near the transmitting bulb itself, and the remaining red boxes contain everything within 3 dB of that peak. The bright glare on the right half of the headlight is ignored despite it being the brightest area in the scene, since it does not contain the frequency of interest.

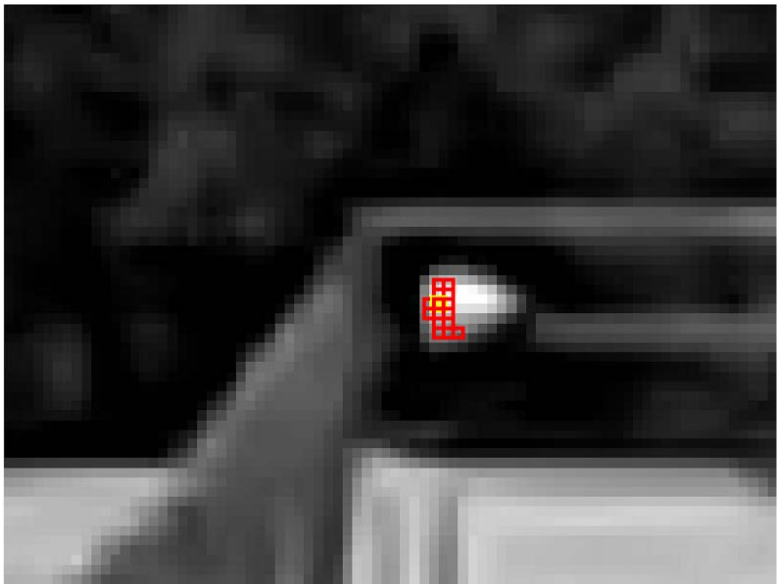

Figure 4.9. Overlay of the pixels within 3 dB of peak power at 16.667 Hz.

4.4.2 Temporally Localizing the Signal

After identifying areas with strong spectral correlation to the preamble, a matched filter was used to establish timing. The header was sifted across the values of the pixel with the strongest correlation to identify the start of the signal in time. Since we are using a global shutter, establishing the signal start time based on this one-pixel vector also establishes the start frame for the signal across all other pixels in the video. The cross-correlation of the preamble with the signal at varied lags is shown in Figure 4.10. The maximum value in Figure 4.10, near a lag of 200, corresponds to the frame at where the preamble started in the received video. Data bits start after an offset the length of the preamble and preamble-data pause. An overlay of the bit masked on the received signal is presented in Figure 4.11, showing strong alignment with expected bit bin edges. Using a preamble to detect timing avoids dependencies on the data itself. An energy detector, without a preamble, would encounter timing errors if leading data bits were zeros. The use of a preamble allows both spatial and temporal localization of VLC signals.

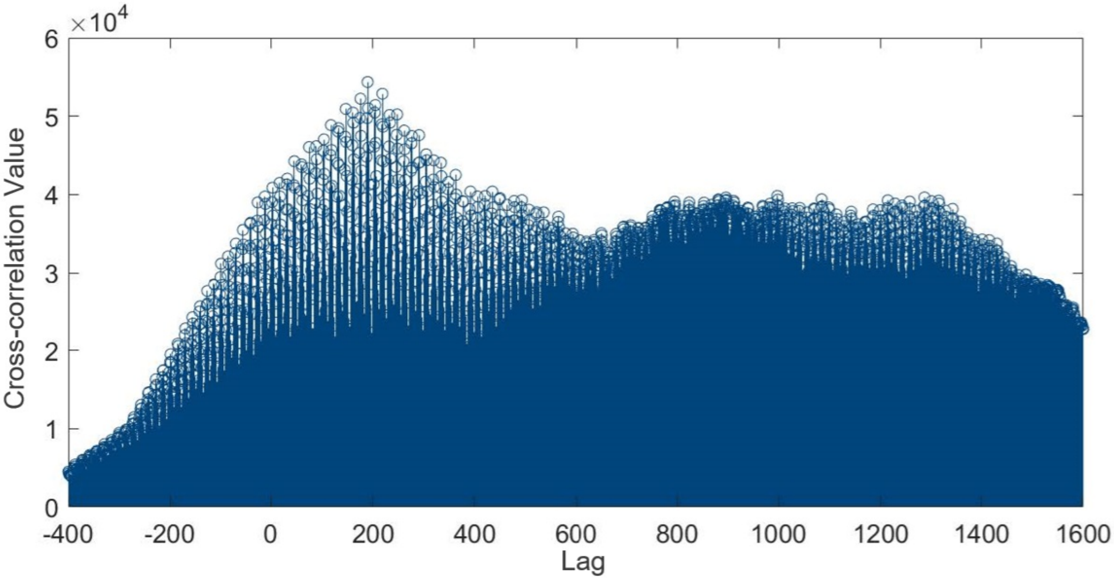

Figure 4.10. Cross-correlating the preamble with the received signal identifies the start of the preamble near a time lag of 200, which in turn identifies timing of the following data bits.

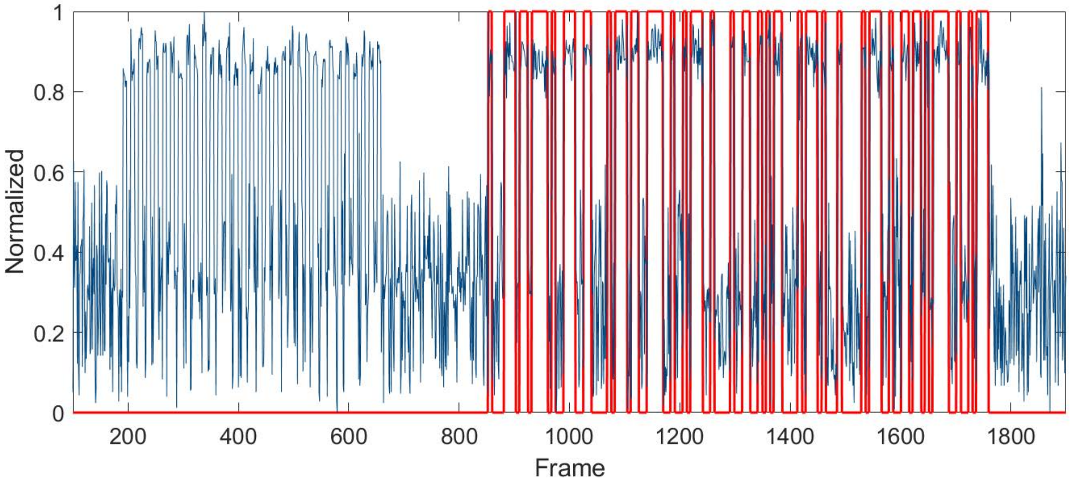

Figure 4.11. Based on the timing established by matching the preamble, timing of the received signal bits (in blue) aligns cleanly with a mask of the transmitted bits (in red).

4.5 Quantifying Signal-to-Noise Ratio

SNR is the ratio of the received power over the noise power, as we introduced in Section 2.4. SNR is our benchmark for performance, and this section expounds on our method for quantifying it from the recordings. Momentarily returning to the fundamentals, electrical power supplied by a DC current is simply

$$P = V \times I \tag{4.8}$$

where P is power, V is voltage, and I is current. Combining this with Ohm's Law, $V = I \times R$, where R is resistance, we can see

$$P = V \times I = V \times \left(\frac{V}{R}\right) = \frac{V^2}{R}\,, \tag{4.9}$$

and power is proportional to the voltage squared. For the purpose of calculating SNR, we can assume unity resistance since constant terms in the numerator and denominator would cancel. With $R = 1$, power is simply voltage squared.

While this seems straightforward, at the receiver we do not have access to the attenuated signal nor the noise alone, only the superposition of the two. To calculate received SNR, we must extract the amplitudes of the received power and the received noise, as shown in Figure 4.12, where the amplitudes on the left and right are to scale. If we had access to the separate signal and noise on the right of the figure, the calculation of SNR would be straightforward. Signal power is found as the difference between a high and low value squared (recalling Equation 4.9).

Since noise appears more unpredictable, measuring the amplitude difference is not as intuitive as the square wave case. However, we can still find the average power by integrating over the period of interest. Average power is given by

$$P_{avg} = \frac{1}{t_2 - t_1} \int_{t_1}^{t_2} \frac{v(t)^2}{R} dt \tag{4.10}$$

and is equivalent to Equation 4.9 if $t_2 - t_1 = 1$, but is more flexible in implementation. The equation to calculate the variance of a discretely sampled signal is

$$\begin{aligned} Var(X) = \sigma^2 &= E[(X - \mu)^2] \\ &= E[X^2] - E[X]^2 \\ &= \frac{1}{n}\sum_{i=1}^{n}(x_i - \mu)^2 \\ &= \frac{1}{n}\sum_{i=1}^{n}(x_i)^2 \end{aligned} \tag{4.11}$$

and if the mean, μ, is zero, this reduces to a time average of the amplitude squared, equivalent to Equation 4.10. Thus, to find noise power, we simply take the square of the noise signal with the mean removed.

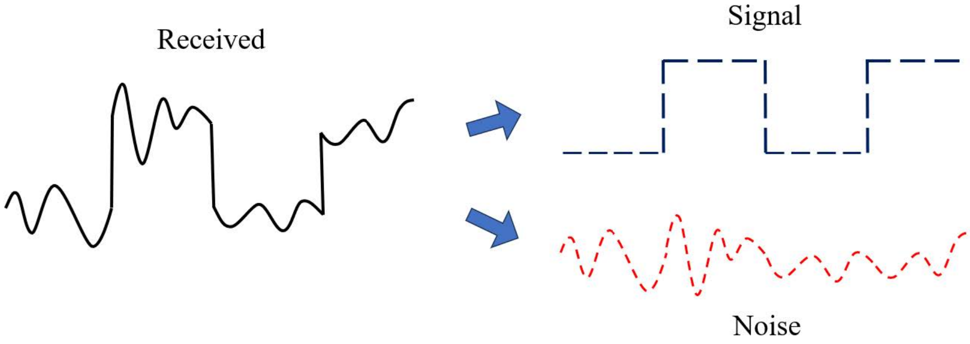

Figure 4.12. The received signal on the left is the only information available at the receiver. In order to calculate SNR, we need to separate the signal from the noise.

We now describe our method for separating the signal and noise components of our receiver output. We begin by assuming that SNR for the system is greater than one. At an SNR of one, the signal and the noise have the same power, which precludes sorting of signal bins with any threshold. Working from the assumption that signal power is greater than noise power, we separate the received ones and zeros to allow further analysis. Assuming SNR is greater than one, even in noise most one bits will be greater than most zero bits. We also know that our transmitted signals are crafted such that there are an equal number of ones and zeros. Equiprobable occurrences of bits is generally a reasonable assumption, but for experimental purposes, we know it to be true.

In order to establish the value of a one, we take the mean of the greatest 50% of the bit bins, leveraging the fact that noise is generally Gaussian in Section 3.3. The value of a zero bit is found in the same manner. Note, this is not the mean of any one bit bin, but rather the mean across all ones and then the mean across all zeros. In Figure 4.12, if you drew in imaginary lines at the average of the high and low values on the left, you would get a shape very similar to the signal alone on the right. Having the high and low values of the approximated signal alone, the difference squared gives us signal power.

In order to approximate the noise alone, we subtract the approximated signal. Envisioning this, if you took the signal alone on the right of Figure 4.12 and subtracted it from the received signal of the left, you would be left with the noise alone in the lower left. This is fairly straightforward, but since we know that noise power varies between high and low bits, we initially handle the grouping of the greatest 50% and lowest 50% of the bit bin separately. Having the distinct standard deviations of the ones and zeros becomes important for determining the optimal decision threshold, which will be discussed in Section 4.6. In order to calculate overall SNR, we then recombine them, essentially averaging the two since bits are equiprobable, and the variance is the overall noise power. Having approximated both the signal and noise power, their ratio is the SNR.

The experimental results presented in Chapter 5 use this process of calculating SNR over at least twelve video files for every filter configuration at every distance. Typically, fifteen to twenty videos were recorded for each configuration, and all usable results were included. However, during experimentation, excessive equipment movement or LOS obstructions were occasionally observed. The results from these trials were removed before calculating statistics. Bar charts show the mean SNR of all valid trails in each configuration and error bars show one standard deviation.

4.6 Calculating Bit Error Rate and Decision Thresholds

Despite our focus on SNR, the BER and SNR are closely intertwined and a review of BER informs the optimal decision threshold we employ to decode binary data. Assessing BER to establish our optimum detector, we begin with a quick review of error probability of a binary channel. This provides an important result due to the asymmetry that we saw in Section 3.2.1 and, in turn, working through the process of setting the selection threshold informs the selection of SNR as our primary metric for communication improvement.

In a binary system, an error will occur when the bit received is not the bit sent. In the simplest case, the probabilities are symmetric both in the likelihood of either bit being sent and the probability it will be received correctly. That is, ones and zeros are both transmitted with a probability of 0.5, and the chance a zero is received as a one is the same as a one being received as a zero.

The binary channel, shown in Figure 4.13, allows for easy traceability of the law of total probability.

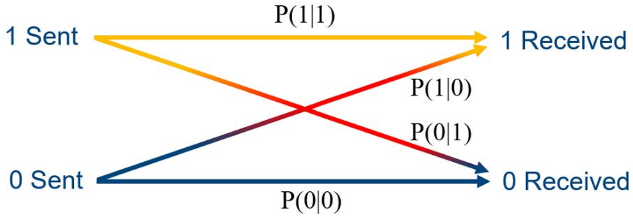

Figure 4.13. The probability diagram for a binary channel, showing probabilities of correct and incorrectly decoded bits given the bit transmitted.

We want to minimize the probability of errors, so assuming equiprobable transmission of ones and zeros we seek

$$\arg\min \sum \mathrm{P}(0|1) + \mathrm{P}(1|0) \tag{4.12}$$

where P(0|1) is the conditional probability of the error condition where a one is sent and zero is decoded and vice versa for P(1|0). Given the law of total probability — that the sum of all probabilities must be one — minimizing error will necessarily maximize correctly decoded bits.

From Section 3.3, we have seen that our channel noise can be approximated as Gaussian, but recalling 3.2.1 we know the variance for the two transmitted bits will not be the same. While we will continue to assume equal likelihoods of bits being transmitted into the channel, we know from Section 3.2.1 that there is more noise for zeros than ones, so the error probabilities are not equal. Figure 4.14 illustrates the need to offset the detection threshold. Any area under a tail of normal distribution on the opposite side of the intended bit average results in an error, so a simple mid-point threshold detector does not minimize error.

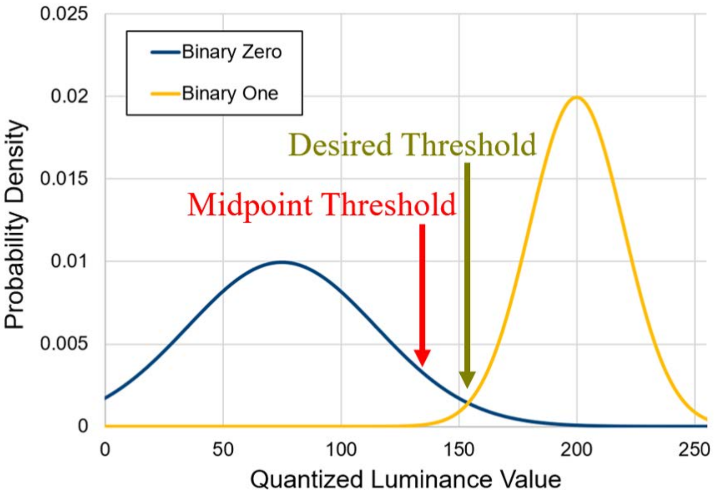

Figure 4.14. A bit error occurs if a received pulse is on the opposite side of the threshold from the transmitted pulse. Setting an equal area for these two tails, which can be calculated from the Q-function, rather than using the midpoint between means, minimizes the probability of bit error.

The area under the upper tail of a Gaussian distribution can be found by integrating from the threshold value to infinity

$$\mathrm{P}(1|0) = \int_{t}^{\infty} \frac{1}{\sigma_0\sqrt{2\pi}} e^{-\frac{1}{2}\left(\frac{x-\mu_0}{\sigma_0}\right)^2} dx \tag{4.13}$$

where t is the threshold value, μ_0 is the mean received values of a zero sent, and σ_0 is the standard deviation of the received value of a zero sent. The error tail for a zero received given a one was sent can be found in a similar manner integrating from negative infinity to the threshold.

To allow for more concise notation, the Q-function is defined as the area under the positive tail of the standard Gaussian distribution

$$Q(x) = \int_x^\infty \frac{1}{\sqrt{2\pi}} e^{-\left(\frac{u^2}{2}\right)} du \tag{4.14}$$

which is equivalent to Equation 4.13 with a zero mean and unit variance. The Q-function is defined only for the positive tail but, by symmetry, the area under the positive and negative tails are the same, as seen in Figure 4.15.

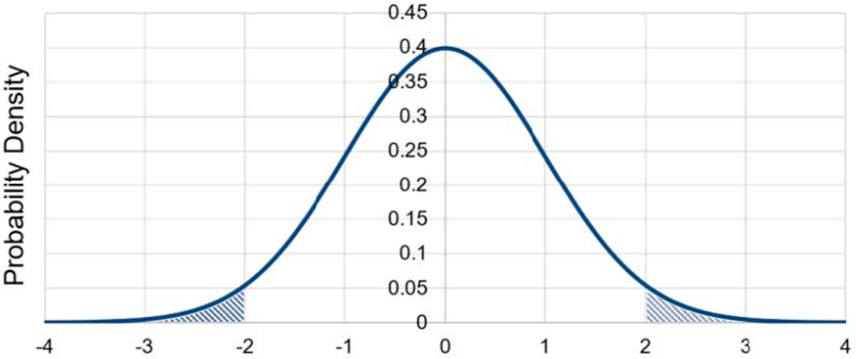

Figure 4.15. While the Q-function only calculates the probability area under the positive tail, by symmetry, the positive tail probability is equal to the negative tail probability, as shown here on a zero mean, unit variance Gaussian.

With this in mind, we can derive the optimum threshold for a non-symmetric binary channel. Due to the exponential shapes of the two PDFs, the arg min for Equation 4.12 is found when P(0|1) = P(1|0). Setting the two tails equal we have

$$Q\left(\frac{t-\mu_0}{\sigma_0}\right) = 1 - Q\left(\frac{t-\mu_1}{\sigma_1}\right) = Q\left(\frac{\mu_1 - t}{\sigma_1}\right) \tag{4.15}$$

with the sign flip on the error from μ_1 allowing for the application of Gaussian symmetry to the Q-function. Since the Q-function is one-to-one, we can effectively take the inverse of the Q-function, which we will denote as Q^{-1},

$$\begin{aligned} Q^{-1}Q\left(\frac{t-\mu_0}{\sigma_0}\right) &= Q^{-1}Q\left(\frac{\mu_1-t}{\sigma_1}\right) \\ \left(\frac{t-\mu_0}{\sigma_0}\right) &= \left(\frac{\mu_1-t}{\sigma_1}\right) \end{aligned} \tag{4.16}$$

yielding a simpler, algebraic relationship. Finally, through algebraic manipulation, we arrive at the equation for the ideal threshold

$$t = \frac{\mu_0\sigma_1 + \mu_1\sigma_0}{\sigma_1 + \sigma_0} \tag{4.17}$$

which can be dynamically updated in our receiver to return the lowest possible BER.

A noteworthy corollary: the numeric result of the Q-function is also the total probability of error. Since the total probability of error is the sum of P(0|1) and P(1|0), assuming P(1) and P(0) are both 0.5 (it is equally likely a one or a zero is initially sent)

$$\mathrm{P(bit\ error)} = 0.5 \times \mathrm{P}(0|1) + 0.5 \times \mathrm{P}(1|0) \tag{4.18}$$

and since Equation 4.17 establishes that P(0|1)=P(1|0) we can simplify this to

$$\begin{aligned} \mathrm{P(bit\ error)} &= 2 \times 0.5 \times \mathrm{P}(0|1) = \mathrm{P}(0|1) = Q\left(\frac{t-\mu_0}{\sigma_0}\right) \\ &= 2 \times 0.5 \times \mathrm{P}(1|0) = \mathrm{P}(1|0) = Q\left(\frac{\mu_1-t}{\sigma_1}\right) \end{aligned} \tag{4.19}$$

and the evaluation of either Q-function by itself from the optimal threshold returns the optimal BER for the asymmetric channel assuming a Gaussian noise model.

CHAPTER 5:
Signal-to-Noise Ratio Improvement Techniques

This chapter presents techniques to increase SNR through noise mitigation, the core focus of this dissertation. A broad overview of the assessed noise mitigation methods is provided in Figure 5.1. First among these noise mitigation techniques is the application of spatial filtering to reject as many signal-free pixels as possible. Spatial filtering may be achieved with optics or software. Next, we test exploiting spectral differences between light sources and background illumination. We investigate whether rejecting certain bands and polarization by filtering could boost the relative amount of signal to noise. Finally, the use of optics and multi-camera systems is assessed.

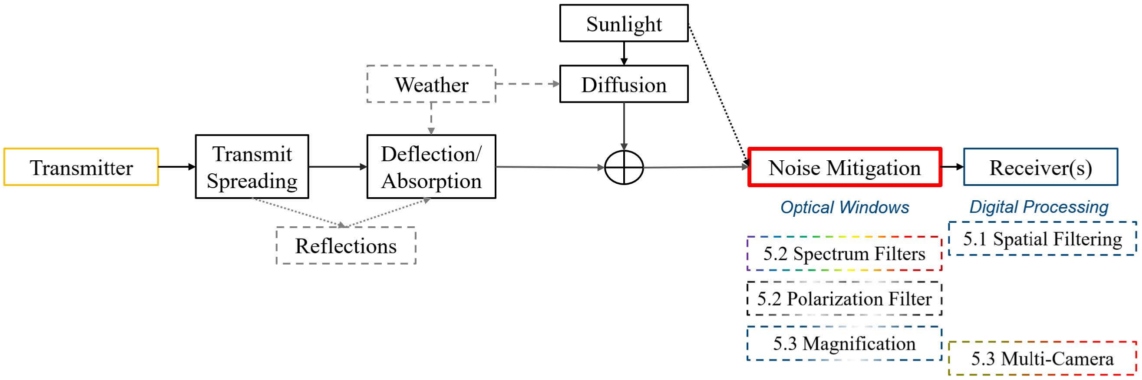

Figure 5.1. Building on Figure 3.1, in this chapter we assess noise mitigation techniques to improve received SNR. Optical filters and magnification are used to precondition light arriving at the camera, and digital selection in the camera emphasizes signal while rejecting noise.

5.1 Spatial Selection to Capture Signal and Reject Noise

Throughout the literature, spatial filtering has been applied as a means of increasing SNR in VLC, both using photodiodes and CMOS arrays as receivers [28], [127]. Any light reaching the sensor that is not signal degrades SNR. One approach that can help both photodiodes and imaging sensors is limiting the FOV. A tube or barrel can be used to constrain the scene and limit extraneous energy arriving laterally into the sensor. However, limiting FOV increases receiver size and creates additional challenges with sensor alignment.

Leveraging a typical OCC configuration, the camera has a lens that concentrates the desired portion of the wavefront onto the CMOS sensor array, and the CMOS sensor array has further micro-lenses that concentrate light on the individual photo sites. By selecting only pixels of interest, there is an inherent aperture constraining effect, and Equation 2.3 applied to the selected area of interest on the array becomes

$$\mathrm{SNR} = \frac{\sum_{\mathrm{px}} P_{sig}(\mathrm{px})}{\sum_{\mathrm{px}} P_{N}(\mathrm{px})} \quad \forall\ \mathrm{px} \in \mathrm{ROI} \tag{5.1}$$

and omitting any pixels that are just noise increases SNR. This result has been experimentally verified [128].

Previous research on low-density parity check coding OCC showed region of interest (ROI) selection aided in thresholding to isolate signals [129]. Our exploratory work on other optical communication projects has verified the importance of spatial filtering [46]. Any processed pixel that did not include the transmitter contributes noise power while adding no signal power, reducing the overall SNR. By constraining the area processed to near the transmitter in the scene, SNR is greatly enhanced. Advanced image processing techniques measuring optical flow to track vehicles in a V2V scene suggest the ability to maintain consistent SNR as long as the brightest pixel can be selected [125].

It has been shown that leveraging multiple pixels increases SNR. Ashok et al. derived the SNR increase in an imaging sensor over a single photodiode if the light source is close enough to illuminate multiple pixels [130]. When the transmitter is far enough away to only illuminate one pixel, the SNR reduces to the photodiode case. For a single photodiode, Ashok referenced Kahn and Barry’s seminal work on IR communications [131], where received signal power is $P_{Rx} = (RhP_{Tx})^2$ where h is the DC channel gain and R is the receiver optical conversion sensitivity. Noise impacting the received signal is assumed to be AWGN with a power spectral density (PSD) per unit area of $S(f) = qRP_n$ where q is the charge of an electron and P_n quantifies the power in background light per unit area.

Thus, with a sample rate of W, noise power is $P_N = qRP_nAW$, providing an overall single transmitter-single photodiode SNR of [130]

$$\text{SNR}_{pd} = \frac{P_r}{P_N} = \frac{\kappa P_t^2 d^{-4}}{qRP_nAW} \tag{5.2}$$

where κ is a function of the transmitter radiation pattern, angles, FOV, and receiver optical gain.

If the receiver is within a critical distance from the transmitter, d_c, the transmitter will illuminate multiple pixels, allowing rejection of areas that are only noise. This critical distance is $d_c = fl/s$, where f is the focal length of the optics, l is the diameter of the transmitter, and s is the edge-length of a pixel (recall Equation 4.2). Beyond d_c, this reduces to Equation 5.2 where $A = s^2$. Ashok et al. provides the SNR for each case as [130]

$$\text{SNR}_{cam} = \begin{cases} \frac{\kappa P_t^2 d^{-2}}{qRP_nWf^2t^2} & \text{if } d < d_c \\ \frac{\kappa P_t^2 d^{-4}}{qRP_nWs^2} & \text{if } d \geq d_c \end{cases} \tag{5.3}$$

and within d_c, a substitution of the critical distance formula squared shows an SNR gain of d^2 as more pixels are filled. While Ashok's derivation is optimistic to assess a gain on the order of d^2, there is clearly a significant gain to be had over the single photodiode case. If the wavefront can be spread across more pixels, the cumulative power of the arriving signal grows at a faster rate than the sum of uncorrelated noise powers — such as graininess produced by Johnson noise or pixel imperfections — improving SNR. While daylight wavefront noise drastically dominates internal camera noise in overall power, we will further investigate the impact of wavefront magnification in Section 5.3.1.

5.1.1 Pixel Inclusion for Array Gain

Beyond rejection of noise, pixel selection enables array gain for VLC. RF array gain calculations establish our baseline, but derivations of RF array gain are based on several assumptions about the characteristics of noise and the propagation environment which do not directly translate to optical frequencies. As a prime example, the PSD of thermal noise is considered constant for most frequencies of interest in the RF, but not at optical and infrared [114]. However, Shannon noted that the entropy power of any noise can be modeled and compared to a Gaussian, where AWGN is the worst of all possible noises [35].

Most RF MIMO array gain equations make an assumption the receiver spacing must be greater than approximately $\lambda/2$. This assumption is based on stochastic models of the RF channel, expecting fading and multi-path to decorrelate the received signal sufficiently to achieve reasonable eigenvalues. RF propagation is generally modeled with a Rayleigh distribution assuming a sufficient number of scattering events that the central limit theorem will generate a Gaussian distribution of phase (between 0 and 2π) at the receiver. However, VLC have an overwhelming LOS path and our receiver provides no useful phase information. In fact, the primary LOS path is so strong that even a Rician fading model is unnecessary. Rician fading occurs when just a few strong reflections cause interference with the LOS path rather than a large number of reflections (and potential absence of a LOS path) in the Rayleigh fading model.

For outdoor VLC, we expect the LOS signal path will be unperturbed by ISI since the variation in propagation time will be significantly shorter than symbol periods. Further, reflections in the environment can be captured separately via the spatial diversity of the imaging sensor to actually enhance the total received signal. The RF MIMO spacing assumption of $\lambda/2$ is based on relative phase at the receiver, which is not available for VLC intensity detection. Pixel spacing nonetheless will be larger than $\lambda/2$. A typical CMOS sensor pixel pitch is 1.4 μm, while the longest wavelength of red light captured by the sensor is 0.75 μm. Individual pixels are thus typically space at least 2λ apart, well beyond $\lambda/2$.

In all cases, array gain, G, is defined as the relative improvement in SNR over the single sensor case

$$G \equiv \frac{\text{SNR}_{array}}{\text{SNR}_{sensor}} \tag{5.4}$$

which provides a normalized ratio of signal and noise power [132]. Expanding on Equation 2.3, the SNR at any individual sensor element is

$$\mathrm{SNR}_{element} = \frac{\mathbb{E}[s^2(t)]}{\mathbb{E}[n^2(t)]} = \frac{\mathrm{R}_s(0)}{\mathrm{R}_n(0)} \tag{5.5}$$

where power can be calculated either as the expectation of the sample value squared or the autocorrelation sample set, $\mathrm{R}(\tau)$, evaluated at zero lag assuming a wide-sense stationary process.

Each component in the receive array could have a different weight, w_n, allowing optimization based on specific filters or paths from the sensors. In RF arrays these weights are valuable for beam forming and array optimization based on the array geometry and propagation characteristics of the field and noise. At optical frequencies, we will focus on uniform weights before considering other optimizations based on color and polarization in Section 5.2. Assuming stationary random processes,

$$\mathrm{SNR}_{array} = \frac{\mathrm{R}_s(0)\ \left|\sum_1^n w_n\right|^2}{\mathrm{R}_n(0)\ \sum_1^n \left|w_n^2\right|}. \tag{5.6}$$

Calculating array gain, normalized by SNR as defined in Equation 5.5, the power terms cancel leaving

$$G = \frac{\left|\sum_1^n w_n\right|^2}{\sum_1^n \left|w_n^2\right|}, \tag{5.7}$$

which is only a factor of the weights [132]. Assuming that all weights are unity, this provides

$$G = \frac{\left|\sum_1^n 1\right|^2}{\sum_1^n \left|1^2\right|} = \frac{n^2}{n} = n \tag{5.8}$$

showing array gain linearly increasing with additional receivers. Viewed another way, the relative noise in the output of the receiver array is reduced by a factor of $1/n$.

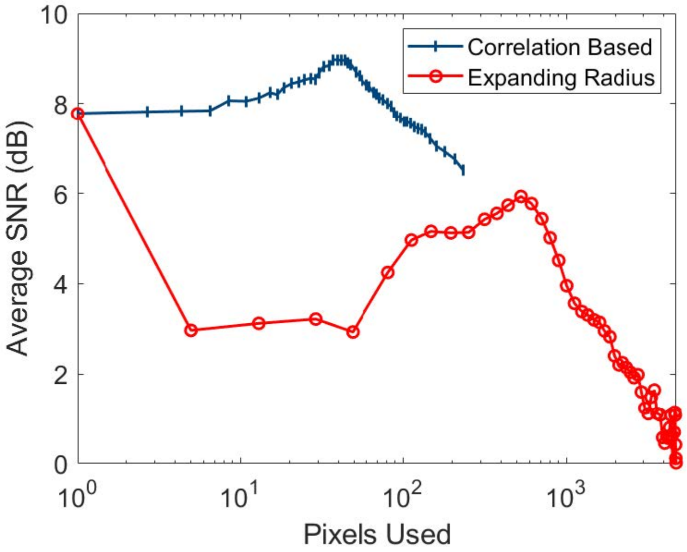

Figure 5.2. Average SNR in 13 signal recordings with varying pixel inclusion. Pixel selection based on the strength of the correlation to the preamble in an 80×60 chip of the video (as introduced in Section 4.4.1) outperforms a simple radial geometric expansion. Including more pixels with signal improves SNR, while additional noise-only pixels dilute SNR. Selecting pixels not only to reject noise but to focus on probable signal maximizes SNR.

Through empirical measurements, we see gains of two or three decibels when ramping up pixel inclusion from 1 to nearly 100 pixels in Figure 5.2. The correlation-based weighting leverages the energy match at each pixel used to localize the signal as was discussed in Section 4.4.1. The expansion follows similar to the shift between Figure 4.7, which captured just the only the greatest 10% of pixels with energy correlated to the preamble, to Figure 4.9, which included the top 50% of pixels correlated to the preamble. While preamble-correlation-based selection is far more robust than a simple expanding circle of pixels, this method still does not approach an ideal factor of *n* gain. This discrepancy can be explained by several phenomena. First and foremost, at 130 m the headlight fills less than 10 pixels, and vastly larger array sizes incorporate more noise but no additional signal. In RF communications, we expect the signal will reach most apertures, but the combination of optical propagation and optics leads to most photons from the transmitter falling only on certain photosites.

Further, we are not ultimately dealing with the wavefront nor photon count directly. Our collection lacks any discernable phase information since the optical frequencies are on the order of 10^{14} Hz, so for a camera sampling at 240 Hz there are on the order of 10^{12} cycles per capture. This captured energy is then quantized to be digitally stored. Quantization undermines the very fine averaging that could be achieved with many photosites, as proximate photon counts are rounded to be the same or simply jump to the next output value. Employing low-cost sensors with 256 quantization bins, we do not approach gains equal to the number of elements. Using different sensors, perhaps multiple high-sensitivity photodiodes pointed at the same point in space, or using optical interferometry, we may find greater gains. These approaches are currently impractical for VVLC implementation.

The discussion above notwithstanding, there is clearly a gain achieved by using multiple pixels, as shown in Figure 5.2. While we are sampling light from different points in the FOV, since all of these points are part of the same transmitter we can assume they are modulated synchronously. Averaging all pixels that contain at least some signal power, we do find relative smoothing of noise which increases SNR. Some area selection techniques are better than others. As seen in Figure 5.2, selection of pixels that are most highly correlated to the preamble, used to localize the signal in Section 4.4.1, achieved rapid SNR gains. However, simple geometric expansion of the region of interest included more noise, resulting in a lower overall SNR.

An equally important reason for averaging an area of pixels is that the transmitter will not be perfectly steady on the receiver array. Throughout our experimentation, we used tripods and mounts in an attempt to stabilize the receiver, and even with a large stable setup there was still motion across the receive matrix due to minor vibrations in the transmitter and receiver as well as atmospheric turbulence and mirage effects. The inclusion of pixels with no signal does degrade SNR, but the loss of signal is far more detrimental when pixels with signal drift outside of the processed area.

In sum, accurate selection of pixels of interest is the most significant challenge in maintaining SNR, and beyond that there are diminishing gains [133]. Optimization that seeks to focus very narrowly on signal pixels is susceptible to the signal drifting out of the area. This would be especially true in vehicular applications where there are numerous sources of movement in the scene. Even with tracking, whether mechanically or through software, it is unlikely that the receiver will be able to precisely fix the signal within an exact set of pixels. At increasing distances, the number of pixels containing signal decreases linearly with increasing FOV. Selecting smaller numbers of pixels increases the likelihood of the whole signal shifting out of a narrowly bounded ROI if a buffer is not used.

5.2 Filtering Approaches to Reduce Daylight Noise

Historically, blue light filtering has been applied to speed up VLC from white PC LEDs by reducing residual phosphor glow [134]. Exotic filters have also been proposed to select and weight narrow bands based on SNR [135]. The focus of this dissertation is robustness in daylight with commodity hardware, so neither of these approaches precisely fits our use case but they both suggest the possibility of gain by exploiting spectral shape.

5.2.1 Color Filtering

As an initial assessment of the SNR gain that could be achieved by selecting specific color pixels from the CFA — rather than equally weighting all of them — we compared the impacts of typical red, green, and blue pigments used in CFAs. Color filters were modeled with a blackbody-like daylight spectrum and a white LED spectrum. Pigment attenuation curves were extracted from [136] and the LED curve was adapted from [137]. The curves for the daylight and LED spectra are shown in Figure 5.3. The peak spectral intensity for daylight was normalized to one and the LED intensity was normalized so they each have the same area under their respective curves.

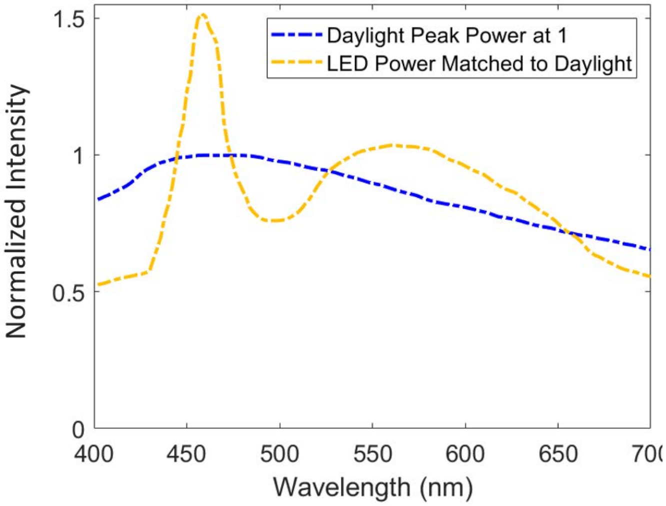

Figure 5.3. Equal power curves for daylight and LED spectra.

Using these baseline curves, the three colors of a typical Bayer CFA were applied, with results shown in Figure 5.4. Using daylight as the base, the percent difference of the power, Δ_P, was calculated as

$$\Delta_P = 100 \times \frac{\int_{400\ nm}^{700\ nm} S_{sun}(\lambda) - \int_{400\ nm}^{700\ nm} S_{LED}(\lambda)}{\int_{400\ nm}^{700\ nm} S_{sun}(\lambda)} \tag{5.9}$$

for each of the three color filters. In the blue filter band, daylight retained 7.1% more energy, counter to our hypothesis that filtering out blue might help suppress blue-sky background in daylight conditions. In the other color bands, daylight was 1.5% lower in the green band and 3.8% lower in the red band. The LED spectrum at equal power across the visible band—even given the strong blue peak seen in Figure 5.3—came through the filters strong in red and green. While the difference discovered suggested an opportunity for SNR optimization, visual inspection of Figure 5.4 shows there is not a large differentiating margin between the filtered spectra. Normalizing by transmit power, all color bands have better than 90% agreement in received power. LED bulbs designed to appear white and CFAs aligned to the tristimulus model of human vision impressively succeed in approximating the spectrum of white light.

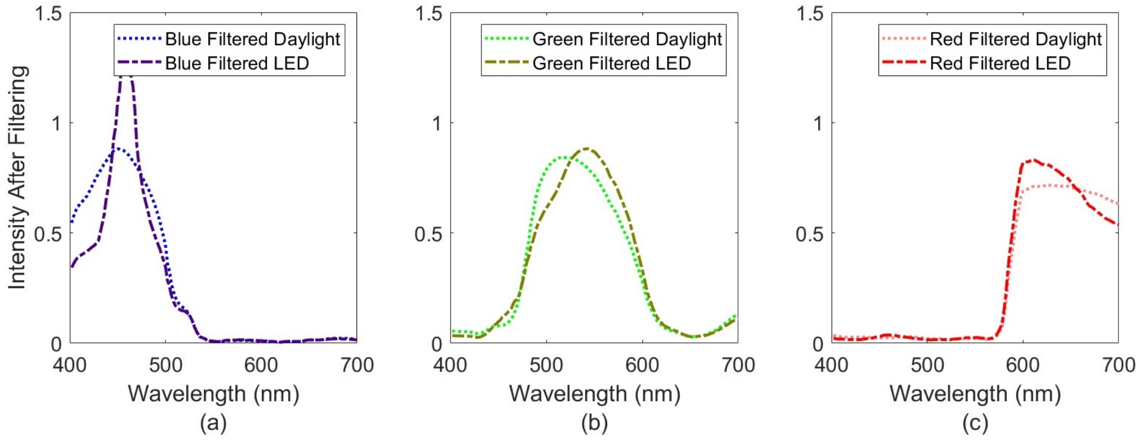

Figure 5.4. Spectral curves after filtering for (a) blue, (b) green, and (c) red.

Still, there may be some room for optimization leveraging the CFA filters or additional layered filters. To achieve higher speeds for VLC, blue pass filters have often been employed to avoid the lag associated with the PC on white LEDs. This is sometimes beneficial for speed, but it has been shown to not always be necessary [138]. The 3.8% relative power advantage of red from artificial lights over sunlight has not been explored in VLC literature. However, in efforts to mitigate sunlight, Eso et al. resorted to employing IR augmenting other light from existing vehicle fixtures [38]. This suggested a bias toward longer wavelengths is beneficial. Shorter, blue wavelengths are Rayleigh scattered more propagating through the atmosphere. However, while red light (620-750 nm) tends to scatter less than blue light, it can experience higher atmospheric absorption due to water vapor and oxygen molecules in the air. The atmospheric transmittance seen in Figure 5.5 suggests why Eso et al. may have shifted all the way into the IR portion of the spectrum (at 850 nm) to augment communications. Near red visible light, attenuation from water and oxygen in the atmosphere increases, and some IR bands have significantly higher transmittance avoiding attenuation caused by water and oxygen molecules in the air.

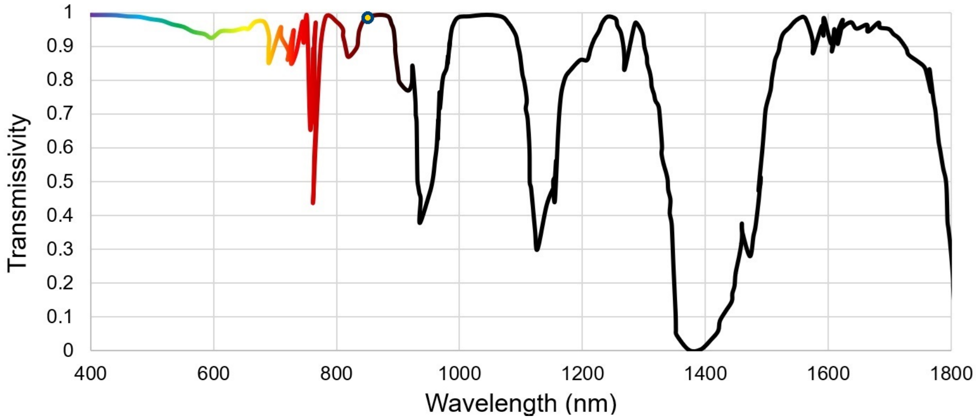

Figure 5.5. Atmospheric transmittance showing attenuation from water and oxygen molecules in the red and near-IR portions of the spectrum. The dot indicates a wavelength of 850 nm, as employed in [38]. Adapted from [139].

We tested using various wavelength off-the-shelf filters to maximize SNR for VLC in sunlight. While Forkel et al. had noted the wide pass band roll-offs of glass filters [140], we stuck with commodity glass filters designed for photography in our experiments. Commodity filters are best in keeping with the design constraints imposed reusing vehicle lights and existing sensors. Selected filters were transmissive in the near-IR, red, green, and blue wavelengths. Specific filter performance, as measured with a high-resolution spectrometer, is contained in Appendix E.

5.2.2 Polarization Filtering

Similar to filtering based on the relative spectral components of the signal and sunlight, we explored the use of polarization filters to reduce the relative strength of sunlight. Kattawar and Plass showed that Rayleigh scattering of sunlight through the atmosphere can produce polarization in the ambient scattered light [109]. While the calculations for polarization depend on the angle and the scattering medium, for clear skies maximum polarization occurs when looking horizontally with the sun directly overhead. Polarization from scattering is maximized perpendicular to the direction of propagation of the transverse wave. This fits the mid-day V2V VLC use case, and implies a polarization filter may help separate the transmitted signal from scattered sunlight. However, this is dependent on any polarization characteristics of the transmitter (we will assume the transmitted signal is unpolarized) and variation in sun angle through the day could degrade any polarization gain. Analytically, we can assess the possible gains by leveraging Malus' Law [141]

$$I_{Tx} = I_{inc} \cos^2 \theta \tag{5.10}$$

where the transmitted intensity from the filter, I_{Tx}, is the incident intensity, I_{inc}, scaled by the cosine squared of the angle, θ, between the polarizer and the polarization of the incident light. In the completely unpolarized case, there is a uniform distribution of polarization angles in the incident light and we expect a net transmission with 50% of the arriving intensity. With an appropriate selection of θ, the polarized light can be dramatically suppressed within the limitations of the physical polarizing device. Thus for the LOS path in daylight, this approach offers significant potential for suppressing solar irradiance compared to the signal. Viewing fixed targets through water, polarization filtering drastically increases contrast ratio [142], and our own experimentation with the polarization of light for VLC in sunlight demonstrated promising results with a very low power transmitter at ranges up to 550 m [75].

5.2.3 Spectral and Polarization Filter Performance

The optimal SNR received at 130 m with red, green, blue, and polarized filters is compared to the unfiltered collection in Figure 5.6. Tests were conducted near solar noon (sun direction 146-227°), on a mostly sunny day with an ambient temperature of 16° C and visibility of 15 km. Ambient brightness in the direction of the transmitter measured 70 000 lx. Across the board, all filters improved SNR. The green provided an increase in SNR of about twice as many decibels as that of the other visible color filters. Some of this observed improvement is a result of signal attenuation. All three of the colored filters reduced the overall energy reaching the CMOS sensor, providing an opportunity for higher granularity in between dark and the brightest areas of the scene during quantization.

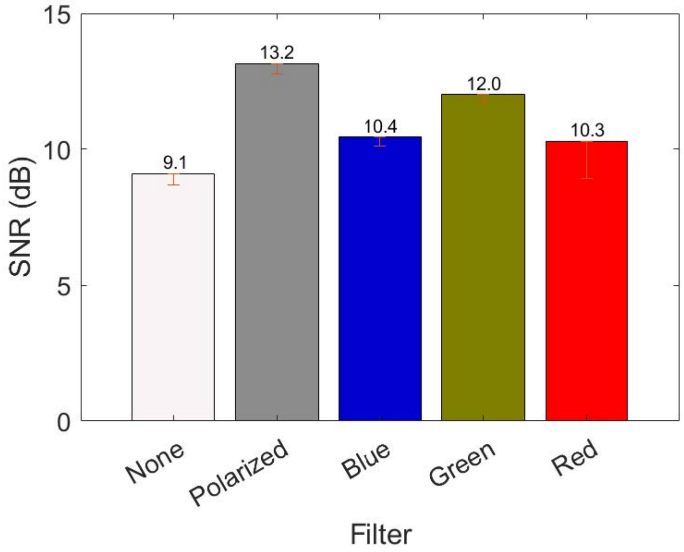

Figure 5.6. Comparison of various filters at 130 m showing the average SNR with optimal pixel selection, with 13 or move videos used for each filter configuration. Error bars show the standard deviation in average SNR as the included region of interest varied from 1 pixel to 100 pixels, as shown in Figure 5.7.

More remarkably, we found polarization filtering offers a gain of over four decibels compared to an unfiltered configuration. This is a substantial improvement, more than doubling SNR. The result is so powerful that low-powered sources can be used to transmit data embedded in polarization at long ranges. A 26 cd transmitter, less than 0.1% of typical car headlight output, was able to maintain 10 dB of SNR for communication at over half a kilometer [75].

Interestingly, as the region of interest that we included to extract signal increases, performance with a red filter falls off dramatically, actually performing worse than no filter at all. This effect can be seen in as seen in Figure 5.7. The red filter is very good at rejecting blue sky background noise and tends to aggressively flatten all values. As the signal is averaged with more and more near zeros, it too flattens out.

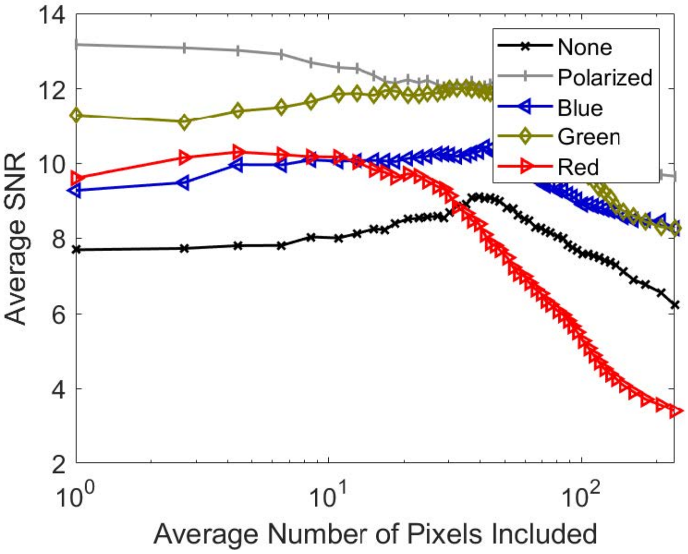

Figure 5.7. Comparison of the average SNR over 13 or more trials using various filters and camera phone with no filter at 130 m while increasing the number of pixels in the region of interest.

Many artificial lights produce a significant amount of waste heat and the atmospheric transmissivity of the near-IR is better than that of visible red light (recalling Figure 5.5). With this in mind, and the inclusion of IR for vehicular communications in [38], near-IR is directly compared to unfiltered reception in Figure 5.8. Near-IR testing was conducted slightly earlier in the day (sun direction 100-121°), with an outside temperature of 17° C, and visibility of 13 km. Ambient brightness in the direction of the transmitter was 31 000 lx.

The near-IR filter lets through so little light in the visible spectrum that it appears almost black. However, viewing the headlight through the camera, the point of light could be clearly discerned. Ultimately — similar to the red filter but more pronounced — the near-IR filter so aggressively filtered light that SNR performance decreased in all cases.

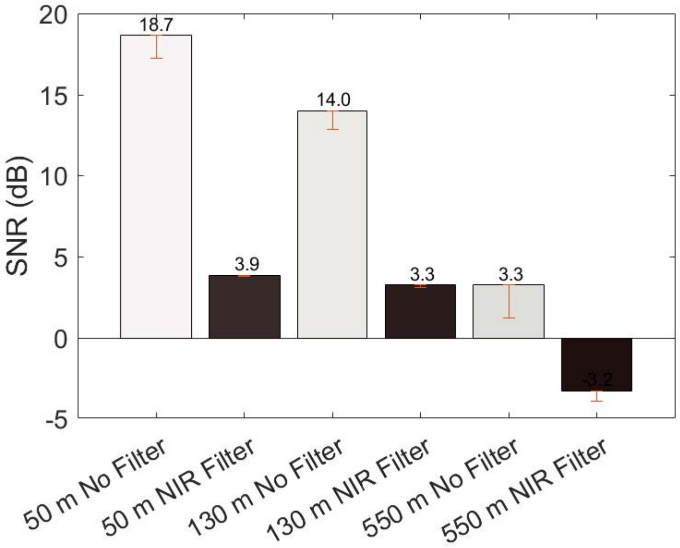

Figure 5.8. Performance of a near-IR filter vs no filtering at varying distances.

In summary, the most effective filter was the polarization filter. The flat response across the entire spectrum of the transmitter maximizes signal dynamic range, with attenuation per Malus' law before quantization. The polarization filter also helps suppress glare and noise. The glare from the headlight housing alone in Figure 4.9 is significantly attenuated by the polarizer. This improves SNR both by increasing the intensity delta when the headlight is modulated on and off and by bound quantization noise. In vehicular applications, the application of polarization filters would allow the reuse of cameras with full-color imagery, and even help to increase the contrast ratio of the software or operator also using the video feed.

5.3 Optics and Multi-Camera Configuration Gains

5.3.1 Magnification

As laid out in Section 5.1.1, having a reasonable-sized area of pixels to maintain continuous signal tracking is important, and a larger area can help reduce noise. As we move to greater distances, pixel fill continues to diminish. At 550 m, a pixel edge covers 14.3 cm of the scene while our headlight is only 8 cm tall, so the headlight already fills less than one pixel. At 1650 m, 43.5 cm of scene area is included along a pixel edge and the area of our headlight fills approximately 3% of a pixel by area. As a means to increase pixel fill, optical magnification can be employed.

Working with a relatively compact monoscope, 20× optical magnification was employed with the Pixel 6a recording video at 2× magnification as without the monoscope. The camera and camera with monoscope can be seen in Figure 5.9. Collection was conducted near solar noon (sun direction 160°) on a clear, breezy day across Monterey Bay. The ambient temperature was 20° C with a visibility of 16 km. Ambient brightness in the direction of the transmitter was 54 000 lx. Figure 5.10 shows the view from the transmitting headlight toward the wharf and from the wharf toward the headlight.

Figure 5.9. Receivers for the 1650 m experiments, with the Pixel 6a mounted to a 20× monoscope in the foreground and a Pixel 6a with no additional magnification (as used in all other experiments) in the back.

(a) (b)

Figure 5.10. Channel for 1650 m experiments; (a) the view from the transmitting headlight on the roof toward the wharf and (b) the view from the receiving phones toward the headlight.

Figure 5.11 offers a comparison of received SNR at 1650 m with and without magnification. Regardless of spectral filters employed, meaningful communication could not be achieved with our hardware without magnification. Using magnification, SNRs above 10 dB were easily achieved, allowing communication at 1650 m.

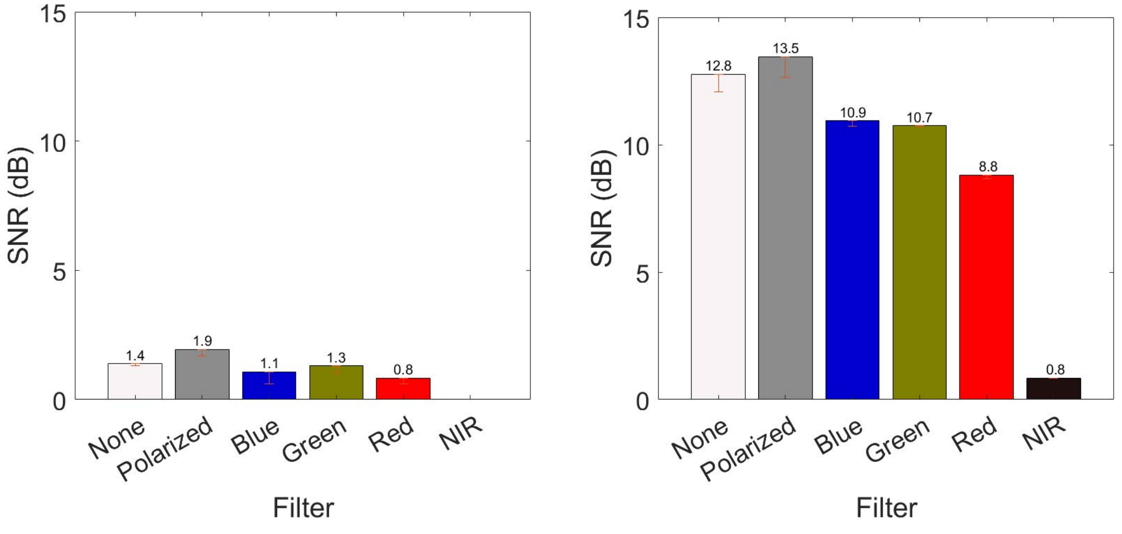

(a) (b)

Figure 5.11. Receiver performance of the Pixel 6a camera phone with various filters at 1650 m, shown no magnification in (a) and with optical magnification in (b). Without magnification, the SNR is too low to recover the signal, but magnification restores a viable SNR for communication.

With magnification, most of our findings from shorter distances hold, but there is less power in the radiant wavefront. As at closer ranges, ROI remains important as including too many pixels incorporates excess noise causing SNR to fall off dramatically. Contrasting what occurred at shorter distances, attenuation from the color filters is no longer helping to increase quantizer resolution. The signal at longer distances is weaker, and attenuation causes a net loss of SNR. Nonetheless, the polarization filter persists in enhancing SNR, even at long distances.

5.3.2 Multi-camera Techniques

Using multiple cameras provides a means to incorporate more pixels for processing. Having examined spatial diversity and array gain from the two million photodiodes of a single high-definition image on a commodity CMOS chip in Section 5.1, we now investigate using wholly separate cameras to further increase diversity and assess the impacts of greater separation with multiple imaging sensors. From [99], the coherence distance for atmospheric turbulence at visible wavelengths is 2-15 cm and we assume that for a single transmitter turbulence and beam wander will be very highly correlated. Attempting to create relevant separation distance while retaining a plausible camera separation for vehicular implementation, a multi-camera mount was fabricated with a separation distance of 13.5 cm. While not as far apart as headlights, nor quite fully 15 cm, it is in line with sensors seen on cars such as the Subaru Outback and Mercedes EQE 350 seen in Figure 5.12.

(a) (b)

Figure 5.12. Forward looking multi-camera configurations for lane departure flanking the rearview mirror at the top of the windshield as marked with arrows on (a) a Mercedes EQE 350 and (b) a Subaru Outback.

Using two separate cameras, the internal camera noise at any given pixel should be uncorrelated, and any slight variations in atmospheric noise and scintillation along the different paths could be leveraged to help suppress noise. The anticipated effect of averaging the multiple copies of the signal and multiple instances of uncorrelated noise is shown in Figure 5.13. The relative amplitude of the noise is reduced while the signal remains fairly consistent.

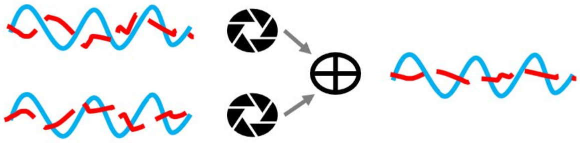

Figure 5.13. Combing two correlated signals corrupted by independent noise, signal shape is preserved while noise is suppressed, as was derived in Section 5.1.1. Using two physically separate cameras we attempt to further decorrelate noise using independent different sensor electronics and greater spatial separation.

The two cameras viewing the headlight at 130m are shown in Figure 5.14. In order to combine the signals from the two cameras, we have to conduct the signal localization process in both time and space for both cameras individually. It may be possible to engineer a fielded system to synchronize the clocks on cameras and avoid this complication, but when recording with two separate smartphones the sample windows on each device were not aligned. After localizing the preamble in time and space for each individual camera video, as laid out in Section 4.4, the start of the bit streams were aligned and weighted combinations assessed.

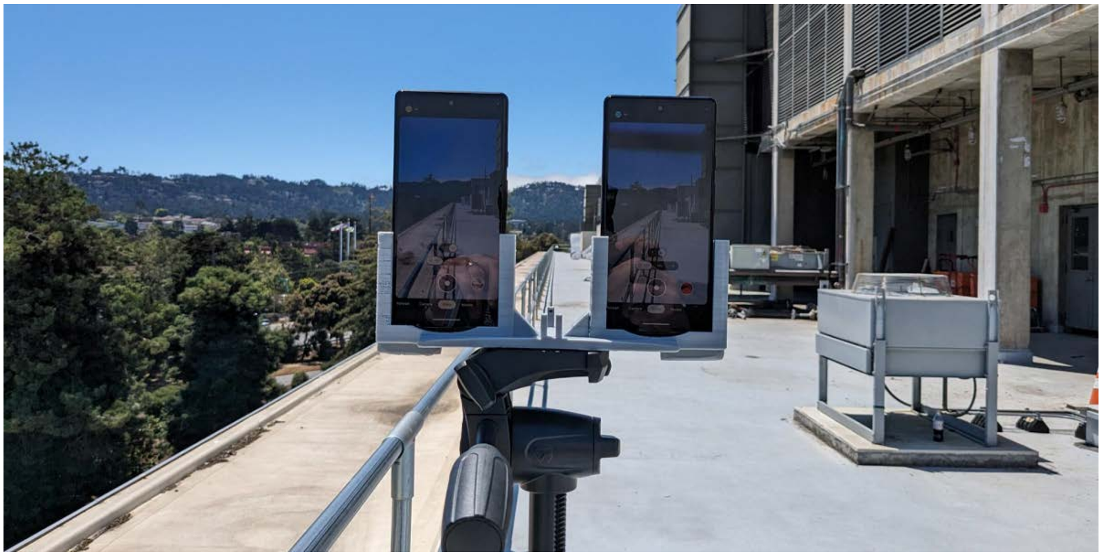

Figure 5.14. Dual camera collection at 130 m. The headlight is visible in the distance, centered between the two cameras.

Two methods of combining the signals were assessed, with results at 130 m and 550 m shown in Figure 5.15. In the first method, assuming equal weights for each video stream, an equal number of pixels are selected from the left video and the right video. In the second method, by keeping track of the relative preamble correlation strength, pixels from both of the videos were selected based on the strongest correlation to the preamble regardless of the source camera. Selecting pixels with the highest correlation regardless of source generated the best SNR with the fewest pixels.

At short ranges, the first method performed worse than using the better of the two cameras alone. At 550 m, however, while using both performed slightly worse than the better single camera, it still performed far better than the weaker of the two cameras. Since a preamble is available, using it to weight pixel selection provides SNR gain in all cases, and if weighting cannot be practically implemented selecting the camera with the superior BER outperforms the equal weight mixing of the first method.

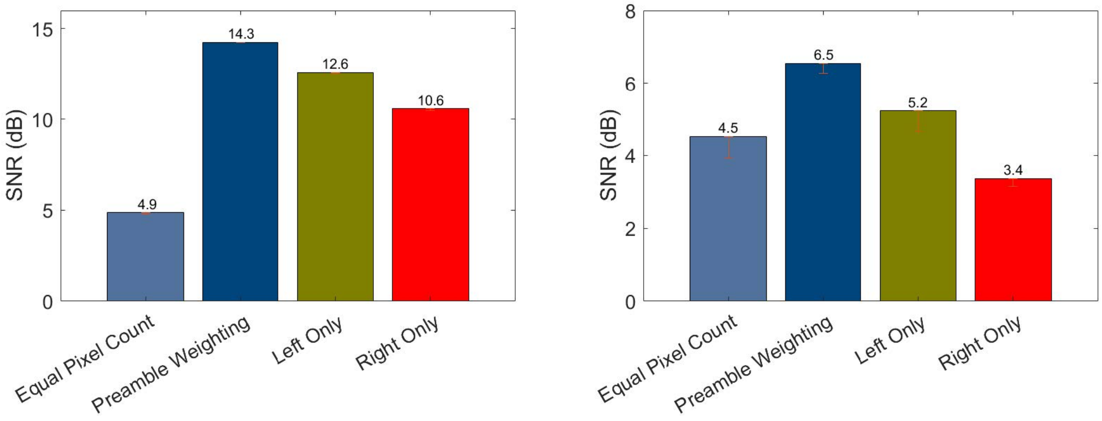

(a) (b)

Figure 5.15. Comparison of the performance of individual cameras, an equally weighted combination of the cameras, and a weighted combination based on header strength (a) at 130 m and (b) at 550 m.

5.4 Temporal Averaging

Having looked at opportunities to increase SNR through spectral and polarization filtering, as well as pixel fill and area averaging, a final dimension worth exploring is bit duration. Similar to averaging over multiple pixels to suppress random noise, longer integration times bias toward constant signal power over time while uncorrelated noise transients contribute less to the aggregate over time. Short bit durations are preferred allowing more data to be sent in less time. When we shorten bit durations too much, however, we reach a fundamental limit of how fast the receiver can sample before parts of the message are lost. The majority of our tests have been conducted with a symbol duration of 30 ms. This is close to the edge of human flicker perception but runs of ones and zeros can still lead to perceptible flicker. Seeking to mitigate this we would prefer to transmit faster and potentially even include entropy encoding to more evenly mix ones and zeros minimizing any long runs. Alternately, we could shift to a different modulation scheme such as undersampled frequency on-off keying (USFOOK) while still capitalizing on the SNR improvements in the preceding sections. In USFOOK, a frequency shift keying (FSK) modulation well beyond human visual perception is used that leverages aliasing effects to recover data [143].[5]

Another round of collection was conducted with no optical filters and a single camera to validate the effects of decreasing symbol duration. Tests were again conducted on the roof of the engineering building and near solar noon (sun direction 176°) with a visibility of 13 km. Ambient brightness measured 40 000 lx with an ambient temperature of 20° C. With a symbol period of 30 ms, the Pixel 6a camera recorded 7.2 frames of video per symbol. At this rate the middle five samples of any bit period could be averaged together, suppressing any high-frequency noise and avoiding any transients or timing errors due to the mismatch between the transmitter and receiver clocks. Similarly, with a 13 ms symbol duration, the Pixel 6a collected 3.12 frames per bit, allowing at least two data points to be averaged to establish the value of a received bit and avoiding any symbol edge issues. Continuing to reduce bit duration at 8 ms, 1.92 frames were collected per bit, and at 4 ms, 0.96 frames were collected per bit. Once the bit duration is less than a frame, there will always be bleed over from adjacent bits. Even with a perfect 1-bit per sample ratio, if the camera sampling clock is not perfectly aligned with the transmit clock, bits will be spread across multiple bins. In

---

[5] See Appendix F for a more thorough development of USFOOK.

the worst case, this would blur a repeating 01010101 string into an essentially constant 1/2 unable to be decoded by the receiver.

Synchronization is a significant challenge, and the use of orthogonal symbol patterns significantly aids bit recovery in OCC [144]. Beyond leveraging orthogonal signals, a multi-receiver setup, similar to Section 5.3.2, with purposefully staggered clocks can aid in symbol recovery. Space-time equalization has been shown to mitigate channel uncertainties [145]. Likewise, the use of multiple transmitters and receivers to aid with clock synchronization issues has been demonstrated for frequency aliasing modulation schemes [143].

The results of varying modulation speed are shown in Figure 5.16. Even a 13 ms bit duration is surprisingly robust at 130 m. A 1% BER can be compensated for with forward error correction coding. BER at less than 2 frames per bit is somewhat less encouraging, but with heavy coding, data could still be recovered at 4 ms per symbol. However, the throughput trade-off of longer symbol durations versus heavier coding tends to favor using 13 ms symbols. Reed-Solomon codes, ubiquitously used for data storage and communication, can correct errors in up to $(n - k)/2$ bits, where n is the length of the overall transmitted block and k is the length of the message bits in that block [146]. We therefore see that for every bit error we need to correct, we need to add at least two bits to the overall block. Correcting error rates of up to 30% at 8 ms would require making the block at least 60% longer, at which point the throughput is only equal to what was already achieved with 13 ms pulses.

At the same time, all of these measurements are based on the Pixel 6a slow motion recording setting at 240 FPS. If limited to a camera at 120 FPS, best-case results are more in line with the 13 ms case, and if the recording was limited to 60 or even 30 FPS with similar 30 ms symbols, the BERs in the 8 ms and 4 ms cases are illustrative. Of course, longer symbols could be used with slower cameras — restoring SNR and BER — but this would tend to introduce visible flicker unless an alternate modulation scheme or domain were employed [75]. With a commodity CMOS sensor capturing 240 FPS, a symbol duration of 13 ms — a little less than half the 30 ms symbol period used in the previous sections — provided improved throughput and reduced flicker, with a manageable BER at 130 m.

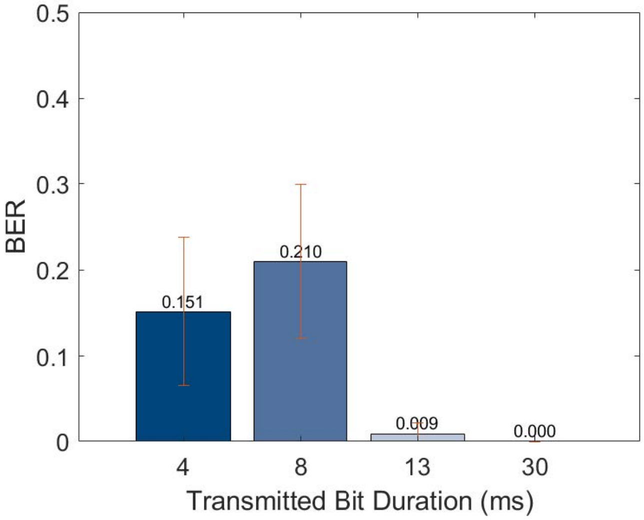

Figure 5.16. BER measured at 130 m with transmitted bit durations of 4, 8, 13, and 30 ms collected at 240 FPS.

Throughout this chapter, we have tested and demonstrated numerous means to improve SNR in outdoor VLC systems. Using spatial selection to incorporate only pixels containing signal provides essential noise rejection. Using a digital filter tuned to the fundamental frequency of the signal preamble allows spatial selection of elements in the sensor array. Leveraging color filters, wavelength variation between signal and background spectra has little effect when data is analyzed only after demosaicing and compression. However, the attenuation introduced by these color filters reduces quantization noise and highlights the contribution of varying sub-pixel numbers in the CFA. Polarization filtering effectively separates characteristics of the light from the signal and background, providing both attenuation and selective gain at the receiver. Multicamera configurations increase the overall effective aperture size, but using optics to spread the signal over more pixels on one CMOS chip proves more effective, especially at longer ranges. Both polarization filter and optical magnification provide significant improvements enhancing SNR for outdoor VLC.

CHAPTER 6:
Analysis of Key Parameters for Commodity Cameras

Bringing together the pieces covered in Chapters 2 through 5, we analytically describe SNR for VVLC using existing vehicle lights and low-cost CMOS receivers. This chapter provides a systematic analysis of the components impacting SNR. We begin by assessing the terms which contribute to received signal power and then explore the contributing sources of noise. The relative strength of the terms allows for simplification in modeling when some terms, such as internal camera noise, are drastically smaller than more dominant terms, such as quantization noise. Experimental results and observations from Chapter 5 illustrate the margins around calculations and validate opportunities for simplification. Ultimately, received SNR is just signal power received divided by noise power, so we begin by expanding received signal strength and subsequently assess the noise.

6.1 Received Power

We begin analyzing SNR by quantifying the received signal power, the portion of the transmitted power reaching the receiver. Figure 3.1 in Chapter 3, illustrates signal degrading effects including spreading loss, absorption, and diffusion. The Friis equation, in decibel form, provides an easy way to see the components that sum to produce the overall received power

$$P_{Rx} = P_{Tx} + G_t - L_{fs} - L_{abs} + G_r \tag{6.1}$$

where P_{Tx} is the transmitted power, G_t and G_r are the gain provided by apertures, optics, and amplification in the transmitter and receiver respectively, L_{fs} is the free space spreading loss, and L_{abs} is the absorption loss [147]. Other loss terms can be included if they are significant in attenuating the signal. In particular, we will consider the pixel fill factor as an additional loss factor. Converting Equation 6.1 from additive terms in decibels to linear multiplicative factors and consolidating all the gain terms into a single variable, G, we obtain

$$
\begin{aligned}
P_{Rx} = {} & P_{Tx} \times L_{fs} \times L_{abs} \times L_{fill} \times G \\
= {} & \begin{cases} P_{Tx} \times \frac{1}{r^2} \times e^{-\beta r} \times \frac{A_{Tx} \times W_{\mathcal{P}}^2}{r^2 \sin^2(\theta)} \times G & \text{for } Px_{fill} < 1 \\ P_{Tx} \times \frac{1}{r^2} \times e^{-\beta r} \times 1 \times G & \text{for } Px_{fill} \geq 1 \end{cases}
\end{aligned}
\tag{6.2}
$$

where β is an atmospheric attenuation coefficient , A_{Tx} is the area of the transmitting light, $W_{\mathcal{P}}$ is the pixel count across the sensor frame, and θ is the angle of view of the sensor. The L_{fill} term, assuming that pixel fill is less than 1, dilutes received signal strength as a ratio of the area on the pixel filled by the transmitter over the total area seen by the pixel. The use of magnification to improve pixel fill is captured in the θ term, where zooming in has the effect of narrowing the FOV and allowing the transmitter to fill a greater portion of the pixel.

6.1.1 Transmitter Power

Using vehicle lights, maximum transmit power will have a fixed value, based on vehicle regulations and eye safety constraints. Federal Motor Vehicle Safety Standard 108 defines the maximum intensity for each type of vehicle light fixture and the allowed variation in illuminance across the beam pattern [148]. Since this is a defined standard and we cannot increase transmit power to achieve greater range, we will consider transmit power, P_{Tx}, as a constant.

6.1.2 Path Loss

Two primary factors cause received power to decrease with increasing distance between the transmitter and receiver: spreading, as discussed in Section 3.1.1, and particle interactions, as discussed in Section 3.1.1. Of the two, atmospheric attenuation causes some signal loss but is significantly less than inverse-square losses. Typically, the attenuation coefficient, β, is between 0.0001 m^{-1} for clear air up to 0.002 m^{-1} for dense fog [91]). At a distance of 1 km in clear air, the atmospheric attenuation reduces the signal by approximating 9.5%. Over 90% of the original signal strength remains after attenuation losses. Contrasting that, wavefront spreading losses — captured by the $1/r^2$ term — result in the arriving wavefront being reduced by 10^6 from the originally transmitted power. In decibel notation, attenuation losses at 1 km are approximately 0.5 dB while inverse-square losses are 60 dB. Even in dense fog, attenuation is only 8.6 dB, nowhere near the 60 dB of spreading loss. The atmospheric attenuation term can be omitted for simplification.

During the testing of near-IR filters, described in Section 5.2, a baseline of videos with no filters was captured within a short time window with constant atmospheric conditions. While the overall background scene varied moving from the rooftop tests (50 and 130 m) to the 550 m cross-campus test, all videos were recorded within an hour. The temperature change was limited to 1° C and there was no change in ambient brightness, visibility, or the cloud ceiling. Finding the inverse-square losses at each range in decibels as

$$L_{fs} = 10 \log_{10} \frac{1}{r^2}, \tag{6.3}$$

we calculate -34.0 dB at 50 m, -42.3 dB at 130 m, and -54.8 dB at 550 m. Beginning with the longer distances, observed results showed a 10.7 dB delta between 130 m and 550 m, presented in Figure 5.8. This difference is reasonably in line with the delta of 12.5 dB from the inverse-square calculation. Given that variables other than range were held constant, this affirms that r^2 losses are the dominant loss factor. However, while these losses are a limiting factor for VLC at long distances, we must provide two caveats. First, we are not actually measuring incident wavefront power, but only assessing SNR after quantization and compression in the sensor. We will return to quantization in Section 6.2.1. The r^2 losses interplay with quantization noise as scene brightness varies. Second, as we will next explore in Section 6.1.3, at shorter distances, other gains compensate for inverse-square losses. From Equation 6.3, we would expect a difference of 8.3 dB between 50 m and 130 m, but in Figure 5.8 we only observed an SNR delta of 4.7 dB.

6.1.3 Gain

As originally described by Friis, the gain terms we are using were the effective antenna size at the transmitter and receiver [147]. The metric we are primarily working with for VLC using commodity CMOS sensors is the number of pixels, or portion of a pixel, filled with the signal. When multiple pixels are filled, an SNR gain is achieved. While this is an interplay of sensor noise and signal power, following the RF convention, we describe it here as a component of received signal power. In order to increase this gain by filling more pixels, we employed optics at 1650 m to increase the physical aperture size, in line with Friis's initial note. Likewise, the sine term in Equation 6.2 is a measure of size within the aperture of an individual photo site. Calculation of SNR gain is presented in Section 5.1.1.

In experimentation, increasing the distance between the headlight and camera from 50 m to 130 m while holding all other variables constant reduced SNR by 4.7 dB. Using Equation 6.3 we calculated an expected difference of 8.3 dB from inverse-square losses alone. Multi-pixel gain explains how the received SNR is more than double what spreading loss would suggest. Using the FOV geometry laid out in Section 4.3.1, we can approximate that 31 pixels are filled by the headlight signal at 50 m, while at 130 m only 5 pixels contain signal. Equation 5.8 provides that gain can be up to the number of elements included. At 130 m, 5 pixels m could produce up to $10 \log_{10}(5) = 7$ dB of gain, and the 31 pixels at 50 m could provide up to 14.9 dB of gain. With ideal, n times, gain moving closer from 130 m to 50 m could provide 6.2× gain, or 7.9 dB. We observed 3.6 dB of gain after accounting for the inverse-square losses between the two distances. This is 2.3× gain reflects an effective gain of $0.37n$.

Adding more pixels at a fixed distance does not produce the same gains as managing pixels in the FOV at increasing distance. With the same 130 m geometry and scene on a slightly brighter day (ambient brightness of 70 000 lx vs 31 0000 above) the effect of including more pixels was shown in Figure 5.2. In these conditions, the SNR at the single best pixel in the recording was 7.8 dB. As the pixel inclusion area expanded to approximately 40 pixels, SNR increased to 9.0 dB. This total gain of 1.2 dB, approximately 1.3×, adding nearly 40 pixels, would reflect an effective gain an order of magnitude less at only $0.03n$. However, as we saw above, the headlight only fills 5 pixels at 130 m. The SNR gain in this case has less to do with gain and more to do with ensuring that all the signal-containing pixels and any halo are fully within the region of interest throughout the collection as camera movement and mirage effects slightly shift the image in the scene. Including more pixels that rarely contain signal adds robustness, seen in the 1.3× gain, but does not continue to contribute linearly to gain as the signal power summations used in Equations 5.6 through 5.8 begin to include signal pixels at or near zero. Taken too far, including an excessive amount of pixels with no signal begins to rapidly attenuate SNR, as is seen in the exponential drop in SNR in Figure 6.1 beyond an inclusion area of 60 pixels.

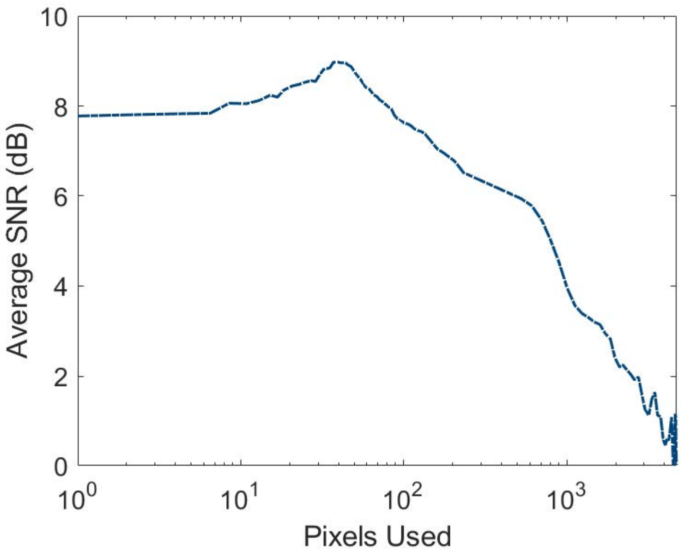

Figure 6.1. Combining both curves of Figure 5.2, with average SNR over 13 trials, illustrates the robustness gain including additional pixels at fixed range. With just headlight pixels, average SNR across all trials is constant. Increasing the size of the region of interest to capture the corona around the light and compensate for movement in the frame increases robustness, adding 1.3 dB of SNR. However, including pixels that never contain signal causes an exponential drop off in SNR.

At long distances, we see that a multi-pixel array is critical to achieving sufficient SNR for communication. Again applying the FOV calculations, with the native 2× optical zoom of the camera phone alone, the signal should fill 0.028 pixels at 1650 m. In experimentation, as seen in Section 5.3.1, we calculated SNR of 1.4 dB at 1650 m. This would indicate the received signal is 1.4 times stronger than the noise, but our method of calculating SNR, in Section 4.5, assumed that the signal was stronger than the noise to separate high and low bits. The accuracy of our SNR calculations with such low margins is not reliable. Even assuming a true SNR of 1.4 dB, it would be infeasible to transmit data with a reasonable BER at symbol durations supporting VVLC.

Cascading the monoscope and 2× zoom in the phone at 1650 m increased the number of pixels used on the sensor and provided substantial SNR gain. We observed a 7-pixel diameter area saturating the quantizer with signal. The actual crescent shape of the headlight reflector area was not discernible, but the saturation area presented clean signal modulation. At a full n times gain, 38 pixels would provide 15.8 dB of array gain. Experimentally, we saw an increase in received SNR of 11.4 dB, to a total received SNR of 12.8 dB. An 11.4 dB, 13.8×, gain over 38 pixels indicates an effective gain of $0.36n$, which is almost exactly the same result as with the change in pixel fill from 130 m to 50 m.

Summarizing our gain finds, including additional signal pixels at moderate to long ranges provided gain of approximately $0.36n$. Including additional pixels immediately around the signal pixels provides robustness to movement, without large gain or significant SNR attenuation.

6.2 Noise Powers

This section examines the noise portion of SNR in outdoor VLC using commodity hardware. Total noise power can be expressed as a summation of the contributing components,

$$P_N = P_Q + P_{amb} + P_{cam} \tag{6.4}$$

where P_Q is quantization and compression noise, P_{amb} is ambient environmental noise due to hardware jostling, atmospheric turbulence, and interfering light, and P_{cam} is the result of all terms contributing to the sensor noise figure including thermal and shot noise. We proceed analyzing and comparing these components of noise, showing empirical results and noise mitigation techniques as they apply.

6.2.1 Quantization Noise

Using any system that digitizes data, quantization limits the granularity of outputs. Using commodity imaging hardware and software, 8 bits per channel per pixel is most common. This granularity provides videos and images that appear natural to human perception. The 256 possible red, green, and blue values combine to offer over 16.7 million colors. Impressive as this number is, 256 levels is still a finite number, and relatively small compared to the dynamic range of many signals of interest. 8-bit audio recordings do not sound natural. Depending on the dynamic range of illumination in a scene, 8-bits can be a significant limitation on recording illuminance values. In some of our tests, we saw background luminance of 70 000 lx. With 256 levels — provided by 8 bits of resolution — each digital output value represents a 8750 lx step. In many settings, a single 8750 lx single step is well beyond the total dynamic range of the scene. The minimum required illumination for an office, established by the Occupational Health and Safety Administration, is only 300 lx [149]. Both human vision and digital cameras adapt to account for such large ranges, enhancing sensitivity for dim objects in low light conditions and adjusting to expanding dynamic range in bright environments at the expense of subtle details in dark areas.

Our initial analysis of quantization noise in Section 3.1.2 focused on rounding errors in the process of digitizing continuous values. Beyond rounding producing quantization noise based on step size, we now account for the fact that the peak quantization value may be a result of the intensity of either the scene or the signal. To accommodate the full dynamic range of the scene, quantization noise power, P_Q is

$$P_Q = \frac{\max(P_{amb}, P_{Rx})}{3 \times 2^{2b}} \tag{6.5}$$

where the upper quantization value — previously just the peak value of the value of the signal squared — is now based on the greatest average brightness in the camera FOV. This maximum brightness is not necessarily the brightness of the received signal. If the signal is the brightest set of pixels, it drives the upper limit of the quantizer, and the maximum SQNR with 8 bits at 6 dB per bit in a uniform quantizer is 48 dB. However, if the scene is brighter than the received transmission, the top quantization value is based on scene brightness, not P_{Rx}. This effectively reduces SQNR

$$\text{SQNR}_{signal} = P_{Rx} \times \left(\frac{3 \times 2^{2b}}{P_{amb}}\right) = \text{SQNR}_{cam} \times \left(\frac{P_{Rx}}{P_{amb}}\right) \tag{6.6}$$

where SQNR_{cam} is the SQNR the camera would have for the whole scene.

If the signal dynamic range is half of the scene dynamic range, only half the quantization bins are used. In an 8-bit quantizer with 256 possible levels, the signal only modulates across 128 levels. Effectively, the signal only has access to 7 bits of output resolution. Using the 6 dB per approximation, the best possible SQNR is now limited to 42 dB, down from 48 dB, due to a brighter background expanding quantization bin size and reducing resolution. This is one of the most significant challenges for outdoor VLC with commodity hardware. Modern CMOS sensors can detect low numbers of photons, but the only way to produce images with bright areas is to expand the upper quantization threshold, thus reducing the granularity of each digital increment. Daylight is a challenge not due to large random variations in noise power, but because the background is producing a large DC offset reducing the output resolution of the sensor.

The data collection presented in Chapter 5 includes empirical measurements that vary only in background illuminance, as shown in Figures 5.6 and 5.8. In both data sets, videos were collected at 130 m without optical filters with the same background and geometry on different days. On the brighter day, shown in Figure 5.6, we observed 9.1 dB SNR at 70 000 lx of background luminance. On a partly cloudy day with 31 000 lx of background luminance, seen in Figure 5.8, we observed an average of 14.0 dB SNR. Comparing these data points cases with Equation 6.6, the power received term is constant (the same headlight at the same range) leaving the change in SQNR simply as a ratio of the two luminance values. The background intensity on the brighter day was 2.3× higher than the second day. Simply using this ratio in decibel units, we anticipate a 3.5 dB SNR delta based on increased quantization noise. Our average measurements showed a 4.9 dB SNR delta between the videos. The 1.4 dB difference between theoretical and measured values is both small and within the standard deviation error bars seen in Figures 5.6 and 5.8. Quantization noise driven by increasing step size in scenes with bright backgrounds is a dominant noise source, causing signal loss as a proportion of the signal-to-background brightness ratio.

Attenuation Gain

In light of the negative effects of increasing bright background on quantization resolution, attenuation can also be used to compress quantization bin sizes and reduce quantization noise in some cases. When the signal is significantly brighter than the background, signal pixels are driven into saturation. For VVLC, the signal is constrained to a small portion of the CMOS sensor — less than 40 pixels out of 2 million pixels in all of our tests — and the signal intensity does not dominate the overall average brightness across the sensor. Beyond only filling 0.002% of the sensor array, the signal is modulating, so its average intensity over time is less than its peak value. The upper quantization bound set by the camera is based on peak average brightness, not these very few points of bright points. As such, when the signal intensity exceeds the upper quantization threshold, the quantization process simply truncates it to the maximum value of the scene — 255 for an 8-bit quantizer. Using attenuation dims the scene, reducing both signal and noise. By itself, this does not improve SNR since both signal and noise are reduced in the same amount. However, the interaction of very bright signal pixels with the quantizer is nonlinear. If attenuation draws the peak signal intensity closer to the upper quantization bound, all the signal energy that was lost truncating to the upper bound can be incorporated into the ratio. Attenuation makes the background darker suppressing noise, while attenuating the signal increases its dynamic range on the quantizer, improving SQNR.

Attenuation improved SNR in our tests with various optical filters. Repeated tests at 130 m using color filters attenuating the signal reduced quantization noise. Transmissivities of these filters are provided in Table E.1 in Appendix E. During 130 m tests conducted at the same time, with the same atmospheric conditions and scene geometry, the green filter increased the average received SNR by 2.9 dB compared to the unfiltered case. The blue and red filters increased SNR by 1.3 dB and 1.2 dB respectively. Moderate attenuation resulted in greater SNR, as seen in Figure 5.6. The signal had greater dynamic range leveraging more quantization values.

This effect relies on moderate attenuation, reducing truncation when the signal overshoots the maximum quantization value. Attenuation does not always help. Tests at 1650 m showed that just suppressing the received signal and noise is not always beneficial. Contrasting the gain produced by the color filter attenuation at 130 m, in Figure 5.6, at 1650 m the attenuation caused by the colored filters resulted in a net loss of SNR in all cases at 1650 m, seen in Figure 5.11(b). Even at short distances, aggressive attenuation like the near-IR filter, drastically reduced SNR.

6.2.2 Ambient Noise and Wander

Ambient noise can result from both movement and other lights in the scene. Pixel movement in the frame is a significant challenge for outdoor VLC with commodity CMOS sensors. While there may be other transmitters and interfering light sources in the environment, the selection of pixels from a CMOS array can reject this noise given sufficient spacing in the FOV. Ambient noise is predominantly driven by wander, not other interfering sources.

Even in cases where other noises appear in the same pixels filled with signal, the competing light has limited impact. The clear plastic of the headlight housing produced glare throughout our experimentation. However, the glare does not have any significant frequency content and only injects a DC bias. Using VVLC on the road with multiple cars sending data, it is possible that the signal from another car could reflect off the housing of the signal light of interest. However, vehicle lights are regulated and standardized, so the reflected signal would be far less than the signal of interest. The scattering as the interfering reflected from the housing of the signal of interest reduces its intensity, and the additional path length for the interfering light causes r^2 losses far beyond the spreading loss for the signal of interest. Combined, these effects mean the direct signal will be much stronger than any reflected interference.

Movement of vehicle and turbulence will introduce most ambient noise. Atmospheric turbulence will cause the signal to wander. Most studies of beam wander are based on laser propagation with coherent sources, but they provide a model to extend to incoherent light from headlights in VVLC. A study of beam wander measurements over a horizontal path throughout a day in Tokyo found that, at around 500 m, beam wander was typically found near 5 mm, and near 1.5 km beam wander averaged around 1.5 cm but was sometimes up to 3 cm [150]. The LED headlight is an incoherent source and the beam wander effect will not be as pronounced as it is for specific laser light frequencies. Beam wander, σ_x is given by

$$\sigma_x = 3.14 C_n r^{17/12} \tag{6.7}$$

where C_n is the structure constant derived from the temperature difference between points and r is the path length in meters [150].

With our specific experimental design, as described in Section 4.2, a pixel edge at 1.5 km covers 39 cm of FOV, so a 3 cm shift is fairly insignificant. Assuming reciprocity in the channel, beam wander is also equivalent to pixel areas shifting around in the FOV. Accounting for the ambient noise that is incorporated through this process, we present a simplified model of the FOV and energy received at any pixel in Figure 6.2. The photons arriving at the sensor, or equivalently any photosite, can be approximated as a summation of the intensity of photons from the background, the transmitter, and ambient scattering in the atmosphere:

$$I_{px} = I_{amb} + I_{Tx} + I_N \tag{6.8}$$

where I denotes the cumulative intensity as the summation of components. The approximation is validated by its reciprocity with the Phong model of illumination, where net intensity on screen is

$$I_{px} = I_{amb} + I_{diff} + I_{spec} \tag{6.9}$$

where I_{diff} and I_{spec} represent the diffuse and specular reflections from objects [151], [152]. For our purposes, the individual intensities of the sources contributing to the overall ambient scene brightness are less relevant, but using the superposition of illumination components allows continued analysis of beam wander.

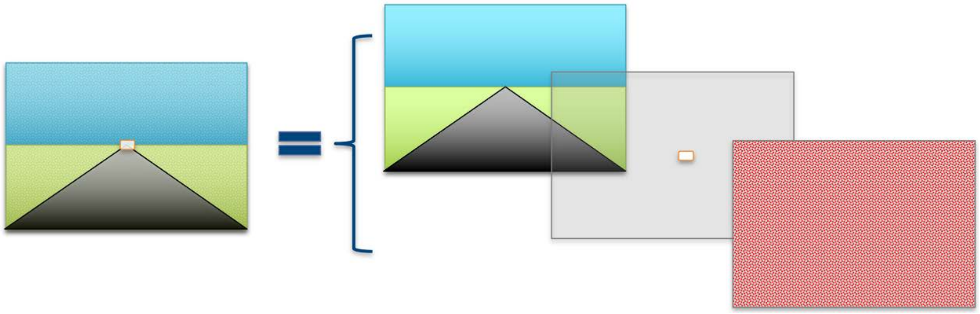

Figure 6.2. The imaged scene, or light arriving at any pixel, can be viewed as the superposition of the background scene, transmitting light, and additive noise.

Following from Equations 5.1 and 5.3, the more pixels the transmitter fills, the greater the SNR. We can assume the atmospheric noise to be relatively constant in the cone of view, but as beam wander occurs, the cumulative ambient background level will change. In Figure 6.2, we see a simplified view of a street on neutral terrain below a blue sky background. If the FOV shifts up, more sky is included in the region of interest, increasing the ambient background intensity. Likewise, shifts down or sideways will vary the ratio of dark asphalt to landscape and vary background intensity with pixel wander.

If we assume the sky has a luminance of 1, the asphalt road has an albedo of 0, and the terrain has an albedo of 0.5, we can represent the overall background luminance numerically as the sum of intensities over the proportional area. Representing this as a matrix with half-pixel shifts represented in each row and column, the intensity at each shift is

$$I_{shift} = \begin{bmatrix} 1 & 1 & 1 & 1 & 1 \\ 1 & 1 & 1 & 1 & 1 \\ \frac{3}{4} & \frac{3}{4} & \frac{5}{8} & \frac{3}{4} & \frac{3}{4} \\ \frac{1}{2} & \frac{1}{4} & \frac{1}{8} & \frac{1}{4} & \frac{1}{2} \\ \frac{1}{4} & \frac{1}{8} & 0 & \frac{1}{8} & \frac{1}{4} \end{bmatrix}, \tag{6.10}$$

where the center value represents the scene shown in Figure 6.2. Likewise, the fourth row, third column value represents the shift shown in Figure 6.3 where beam wander shifts the scene straight down one half pixel height.

In perfect stillness, the background would not vary. There would simply be a constant bias mixed with the signal in the pixel. Assuming wander causes uniform shifts within half the region of interest, background variance jumps to 0.11. This variance contributes extra noise power, reducing SNR. Full scene shifts increase background variance to 0.13, creating even stronger noise. Using the results from [150] that beam wander can approach 3 cm at 1.5 km, with our test system we only expect an 8% shift in pixel composition — nowhere near a half or full pixel — and the maximum expected variance due to atmospheric beam wander alone is 0.02. However, we empirically observed that to maximize SNR, we sometimes needed to use a region of interest 6 pixels wide to fully capture all signal energy from a transmitter nominally 2.2 pixels wide at 130 m, indicating more than full pixels shifts in either direction in some of our tests. At short ranges, the transmitter filled several pixels and shifts did not cause outages. Likewise, to achieve the required gain for communication at long distances, optics increased the number of pixels filled and small pixel shifts still did not cause outages.

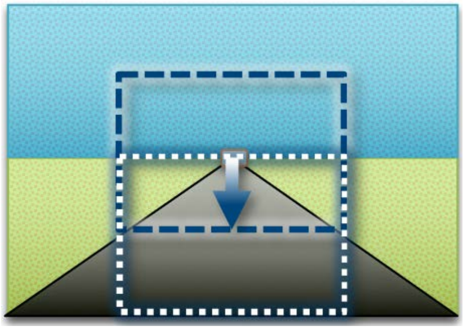

Figure 6.3. Illustration of the impact of the pixel scene area from Figure 6.2 being shifted down half a pixel, reducing the overall background albedo.

From Equation 6.7 movement increases as $r^{\frac{17}{12}}$. However, the variation in background illuminance is a function of both how much the pixel is moving and how big the pixel is. A narrow beam moving on a high contrast edge — like the horizon — would cause huge variance. However, gentle sway with a large optical aperture will cause only subtle changes in variance. Holding pixel count, $\mathcal{P}_{ct}$, and angle of view, θ, constant, in Equation 4.2 we saw FOV is proportional to $r \sin\theta$. Putting this all together, we have

$$P_{amb} = \frac{3.14 C_n r^{\frac{17}{12}} \times \mathcal{P}_{ct}}{r \sin\theta} = \frac{3.14 C_n \mathcal{P}_{ct}}{\sin\theta} r^{\frac{5}{12}} = \kappa\, r^{\frac{5}{12}} \tag{6.11}$$

where κ aggregates the fixed constants for any given setup, including the camera resolution and angle of view, as well as the atmospheric structure constant, C_n. The wander matrix in Equation 6.10 is derived from the generic, symmetric scene in Figure 6.2. In practical application, the scene could have many varied and asymmetric compositions, further increasing variance with beam wander and reducing SNR. The impact of increasing range on background jostling noise based on turbulence alone, however, increases at a rate slightly less than the square root of the distance as increasing pixel inclusion area counteracts shimmer.

As a caveat to this relatively slow increase in noise from increasing range, the matrix in Equation 6.10 assumes at most a full region of interest offset. Beyond that, the transmitter is no longer in the integration area and SNR goes to zero regardless of the denominator noise power. While turbulence is somewhat countered by increasing size, the impacts of pointing error — as may be caused by vehicle movement — become much more pronounced at longer distances. While the beam wander results derived from [150] are reassuringly small, they do not capture all the other sources of movement in the scene. Many of these sources of movement could be mitigated with optical flow tracking in software, which was not implemented in our experimental design, but would help mitigate noise power caused by background scene variation in the region of interest.

Polarization Gain

Having seen opportunities for attenuation gain in Section 6.2.1, the polarization filter performs far better than would be expected from attenuation-based SQNR improvements alone. Using a linear polarizer provides selective gain, reducing the impact of the background included in the region of interest and increasing SNR at all ranges tested. The polarizer rejects spectral reflections and atmospheric scattering in the background scene at a higher rate than it suppresses the signal, producing SNR gain. Considering the exemplar scene in Figure 6.2, polarization filtering makes the background darker while the transmitting headlight remains brighter in comparison. This directly provides SNR gain. Further, considering Figure 6.3 and the derived matrix in Equation 6.10, the brightness of the sky and reflected energy is reduced, reducing their dynamic range and, in turn, variance contributing to scene noise. Through experimentation, we found a linear polarizer provided 4.1 dB of gain at 130 m, more than doubling received SNR. At 1650 m, as other filters failed to provide benefit, the polarization filtering still provides an additional 0.7 dB of gain.

6.2.3 Internal Camera Noise

The quantum nature of light leads to noise in optical sensors and thermal noise is an important consideration for electronics in all sensitive RF and optical receivers. Used for imaging in daylight, CMOS sensors are not limited by these noises but, for completeness, we consider the noise from the receiving camera itself as:

$$\begin{aligned} P_{cam} &= \quad P_{shot} \quad + \quad P_{therm} \\ &= 2q_e G_{PD}^2 F(I_{inc})B + 4\left(\frac{k_B T_k}{R_l}\right) F_n B \end{aligned} \tag{6.12}$$

where F is the excess noise, q_e is the electron charge, G_{PD} is the photodiode gain, B is the photodiode bandwidth, I_{inc} is the induced photocurrent, k_B if the Boltzmann constant, T_k is the absolute temperature in Kelvin, R_l is the load resistance, and F_n is the noise figure [33]. Photon shot noise results from the Poisson distribution of quanta of light arriving at the sensor. Thermal noise results from the random thermal agitation of electrons in the sensor. In some precision sensors, cryogenically cooling is used to reduce this thermal noise. With the intent of reusing existing, low-cost sensors in vehicular applications, both of these terms will likely have values analogous to those seen in Table 3.2.

From Table 3.2, the voltage swing on our sensor is nearly half a volt, while noise sources produce small fractions of a mV. Summing DSNU, read noise, and dark voltage over a frame gives 0.264 mV, less than 0.06% of the sensor voltage swing. This is negligibly small, and an order of magnitude less than best-case quantization noise. Internal camera noise can be omitted from calculations for outdoor VVLC due to the abundance of photons, from both the signal and background, reducing any shot noise effects and the extraordinarily small impacts of thermal noise relative to other processing noise.

6.3 Aggregation and Simplification

Having developed each of the individual components for received SNR, from signal strength in Equation 6.1 to the contributing noise powers in Equation 6.4, we aggregate them to establish an analytical model for SNR with commodity hardware. We begin considering all relevant terms and subsequently incorporate simplifications based on the relative weight of components. Ultimately, leveraging just the most significant terms — all of which are range dependent — we arrive at a simple proportionality bound SNR performance for outdoor VLC systems using commodity hardware.

Dividing received signal strength, from Equation 6.2, by the summation of the noise powers in Equations 6.5, 6.11, and 6.12, the SNR is

$$\text{SNR} = \begin{cases} \dfrac{P_{Tx} \times \frac{1}{r^2} \times e^{-\beta r} \times \frac{A_{Tx} \times S_{res}^2}{r^2 \sin^2(\theta)} \times G}{\left(\frac{\max(P_{amb}, P_{Rx})}{3 \times 2^{2b}}\right) + \left(\kappa \; r^{\frac{5}{12}}\right) + \left(2 q_e G_{PD}^2 F(I_{inc}) B + 4 \left(\frac{k_B T_k}{R_l}\right) F_n B\right)} & \text{for } \mathcal{P}_{fill} < \; 1 \\ \dfrac{P_{Tx} \times \frac{1}{r^2} \times e^{-\beta r} \times G}{\left(\frac{\max(P_{amb}, P_{Rx})}{3 \times 2^{2b}}\right) + \left(\kappa \; r^{\frac{5}{12}}\right) + \left(2 q_e G_{PD}^2 F(I_{inc}) B + 4 \left(\frac{k_B T_k}{R_l}\right) F_n B\right)} & \text{for } \mathcal{P}_{fill} \geq \; 1 \end{cases} \tag{6.13}$$

for the cases of sub-pixel and multiple-pixel fill respectively. In practice, many of these variables will be fixed. Transmit power is regulated and most camera parameters, including pixel count and noise figure, will be fixed once implemented in a vehicle. The weather can have a substantial impact and is variable. Allowing atmospheric attenuation, β, and the structure constant, C_n, to vary can provide some insights, but as noted in Section 6.1.2, the inverse-square loss is significantly greater than atmospheric attenuation and absorption. The primary opportunities we have seen to increase throughput at long distances are filtering and magnification. Consolidating the range-dependent terms in the power received and aggregating fixed camera noise as C, Equation 6.13 is more succinctly expressed as

$$\text{SNR} = \begin{cases} \dfrac{P_{Tx} A_{Tx} S_{res}^2 G}{e^{\beta r} r^4 \sin^2(\theta) \left[\left(\frac{\max(P_{amb}, P_{Rx})}{3 \times 2^{2b}}\right) + \left(\kappa r^{\frac{5}{12}}\right) + C \right]} & \text{for } \mathcal{P}_{fill} < 1 \\ \dfrac{P_{Tx} G}{e^{\beta r} r^2 \left[\left(\frac{\max(P_{amb}, P_{Rx})}{3 \times 2^{2b}}\right) + \left(\kappa r^{\frac{5}{12}}\right) + C \right]} & \text{for } \mathcal{P}_{fill} \geq 1 \end{cases} \tag{6.14}$$

where we see changes in SNR are dominated by inverse-square losses at short ranges, but then decrease at a rate of $1/r^4$ when the transmitter fills less than one pixel. In the sub-pixel regime, magnification is critical to boosting receive SNR by reducing background noise in the integration area and including more signal. The use of multiple pixels best enables VVLC with CMOS sensors at both short ranges and long distances requiring magnifications, so we will continue to focus there.

Given typical values, inverse-square losses dominate atmospheric attenuation and quantization noise dominates both beam wander and the internal camera noise This allows further simplification of Equation 6.14. For the pixel fill greater than one to

$$\mathrm{SNR} \propto \frac{P_{Tx}G}{r^2\left(\frac{\max(P_{amb},P_{Rx})}{3\times 2^{2b}}\right)} \tag{6.15}$$

where SNR performance is approximated by omitting small terms and focusing on the dominant source of noise and gain. Both G and P_{Rx} are also themselves functions of range. Carrying forward the same simplifying approximations, the received power, P_{Rx}, is proportional to P_{Tx}/r^2. The multi-pixel gain, G, remains dependent on specific camera parameters, as was established in Equation 4.5. The size of the CMOS array will be constant, but to enable a range of reception distances, a variable angle of view, θ, would allow the sensor to zoom in on transmitters at long distances. Optical zoom is already used in many small form factor cameras. Using our particular experimental configuration, which we anticipate will be typical of most configurations with current hardware, 8 bits were used to quantize data and saw an array gain efficiency of 0.36. Using these terms in Equation 6.15 gives

$$\mathrm{SNR} \propto \frac{P_{Tx} \times 0.36n}{r^2\left(\frac{\max(P_{amb},(P_{Tx}/r^2))}{3\times 2^{16}}\right)} \tag{6.16}$$

and extracting the numeric constants in the proportionality leaves

$$\mathrm{SNR} \propto \begin{cases} \frac{P_{Tx} \times n}{r^2} & \text{for } P_{Rx} > P_{amb} \\ \frac{P_{Tx}^2 \times n}{r^3 \times P_{amb}} & \text{for } P_{Rx} < P_{amb} \end{cases} \tag{6.17}$$

where the P_{Rx} term is reflected as P_{Tx}/r^2 in the case where scene brightness causes quantization noise loss. Assuming all camera parameters, including θ, are constant, Equation 4.5 gives the linear number of pixels decreasing by a factor of $1/r$. Since G is a function of total pixels, n is an area, and array gain without adaptive optics decreases as $1/r^2$. Replacing n in Equation 6.17 with $1/r^2$ maintains the proportionality, but further simplifies it to

$$\text{SNR} \propto \begin{cases} \frac{P_{Tx}}{r^4} & \text{for } P_{Rx} > P_{amb} \\ \frac{P_{Tx}^2}{r^5 \times P_{amb}} & \text{for } P_{Rx} < P_{amb} \end{cases} \tag{6.18}$$

which is maximally simplified using a radiant flux model to project a smooth exponential decay. However, this proportionality should not be confused with a direct measure SNR. It is only a bound that informs the envelope of decay. Signal recovery for VLC with IMDD on commodity CMOS sensors relies on the ability to separate high and low values in the quantized output. With extraordinarily low noise, even a shift between adjacent quantization values would be sufficient to recover ones and zeros. Output variations approaching the full dynamic range of the sensor, 256 values for an 8-bit quantizer, are not needed to recover a single bit of data. The average noise, measured in Section 3.2.1, had an average standard deviation of approximately 3 quantization values. As discussed in Section 4.6, SNR and BER become a function of how much separation we provide between the quantized values for a one bit and a zero bit.

Through this analysis, we have identified the primary factors that influence the spacing of output quantized values based on the intensity of the signal reaching the camera. Relative scene-to-signal brightness sets the quantization bin size and is the dominant factor. When the signal is significantly brighter than the background scene, using filters to attenuate all the energy arriving at the sensor produces gain. In this case, attenuation compresses the full dynamic range of the signal, minimizing losses from truncating the overshoot of the maximum quantization value, while also suppressing the strength of the background. When the background is significantly brighter than the signal, quantization noise increases for the signal. Attenuation does not help in this case, but noise suppression can still increase SNR. Using multiple pixels, we empirically measured an array gain of $0.36n$. Using polarization filters, selective gain was achieved with more light from the background being filtered out in proportion to the signal.

CHAPTER 7:
Conclusion

In this dissertation, we focused on improving the performance of outdoor VLC, specifically targeting vehicular applications. The ability of cars and other vehicles to communicate with each other and infrastructure will be crucial to future efforts to improve the safety and efficiency of transportation systems. Rather than rely on the RF alone, visible light offers an opportunity to communicate in less congested bands. At the same time, leveraging existing hardware will reduce the space and power needed, and in turn cost, for vehicle systems. While there are many opportunities to optimize a VLC system, we focus on SNR since improved SNR offers opportunities to transmit data faster, farther, or more robustly at the system designers' choosing.

As LED technology has matured over the last two decades, a growing body of research is investigating ways to simultaneously transmit data and provide illumination — especially for indoor applications. The outdoor environment and long ranges required for VVLC require significantly more effort to mitigate noise and achieve serviceable SNRs. We began our empirical measurements by establishing a baseline for daylight noise across an entire solar day and establishing a sufficiently accurate statistical model for further analysis.

With an understanding of the noise contending with VLC signals in an outdoor environment, we tested numerous methods of improving received SNR via filters and processing at the receiver. We assume little control over the transmitting headlights and taillights — other than the ability to modulate data — since their primary purpose is to provide illumination and signaling for the vehicle. Likewise, we focused on the use of low-cost, commodity CMOS sensors as they are the most likely to be ubiquitously deployed on vehicles for other purposes such as lane assistance. Within these constraints, we assessed the impact of color filters, polarization filters, optical magnification, and multi-receiver configurations.

While working with commodity CMOS sensors, we found little wavelength-specific gain from colored filters. Using the existing CFA and compression algorithms required to store video files, the overall impact of the color filters was primarily signal attenuation and not spectral gain. However, using polarization filters provided significant gain in all circumstances — even from an unpolarized headlight — and should be considered as a viable low-cost option to improve outdoor VLC performance without interfering with other functions of the onboard vehicle camera systems.

Extending performance to longer ranges than previously achieved in the literature, we found that optical magnification to spread the wavefront across more pixels is required. We were able to rely on a compact monoscope to provide 20× magnification without needing to resort to larger telescope-type optics. In terms of practical design, many late-model camera phones can already provide 15× magnification and pancake lenses could provide sufficient zoom without needing bulky optics in vehicular applications. Magnification primarily increased the ratio of pixels filled by the transmitter versus the background, thereby reducing noise from the scene in the ROI unrelated to the transmitter. With a sufficient number of filled pixels, light communication with commodity hardware was achieved at an unprecedented range of 1.6 kilometers.

Building on these results, an analysis of the factors impacting achievable SNR — and in turn range — of an outdoor VLC system was presented in Chapter 6. At ranges practical for vehicular communication in sunlight, SNR is dominated by the overall signal power to scene brightness ratio driving quantization noise and array gain enabled by multiple pixel fill.

7.1 Findings and Contributions

While many proposed VLC systems struggle in daylight conditions, we have found that using commodity CMOS sensors can allow communication at long distances and low cost. Using CMOS sensors results in a slower sampling rate than using photodiode systems but enables spatial filtering that rejects noise from the background scene. In the spatial selection process, we found that a correlation-based weighting derived from the fundamental frequency of the preamble better isolates the signal than geometric expansion. Even with well-selected signal pixels, we found tracking and stabilization remain an important challenge for VVLC. Another benefit of using a camera sensor, rather than a photodiode, is the potential to leverage digital tracking based on optical flow to follow vehicles moving in the scene.

Assessing opportunities to improve SNR, we found quantization is a driving performance limiter of commodity sensors in daylight communications. A bright scene leads to larger quantization steps, reducing the number of steps the signal modulates over. In dark scenes, this is not an issue since the signal can use the full range of the quantizer. However, as the background gets brighter, the quantization swing produced by the light becomes proportionately less. Using the 8-bit output of a camera phone, this is very pronounced. By extension, any digital communication system, even with a photodiode front end, will end up quantizing the incoming light, and brighter scenes result in lower signal SQNR. In bright conditions, the attenuation caused by filters helps mitigate quantizer bloom, but attenuation at night or in other dark environments would be counterproductive.

We also found polarization filters provide gain in all tested configurations. Beyond attenuation, the polarizer is a discriminating filter that allows more signal to pass relative to the background. Sunlight scattering through the atmosphere becomes polarized perpendicular to the direction of propagation. If the sun were at zenith, this would produce a degree of horizontal polarization in the atmosphere. During the brightest parts of the day, the sun is relatively high. Specular reflections from roads and other surfaces also become horizontally polarized. A vertical polarizer cuts down on both of these horizontally polarized components of the background, while the headlight is unpolarized and thus less attenuated.

Finally, we found that using multiple pixels does produce array gain in the receiving camera. The impact of color filters reducing the number of active pixels under the CFA showed that the more sub-pixels were used, the better SNR performed. At long distance (1650 m) magnification spread the signal from a small fraction of a pixel to nearly 40 pixels, lifting the signal from the noise floor by more than 10 dB, sufficient to allow communication at unprecedented ranges for VLC using commodity hardware.

In summary, our specific research contributions include:

1. A new set of empirical data recording actual daylight background noise as it impacts outdoor VLC over the course of a full day. While often recognized as a challenge, most of the literature on outdoor VLC adopts analytic models [88], [153] and the few sources that do measure it [63] only assess one or two times during a day. Establishing the statistics for noise across a full solar day — and collected through numerous filters — provides foundational data to enable future work.
2. Documented performance results employing a variety of optical filters and assessing their impacts on OCC. Many works have assessed the impacts of blue filters, most

finding throughput gain [52], [63], [154], [155] and others questioning net gain [138]. However, beyond exotic configurations [135], [140], [156], no literature has baselined performance across off-the-shelf green, red, and near-IR filters for outdoor VLC.

3. Demonstrated tremendous performance gains leveraging a simple linear polarization filter at the receiver. Other literature has suggested polarization as a means of encoding data for VLC [157]–[159], but to our knowledge, no other studies have assessed the use of polarization to improve receiver performance for unpolarized outdoor VLC transmissions. We previously employed polarization encoding to communicate over half a kilometer [75], but we have now shown that using polarization filters provides significant gain with an unpolarized LED headlight source — even 1.6 km away.
4. Empirically demonstrated the ability to transmit data via headlight modulation to commodity cameras at unprecedented ranges. While FSOC and other bespoke optical communication systems have long been able to deliver multi-kilometer communication, no other known outdoor VLC research leveraging vehicle lights and low-cost cameras (or even custom photodiodes) has shown ranges greater than 400 m (see Table 2.1), and we demonstrated throughput at 1.6 km.
5. Leveraging our empirical data and known link performance and attenuation equations, we established that the dominant components of SNR for outdoor VLC are relative scene brightness and pixel fill. Scenes brighter than the received signal cause loss of SQNR. At moderate ranges, attenuating filters increase SQNR. At longer ranges, multi-pixel fill is needed to enable array gain supporting communication.

7.2 Future Work

Much work remains to implement meaningful V2V communications with the market saturation needed to support an ITS. There are continuing opportunities for the selection of optimized error-correcting codes and enhancing modulation schemes for VLC. Other work has begun to bound performance in actual vehicle conditions accounting for headlight beam patterns, geometry, and vehicle speed [3], [63], [160]–[163], and it is worth continuing toward operational vehicular systems. Further low-cost VLC applications are being explored for Internet of Things devices [164]. All of these studies could find gain through polarization and manage pixel fill to enable extended ranges.

While we have constrained our study to one transmitter, multiple transmitting fixtures on the vehicle could be used to send more data through the channel. Research has been conducted using unique pulse position codes to allow transmitting data from two separate lights to a single receiver while mitigating the impacts of mutual interference [165]. However, using a CMOS sensor as a receiver camera, these two data streams are already spatially separated and do not cause mutual interference as long as the two lights remain in distinct pixels or clusters of pixels. Taking this further, some late-model cars include arrays of LEDs as headlights and taillights. For example, Porsche has introduced HD Matrix LED headlights designed to adaptively provide optimum illumination [166]. In practice, they provide eight distinct points of light on the front of the vehicle, as seen in Figure 7.1. Rather than using two lights to provide twice the throughput, eight lights allow for eight times the throughput — so long as the combination of range and magnification at the receiver allows for spatial separation. Future work may maximize throughput for vehicular implementations layer by establishing optimal array geometries leveraging our SNR improvement techniques.

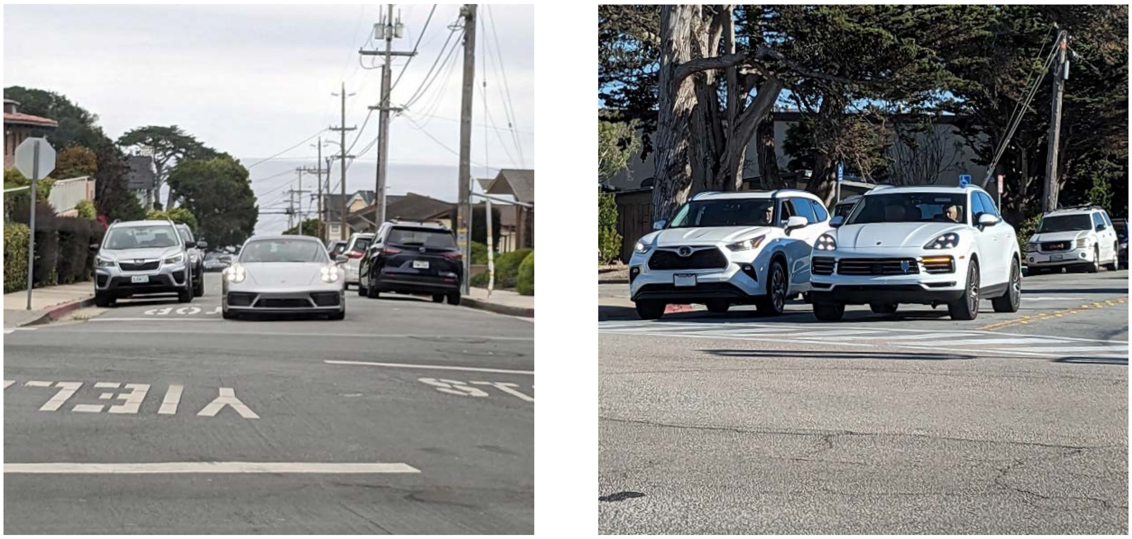
(a) (b)

Figure 7.1. HD Matrix LED headlights seen on the centered vehicles, (a) a Porsche Cayman and (b) a Porsche Macan, during daylight conditions.

Our finding that attenuation can create gain by minimizing quantizer saturation suggests dynamic exposure compensation may significantly improve the performance of outdoor

VLC links. We have demonstrated the impact of scene brightness, expanding quantization bin size and reducing SQNR for the signal. In Chapter 3, we saw that while background luminance varies significantly across the day, the camera tries to hold background white and black regions at the same quantized values. Attenuating filters improve SNR during the periods of the day when the signal is far brighter than the background, but are detrimental at very long distances or with lower contract ratios between scene and signal. Future work may explore dynamic attenuation through software exposure control or photosensitive filters.

Finally, building on software exposure control, coding and application programming interface (API) development could unlock more performance from the same commodity CMOS sensors. We processed the received data after demosaicing and video compression. Lower-level software interfaces may allow taking advantage of the CFA pixels directly for filtering rather than layering other optical windows in front of the camera. This could continue to allow reuse of existing camera hardware while more fully leveraging the available data before compression. The IMX363 sensor used in our experimentation has a 10-bit quantizer [117], but we could only access 8 bits of resolution post-processing. Directly accessing the full potential of the hardware could increase precision and improve SQNR.

Implementing VVLC offers great potential to augment RF, reducing network congestion and improving vehicular safety and efficiency. We have established the key performance parameters impacting SNR for long-distance VLC using commodity hardware and shown opportunities for improving SNR through attenuation, polarization, and array gain. Future work toward VVLC in ITSs will ultimately involve marrying these enhancements with the critical work of engineering system design and the development of standardized communication protocols for interoperability.

APPENDIX A:
Light Units

Units for light are not broadly familiar and may not be immediately intuitive. They have similar-sounding names for different aspects of light output and arrival at points in space. Light units also deviate from units typically used in other electrical and RF engineering since they are adjusted to the sensitivity of the human eye. This appendix briefly covers some fundamental units and terms dealing with light.

Light is an electromagnetic wave, familiar to readers with a background in RF, but also only arrives in discrete, quantized units — photons. Each photon carries energy correlated to its wavelength, λ, which can be calculated as

$$E(\lambda) = \frac{hc}{\lambda} \tag{A.1}$$

where $h = 6.6256 \times 10^{-34}$ J·s (Plank's constant) and c is the speed of light in a vacuum. Alternately, converting wavelength to frequency, ν, $E(\nu) = h\nu$ [167]. While the quantum nature of light is critically important in the operation of silicon photodetectors, in many uses a radiant field approximation — as is used to model propagating RF waves — is sufficient to describe the behavior of light.

The SI unit for light is the candela. Candela measure the strength of visible light in a particular direction. The candela is defined as "the luminous intensity in a given direction of a source that emits monochromatic radiation of frequency 540×10^{12} hertz and that has a radiant intensity in that direction of 1/683 watt per steradian" [168]. The value of 1/683 was chosen to maintain consistency with the historic candlepower unit, based on the luminous intensity of a spermaceti candle [169].

The candela being defined by steradian presents another way to see how the inverse-squared law impacts light. As seen in Figure A.1, the surface area of a steradian is equal to the radius squared. A receiver of fixed size will take up less and less of this r^2 area as distance increases, receiving proportionately less light energy.

Lumens (lm) and lux (lx) are derived units of the flow of visible light from or through a surface. These visible light quantities are calibrated to the sensitivity of human vision (photometric flux) and is not all radiant energy (radiometric or radiant flux). Photometric flux, lumen, is measured in candela·steradian, recalling a candela was defined at a particular wavelength near the peak of human visual sensitivity. When purchasing bulbs, lumens normally consider isotropic radiation in all directions (over 4π steradians), as illustrated in Figure A.1. The luminous efficiency of a bulb is found by dividing lumens by watts. If one were concerned about total radiant flux, not just photometric flux, watts measure output in joules per second.

Illuminance, lux, provides a directional measure of how much light flows through, or lands on, a surface area [170]. Lux are lm/m^2, but analogous non-SI units such as foot-candles are often also used, documenting how much light, in candlepower, falls on a one square foot area. If the normal of the illuminated surface is not aligned to the incoming field vector, received strength diminishes roughly proportional to the cosine of the angle between the vectors. The cosine relationship between the normal and the incoming light is defined by Lambert's Law.

Contrasted with illuminance, luminance measures light output in cd/m^2. This quantity is called a nit. Nits are often used to describe the light output of displays. Solar irradiance can also be quantified in cd/m^2.

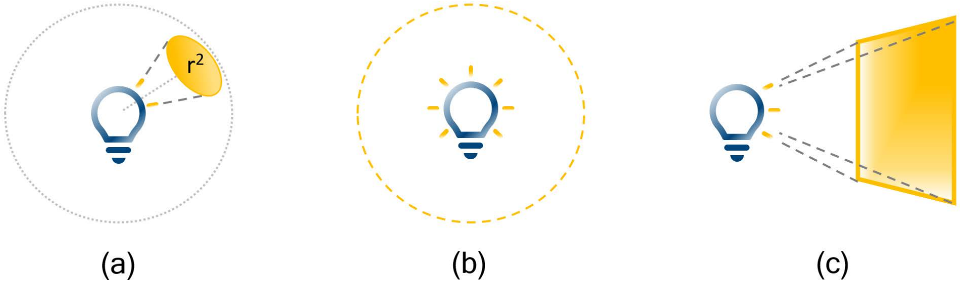

Figure A.1. Units used to describe luminous flux. (a) Candela are the SI base unit for illuminance and capture how much energy flows in a particular direction, in W/sr at λ=540 nm. (b) Lumens are cd·sr, often used to capture total light output from a source measured over 4π steradians. (c) Lux capture the amount of illuminous flux per unit area, lm/m^2.

Returning to photons, the 2009 meeting of the Consultative Committee for Photometry and Radiometry for the International Bureau of Weights and Measures [171] proposed clarifying language for the definition so that “the candela is the luminous intensity, in a given direction, of a source that emits monochromatic radiation of frequency 540×10^{12} hertz and that has a radiant intensity in that direction of 1/683 watt per steradian. This radiant intensity corresponds to a photon intensity of $(683 \times 540 \times 10^{12} \times 6.626\,068\,96 \times 10^{-34})^{-1}$ photons per second per steradian.” For most practical engineering purposes, a radiant flux model provides sufficient granularity.

THIS PAGE INTENTIONALLY LEFT BLANK

APPENDIX B:
Transmitter Construction

Previous NPS theses focusing on experimentation with VLC have leveraged digital multiplex (DMX) lights [165], [172]. DMX lights are designed to provide illumination and effects on stages and are easily controlled by dedicated software over USB. While easily controlled and capable of providing similar luminous output to headlights, they are limited to modulation at about 25 Hz. This frequency is well within human flicker perception. The design of DMX lights makes sense for theatrical lighting but it is not well suited to higher-speed VLC. In order to truly assess a V2V light configuration and allow higher speed modulations we constructed a custom LED car headlight.

We acquired an LED headlight bulb from a major online retailer for experimentation. Such bulbs are advertised as capable of replacing legacy stock bulbs in the housing already in the vehicle. While late-model production vehicles often include LED lights as part of the original equipment, a separate bulb outside of a fixed housing better facilitates engineering analysis. The LED retrofit bulbs we used are shown in Figure B.1 in their original packaging.

Figure B.1. Headlight bulb with packaging.

We began our investigation into the modulation capabilities of the bulbs using a signal generator on the bulbs without modification. The light bulb specifications indicated an operating range of 10 to 30 V (in line with typical vehicle electrical bus voltages, notably 12 V from a car battery), but not much other technical data was included in the packaging. We found the LEDs began to illuminate around 5 V and grew gradually brighter up to 10 V.

Next, we assessed frequency response, which would enable modulation to transmit data. Adjusting the frequency of pulses provided by a signal generator and capturing light output with a high-speed camera, we observed a very clean square wave of light output at 10 Hz. Increasing frequency, at multiples of the camera frame rate, aliasing was observed. This is a sampling artifact and not a limitation of the LED bulb. However, at 180 Hz the bulb began to behave erratically. A 180 Hz square pulse should be imperceptible to the unaided human eye but was clearly flickering. At 190 Hz the bulb simply went dark producing no light whatsoever. The LED bulb was significantly more complicated than a simple LED, presenting challenges to modulate and encode data.

We subsequently removed the heat sink and bulb housing to investigate the actual circuitry included in these relatively low-cost light bulbs. Figure B.2 shows the light bulb removed from the heat sink and housing. Grids of 3 × 10 white LEDs are seen on each arm and the small printed circuit board (PCB) contains circuitry to provide a fixed current to the LEDs. The stock headlight bulb circuit takes whatever the input voltage is input, steps it down appropriately, and then provides constant current to the LEDs to provide a constant level of brightness. Figure B.3(a) enumerates the main components on the PCB.

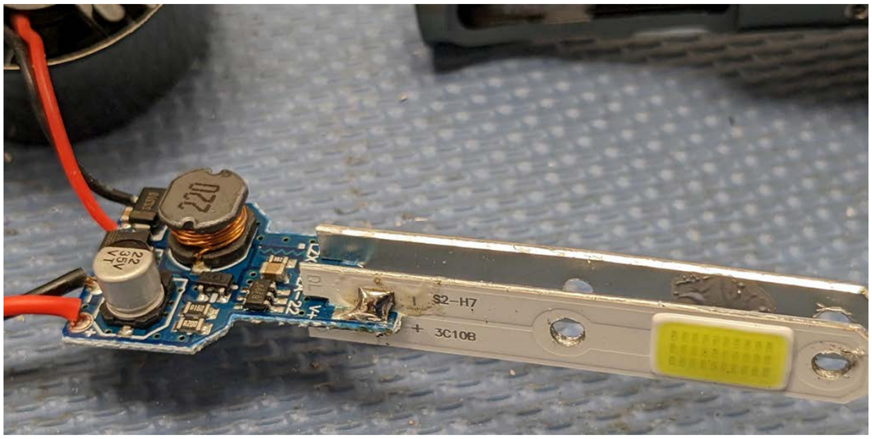

Figure B.2. LED bulb removed from housing.

While this design for constant current makes sense in the manufacturer's intended usage, in order to modulate the bulb we need a way to rapidly switch on and off current to the LEDs. Our initial hope of simply modulating the electrical bus feeding the bulb (analogous to [173]) would not be effective for data transmission since the circuitry is designed to suppress these sorts of transients.

Since modulating the electrical bus would be infeasible with the stock bulb, we replaced the PCB with a new circuit, shown in Figure B.3(b). Using a femtobuck [174] also provides constant current and the ability to step down voltages both provided a control pin that could toggle the output current to the LED's on and off. Essentially this provides the same capability as the stock PCB but allows switching the lights on and off with a 5 V control pin. This control signal was easily generated as the output of the Arduino microcontroller GPIO pin. The femtobuck, driven by a 12 V source, could provide 660 mA of constant current to the LED, rapidly switching the light faster than electrical bus-based modulation and providing more power than would be available from the Arduino alone.

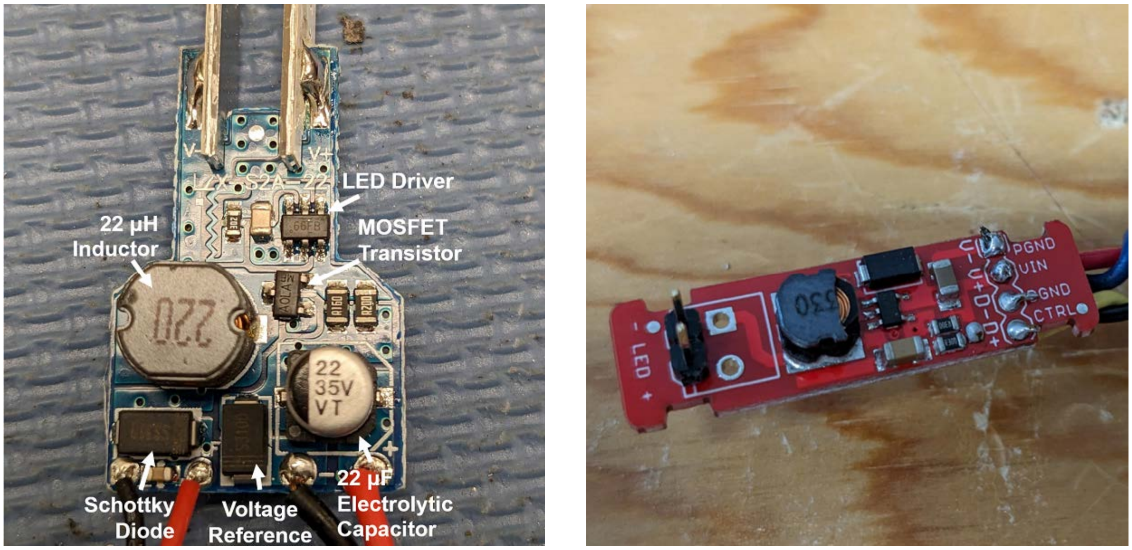

(a) (b)

Figure B.3. LED bulb drive circuits. (a) The stock driving circuit designed to deliver constant current with component call outs.(b) The femtobuck drive circuit used in experimentation to deliver 660 mA to the bulb, controlled by a 5 V pin. The overall layout is similar to the original board, noting the 33 μH inductor in place of the 22 μH one, but has switchable output.

The Arduino control circuit was validated using an oscilloscope and small LED on a breadboard (Figure B.4). Having confirmed the Arduino output, it was connected to the control pin on the control pin of the femtobuck circuit. The femtobuck was also connected to a constant 12 V DC supply and the headlight LED matrices (with the PCB removed).

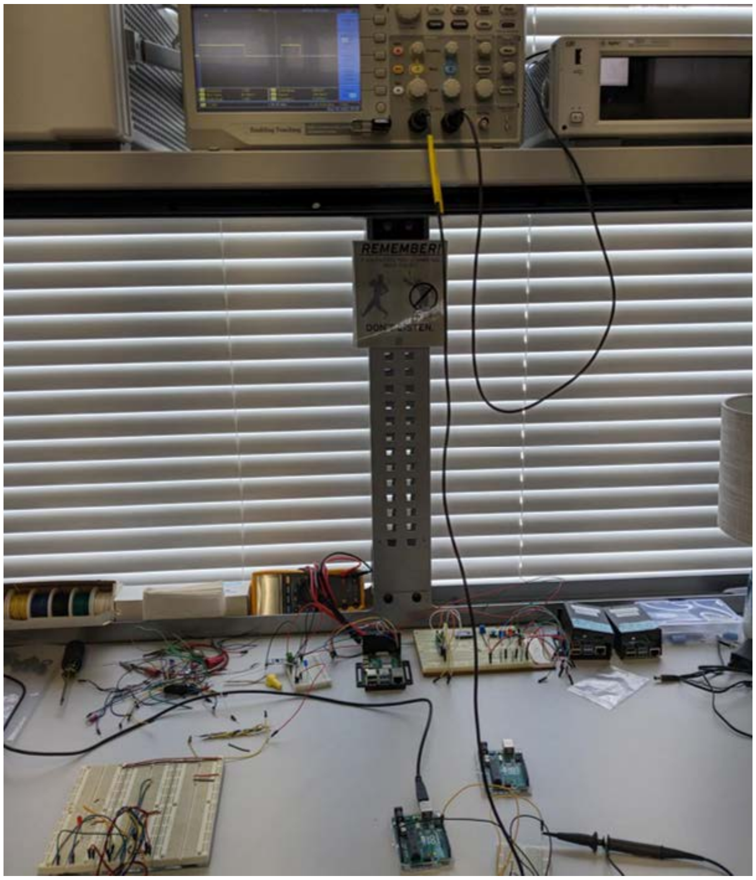

Figure B.4. Bench testing the Arduino drive circuit with a small LED. The 5 V signal from GPIO pin 13 was subsequently used to control a femtobuck switch 660 mA to the headlight LED.

After confirming proper operation, the headlight LED was installed and an actual car headlight housing. In our case, the housing chosen due to cost and availability was from a Ford Taurus. The smaller side reflector was used emulating a daytime limit ring light rather than the main reflector. Figure B.5 shows the controllable headlight illuminated.

Figure B.5. Customized, controllable LED mounted in the left side reflector area of the headlight assembly.

APPENDIX C:
Transmitter Code Development

In order to test the receiver performance of any communication system, thorough knowledge of the transmitted signal is required. Since we were using an Android camera as a receiver, an Android transmitter was also considered. We found significant fluctuations in timing in both the receive and transmit capabilities of our own custom Android apps. Following this we focused on using a dedicated microcontroller, the Arduino Uno, which provided more reliable timing. The microcontroller is capable of very precise timing — down to the clock cycle — by calling C++ assembly subroutines, but we were able to achieve near millisecond precision via the C functions available directly in Arduino sketches.

C.1 Android

A key aspect of digital communications is timing. Synchronization between the clock at the transmitter and receiver ensures that bit windows will align so samples can be properly decoded. We began developing a custom Android app to reduce processing during video recording since receivers in OCC introduce many artifacts to improve subjective image quality. Through this developmental effort, significant time variations between frame captures were discovered. While these variations are not enough to impact casual viewers of a video file, they do introduce significant timing challenges for digital communications.

In order to better understand the timing characteristics of an Android device with a less complicated process, we developed a transmitter that toggles the flash on and off rather than leveraging the whole camera processing chain. This effort also uncovered timing inconsistencies. While the transmitter worked well at full-second intervals, variation of the order of milliseconds was tremendous.

C.1.1 CameraX

Appreciating that cell phone cameras are designed to provide the most pleasant picture possible through processing, what is needed to receive and decode signals is a predictable and consistent sampling at the receiver. CMOS sensors, as used in cell phones, make sense for many applications due to their low cost and broad availability. However, both Android and iOS devices constantly try to compensate for changes in brightness. This creates DC drift leading to challenges in post-processing. Recording high definition videos also produces very large files, which are costly in terms of both memory and process time. Collecting scene data closer sensor itself can helps reduce software-induced noise. If analysis can be done on the byte buffer in the phone, rather than on a video file, video compression artifacts and file transfer time can be avoided. With this in mind, we set out to develop a stripped-down Android camera app to directly pull frame luminance values.

Android applications are built in the Android Studio application provided by Google. The integrated development environment provides a what-you-see-is-what-you-get capability for developing the graphical user interface shown on screen. It also provides access to numerous supporting XML files and the Kotlin (successor to Java) code files needed to run applications. Android is first and foremost about user experience and is designed to prioritize on-screen tasks and respond to user inputs. Kotlin, like Java, is a high-level language that helps facilitate easier, less error-prone coding but is not optimized for direct hardware interface or speed. The language is also very object-oriented. Properties and actions are defined within a hierarchy of objects.

The camera is accessed through a Jetpack library, which provides object-oriented access to the camera. In 2017, Google released the CameraX API [175], designed to provide easier access to the camera for application developers. The predecessor API, Camera2, required a significant of programming to instantiate and close various aspects for the camera on each screen in the application. CameraX provides a wrapper around many of these functions and handles most of the housekeeping associated with calling the camera API in an Android application. This abstraction significantly lowers the barrier to entry for adding camera functions to an application, but it also does abstract away some of the fine-grain controls. Generally, Camera2 functionality can be called to override CameraX behavior, like accessing an assembly routine from C but at a much higher level. This allows some control over specific behaviors for white balance and exposure compensation, but can also create issues with settings CameraX otherwise manages.

Working through the online Android developer courseware provided by Google, fairly quick progress was made from a basic “hello world” app to multi-screen apps capable of basic calculations and sharing data. The online CameraX tutorials also facilitate rapidly building an app to take pictures and record videos. However, many of these tutorials included provided code sections that were not thoroughly explained. In trying to further customize the performance of a custom CameraX app, various layers of object abstraction presented challenges. In many cases, documentation suggested a capability should exist, but the implementation of more complex cases was neither straightforward nor documented.

While falling short of the initial goal to directly calculate received signal data from the byte buffer, we were able to build a custom app that recorded average brightness across the whole frame and exported it via email from the phone. This alone was a huge time saving over downloading videos from the iPhone 13 to extract average luminance in MATLAB employed in [46], but uncovered variable timing in the frames. Figure C.1 shows the Pareto histogram of time between images, with histogram bars sorted by frequency and the overall percentage of samples on the top curve.

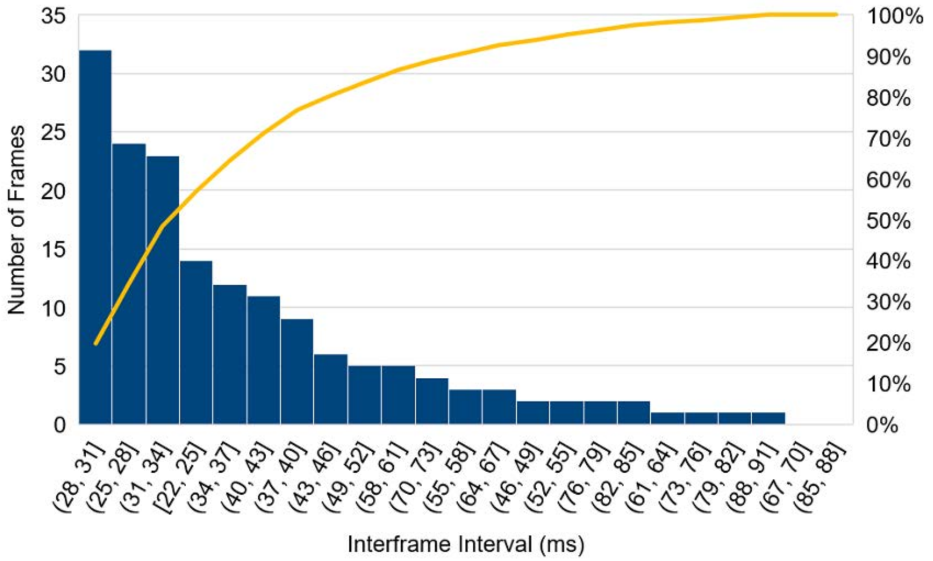

Figure C.1. Pareto histogram of inter-frame interval.

Approximately 70% of the frames were captured in less than 33 ms, the cut-off for 30 FPS. While occasional variability would not disrupt viewing a replay of a natural scene, these jumps lead to bit errors in digital communication. Attempts to tweak Camera2 parameters to speed up frame collection were not successful. It may be possible to sidestep software image enhancement, apply spatial filtering, and decode bits on the phone. However, with limited computer science or application development background, the difficulty and time involved exceeded the resources available, and this effort is left for future work.

C.1.2 DroidCam

DroidCam is an Android and Windows application pair that offers many of the desired controls over video recording. DroidCam was developed to allow an Android phone to be used as a webcam [176]. An app on the phone connects to a computer via WiFi or a USB cable. Another application on the computer accesses the video from the phone to be used like any other webcam for video conferencing or recording. While the computer-side software is all open source, the phone apps are not. Free versions of the app are available in the app store, and a paid pro version is available unlocking more features and control.

Due to challenges with custom software development, DroidCam was used during the initial phases of research and preliminary studies [75] to streamline video collection. For the final experiments — presented in the main body of this dissertation — we shifted from iPhones and a Pixel 3a to the Pixel 6a. DroidCam allows setting the white balance, exposure compensation, focus, and zoom manual, which helps to eliminate many of the software-induced artifacts in the stock phone camera applications in Android 12 and below that we encountered in early development. Shifting to Pixel 6a phones — using Android 13 — for our final data collection, manual control over exposure and white balance in exposed in the stock camera application. In early testing, sending data over USB to be recorded on the computer also reduced the time associated with post-collection file transfers. While offering significant functionality, DroidCam still does not support accessing the byte buffer to extract raw sensor data, as we had initially pursued in our own software development.

Since the computer side applications are open source and we had bought the pro version, we inquired with the software authors about seeing their Android code for academic purposes. They hold their Android source as proprietary but did inform us that DroidCam is written in Camera2 with proprietary customizations for speed. DroidCam does collect cleanly at 60 FPS, better than our application collecting at 30 FPS. The DroidCam authors — who are very well versed in the internal operations of the Pixel camera software stack — also speculated that directly accessing the byte buffers below the Camera2 API would be difficult [177].

C.1.3 Transmitters and Timing

In an effort to better understand the timing anomalies we were seeing recording video on a CameraX app, we shifted from recording to transmitting via the camera flash. A custom app was developed that would take an arbitrary string, convert it to ASCII, and then transmit it by on-off keying (OOK) with selectable bit durations and number of repetitions. The ability to change the message, bit durations, and cycle on screen was significantly faster than using the hardcoded approaches on the Raspberry Pi and DMX transmitters.

The strobing transmitter worked well with pulses in the 100s to 1000s of milliseconds, but the pulse shape deteriorated attempting to produce pulses of single milliseconds. Very short pulses are needed for USFOOK where we need frequencies at multiples of the camera frame rate. The flash transmitter code was revised to remove the ‘sleep’ delay in the loop to just use the cycle time of the loop to delay between pulses. However, this still did not produce clean results. The challenges with using delays in loops in high-level languages also suggest there may be imprecision in Python code implementation on both the Raspberry Pi and DMX circuits. These issues were even found running Python on a Celeron N3450 Windows 10 laptop [75], so the challenge is not constrained to the Linux kernel or single-board computers.

The following code snippet is the Android Kotlin code section meant to simply transmit a high or low bit and wait a specified amount of time.

```
/** Toggles torch on and off based on the settings and encoded message string.*/
fun transmitMsg() {

    // Iterate through encoded string holding each message bit for pulse duration
    for (msgBit in encodedUserString.iterator()) {
        val bitVal = msgBit.code.toInt() - 48      // Offset from ACSII to number

        if (bitVal == 1) {
            cameraManager.setTorchMode(cameraID, true)          // bright for one
            Thread.sleep(pulseTau)
        } else if (bitVal == 0) {
            cameraManager.setTorchMode(cameraID, false)          // dark for zero
            Thread.sleep(pulseTau)
        } else {
```

```
            Toast.makeText(this, "Data Error", Toast.LENGTH_SHORT).show()
        }
    }
    Toast.makeText(this, "Transmission Completed", Toast.LENGTH_SHORT).show()
    cameraManager.setTorchMode(cameraID, false)           // make sure turned off
}
```

C.2 Arduino

In an effort to provide better pulse timing, we shifted from Android and Raspberry Pi transmitters to developing on an Arduino board. The Arduino microcontroller can be programmed in a variant of C or directly with assembly commands. Using assembly to account for the time delays on each register shift and compare, timing could actually be controlled very precisely against the 16 MHz clock on the microprocessor. Figure C.2 shows the very clean pulse shape generated using assembly for 10 ms pulses. The Arduino provides consistent squares, 0.05 ms off of target, vs the Android flash being non-symmetrical on high and low pulse times with variance of multiple milliseconds.

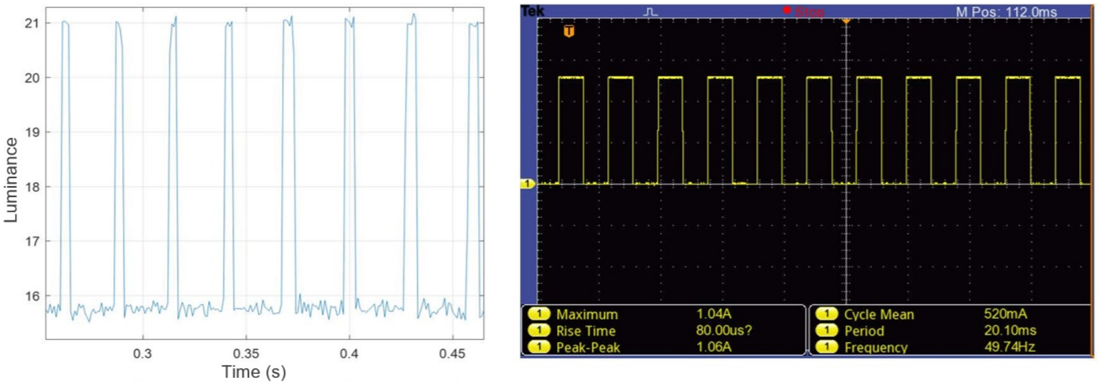

(a) (b)

Figure C.2. Millisecond pulse shape generated by (a) the flash in Android vs (b) an Arduino microcontroller.

The following code is the Arduino sketch used by the transmitter. Tighter loops can be made by calling C language subroutines and individually account for every processor clock cycle at 16 MHz. Precisely counting every instruction, the microcontroller can provide precision within 10s of nanoseconds, but using the built-in delay function with millisecond resolution was more straightforward and still allowed communication.

```
// Arduino sketch to transmit message as ASCII characters
// D.E. Barber - 01 September 2023
// Uses onboard LED for initial validation, pin 13 also serves to
// drive external LEDs and the headlamp
// Initial version resulted in a bit duration of approximately 7.2
// sample frames on the Pixel 6a 1/8x slow motion
// This update decreases bit time from 30 ms to 13 ms to produce
// approximately 3.12 frame bits
// Otherwise some options are: 4 ms -> 0.96 frames, 8 ms -> 1.92

// Initialize our delay times for turning the LED on and off in ms
int bitDuration = 13;          // bit duration in milliseconds
int preambleTailSpace = 250;   // wait time after preamble

// Initialize variables
String msgData = String("GoNavy.BeatArmy.");
                    // test string to transmit (balanced 1s and 0s)
unsigned int msgDataLength = msgData.length();
                    // the length of message string
char sendChar = char('1');
                    // initial variable to hold letter to transmit
int myPreambleLength = 32;
                    // number of cycles in the preamble

void setup() {
  // Initialize digital pin LED_BUILTIN (pin 13) as output
  pinMode(LED_BUILTIN, OUTPUT);
}

void loop() {
  // Preamble sequence of 32 highs and lows
  for (int i = 0; i <= myPreambleLength; i++) {
    digitalWrite(LED_BUILTIN, HIGH);
    delay(bitDuration);
    digitalWrite(LED_BUILTIN, LOW);
    delay(bitDuration);
```

```
  }
  delay(preambleTailSpace);

  // Gets the character at each position in the message
  for (int i = 0; i <= msgDataLength; i++) {

    // Get the character at the current position in msgData
    sendChar = msgData.charAt(i);

    // Break character into 8-bit ASCII for transmission
    for (uint8_t bitMask=128; bitMask !=0; bitMask=bitMask>>1) {
      if (sendChar & bitMask) {
        digitalWrite(LED_BUILTIN, HIGH);
        delay(bitDuration);
      } else {
        digitalWrite(LED_BUILTIN, LOW);
        delay(bitDuration);
      }
    }
  }

  // 5 seconds of off time between cycles of preamble + message
  delay(5000);
}
```

APPENDIX D:
Additive Manufacturing for Camera Mounts

To ensure stable, repeatable measurements using Pixel 6a camera phones, custom adapters were developed using additive manufacturing. These included a lens mount and tripod adapter. The tripod adapter provided a steady position for the camera to allow noise baselining and minimize the need for optical tracking and stabilization for signal recordings. The lens mount allowed standard 55 mm camera lens filters to be affixed directly in front of the Pixel 6a camera sensor without the need for other optics or magnification. This configuration provided an interchangeable test bed, showing what could be achieved by applying filters within or directly in front of the camera.

Component development followed a basic pattern of detailed measurements, rough sketching, computer aided design (CAD) model development, model conversion, and 3D printing. Measurements of the camera, lens, and generic tripod adapter were conducted manually with rulers and calipers. Spatial visualization of component alignment was achieved by pen-and-ink drafting, before building a CAD model. CAD models were developed using the online tool Tinkercad by Autodesk [178].

Within Tinkercad, designs are created by combining various geometric shapes in a workspace. Shapes, such as rectangular prisms and cylinders, are resized as needed once added to the workspace. Rotations and displacements allow overlapping the shapes as desired to create more complicated shapes. Additive merges create larger objects from the overlap, while subtractive merges create holes in the existing shape. Completed shapes can be downloaded as .STL stereolithography files.

In order to print stereolithography models, they must first be converted to specify how the 3D printer should build them. The 3D printer used was an Ultimaker 5 which produces shapes through a fused deposition model. Essentially, it is a very precisely controlled hot glue gun with polylactic acid (PLA) filament, such that the stacked melted plastic builds the desired shape. Ultimaker Cura is 3D printing software package that converts the .STL design into the specifics needed for 3D printing [179]. Printing parameters defined during the slicing process include the thickness of the shell of the 3D object, how densely it is in-filled, and adjustments to trade off print speed versus the granularity of details in the final print.

After Cura completes the translation, its output can be sent over a network or transferred to the printer on a universal serial bus (USB) drive. After selecting the desired files, no further interaction is required during the print job, very similar to a paper inkjet. However, the process of gradually laying down thin filaments of melted PLA to build up a shape is much slower. Print time for each of the custom phone adapters was 8-9 hours. Figure D.1 shows the CAD model for the lens mount and the Ultimaker printing the sliced design. The final product, a 55 mm lens mounting adapter for the Pixel 6a, is shown in Figure D.2.

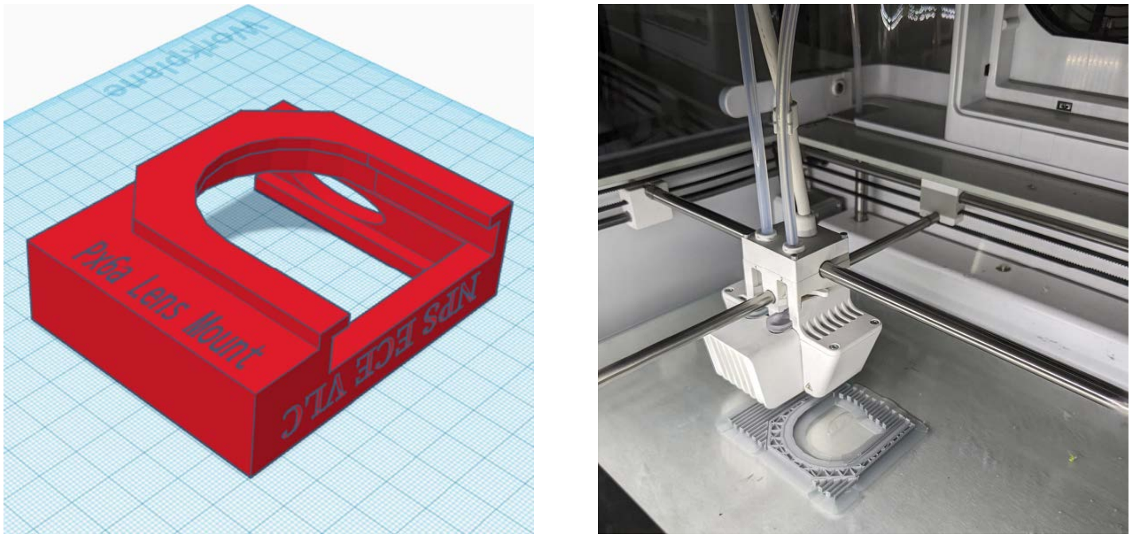

(a)

(b)

Figure D.1. Additive manufacturing showing the 3D design rendered online with (a) Tinkercad and (b) the lens mount being printed on the Ultimaker 5.

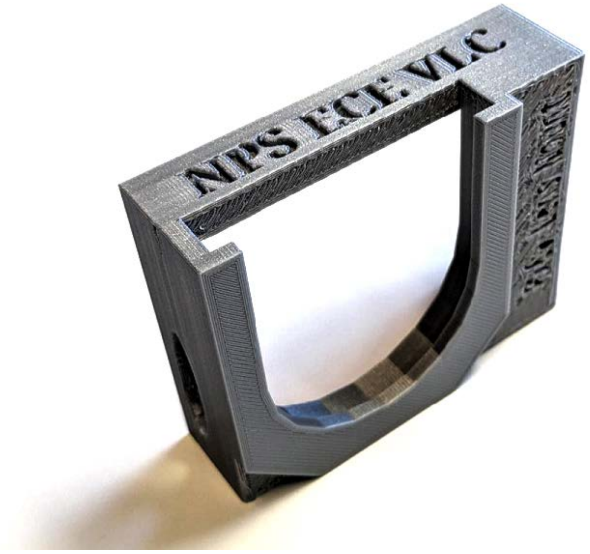

Figure D.2. A printed lens mount, one of several pieces used to fix and stabilize the Pixel 6a and filters during experimentation.

THIS PAGE INTENTIONALLY LEFT BLANK

APPENDIX E:
Measured Filter Transmissivity

As presented in Section 5.2, using filters to enhance SNR depends on suppressing noise to a greater extent than signal. Any filter will decrease both signal and noise but, if the spectral shape of the two signals differs, a filter may allow a greater portion of energy from one spectrum or the other. At a high level, the black body radiation curve of solar radiation during the day contains more blue energy than most artificial sources. LED bulbs produce significantly less heat and infrared light than traditional halogen and incandescent bulbs restricting most of their output to the visible spectrum.

The glass filters used in this dissertation include a Gzikai 720 nm near-IR filter, Tiffen Red 25 filter, Tiffen 11 Green 1 filter, Tiffen 80A blue filter, and Tiffen SR linear polarization filter. The near-IR filter appears almost black since it filters out most all visible light, while the colored filters appear red, green, and blue respectively. The polarization filter simply appears grey. To provide a more empirical measure of their actual transmissivity, a high-resolution spectrometer was used to measure their actual transmittance curves, as shown in Figure E.1.

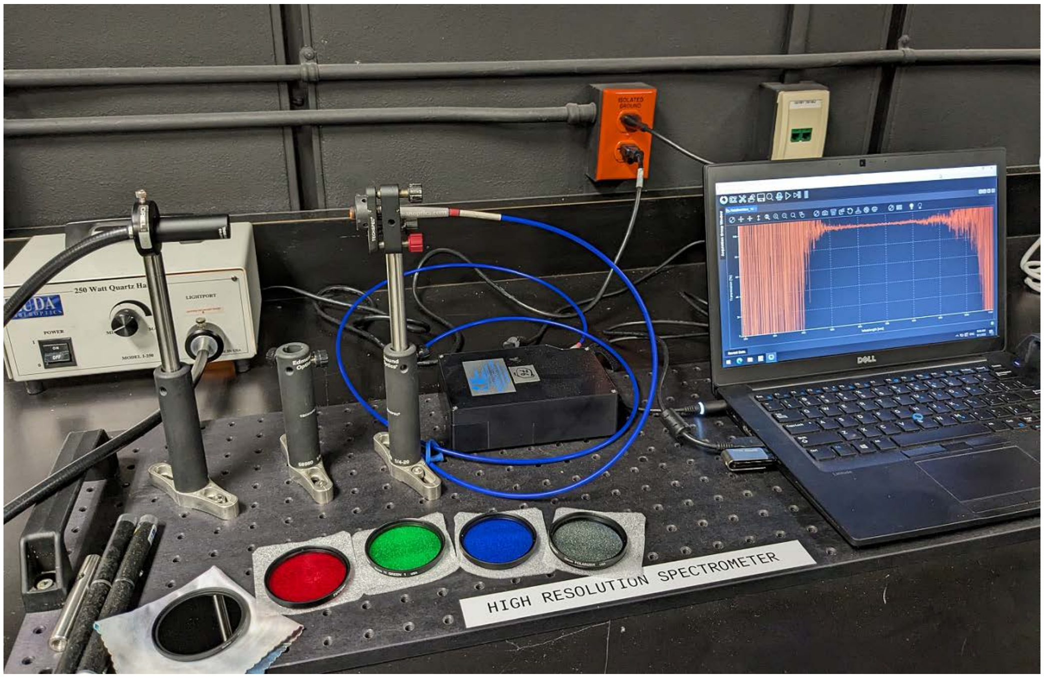

Figure E.1. Lab set up for spectroscopy measurements with the five filters in the foreground.

Measured transmittance is plotted against wavelength in Figure E.2. The near-IR filter does show a long pass transmittance starting around its specified cut-off wavelength of 720 nm. The color filters have peak transmissivity aligning to their own colors — in line with expectations — but attenuate light to some degree at all frequencies. The polarization filter had a relatively flat response across the entire visible spectrum. In line with Malus's Law [141], the linear polarizer blocked approximately half of the light regardless of wavelength.

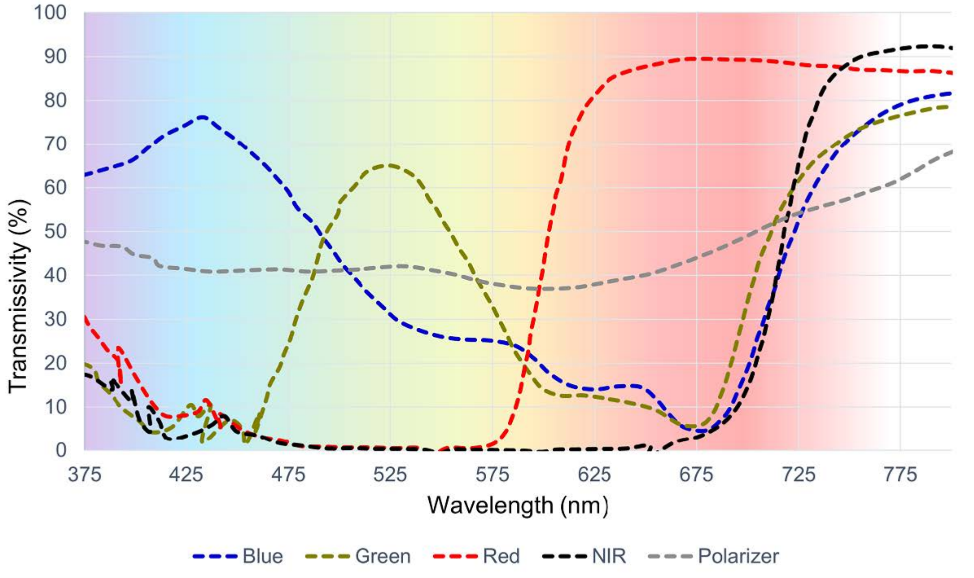

Figure E.2. Transmissivity of the filters used in testing as measured by a spectrometer.

Integrating the area under each of these curves from 400 nm to 750 nm, we can approximate how much of the total incident light energy reaches the camera sensor as captured in Table E.1. The polarizer has a transmittance of 46.3%, near an ideal 50%. Unsurprisingly, the near-IR filter — which appears almost black and blocks most visible light — lets through only 14.7% of the light in the 400 to 750 nm band. Pushing beyond 700 nm exceeds the limits of human visual perception and transitions into the IR. The green filter allows approximately 10% less light through than either the blue or red filters. The lower transmissivity of the green filter better attenuates the scene to increase SQNR, contributing (along with a great number of sub-pixels) to the superior overall SNR results seen in Section 5.2.3.

Table E.1. The overall percentage of light, from 400-750 nm, allowed to pass by each filter.

Filter	**Visible Transmittance (%)**
Gzikai 720 nm near-IR	14.7
Tiffen Red 25	43.2
Tiffen 11 Green 1	32.0
Tiffen 80A Blue	40.1
Tiffen SR Linear Polarizer	46.3

APPENDIX F: Undersampled Frequency On-Off Keying

Given detectability constraints, most VLC rely on IMDD — slightly changing the brightness within the dimming constraint to encode data. While we have addressed the issue of noise and ambient in-band interference using OOK, we have been less thorough in our review of visible flicker artifacts. Our techniques for improving SNR support enhanced communication regardless of modulation technique, and direct intensity modulation provided the most straightforward way to measure SNR. In this appendix, we discuss USFOOK as a promising technique for modulation with frequencies above human flicker perception while continuing to use low-cost commodity sensors with limited sample rates.

Roberts at Intel Labs [143] developed USFOOK in 2013 and it was adopted for use as PHY IV in the IEEE 802.15.7 standard for short-range VLC [19]. USFOOK uses higher frequencies selected to be specifically at or between the harmonics of the receiving camera frame rate. Using higher frequencies avoids visible flicker, while the slower camera frame rate under samples the faster pulses. The undersampling produces a frequency alias at 0 Hz for harmonic multiples and another frequency spike at half the camera frame rate for the offset multiple. This frequency or zero frequency is then easily read as marks and spaces transmitting data. This sort of frequency modulation is more robust to ambient interference, just as FM radio is more robust to noise than AM radio. Undersampling also allows the potential to avoid visible flicker impacting vehicle operators, making such modulation an excellent candidate for increasing the range of VVLC.

In his original paper, Roberts noted that "modulation is applied to signals of opportunity; that is, there may be little or no control over the light intensity and the associated applied level of dimming; which in turn means there is no guaranteed quality of service" [143]. Most work to date on USFOOK has focused on short-range communication, but Plattner and Ostermayer successfully demonstrated USFOOK sending vehicular communications via taillights [4]. USFOOK still demands sufficiently bright LED to overcome noise [180], but having demonstrated OOK at ranges up to 1650 m in this dissertation, USFOOK should continue to work at that distance.

USFOOK Signal Generation

In order to produce a binary USFOOK signal, a modulation frequency matched to a harmonic of the receive camera frame rate and another frequency offset from that harmonic by half of the camera frame rate are needed. For example, assuming a camera recording at 60 FPS, a zero bit could be denoted by a 120 Hz signal while a one bit would be represented by a 150 Hz signal. More generally 1 and 0 bits, 1_{bit} and 0_{bit}, can be represented as

$$1_{\text{bit}} = (\alpha + 0.5)F \mid \alpha F > D \tag{F.1}$$

$$0_{\text{bit}} = \alpha F \mid \alpha F > D \tag{F.2}$$

where F is the camera frame rate (typically 30 or 60 FPS, but up to 240 FPS as was the case with the Pixel 6a), D is the perceptible flicker threshold (nominally 100-200 Hz), and $\alpha \in \mathbb{N}$. These two equations establish the rates needed for USFOOK binary communications. VLC implementation also requires pulse width modulation (PWM) creating an imperceptible dimming — that is, one bit should not visually appear be brighter than a zero bit — and that the frequencies can be generated with pulses achievable by the modulating circuitry and software — which is not an issue using a control circuit like an Arduino microcontroller.

The approach used to implement varying pulse widths and modulation frequencies is aggregating sub-pulses. By summing slivers of pulses, pulses of varying widths are created. To ensure sub-pulse widths sum to the desired pulse timing, they must be divisors of both Equations F.2 and F.1. For the sake of illustration, we can set aside the constraint on detectability (D) and examine the case of small numbers. Using $F = 4$ and $\alpha = 1$, a zero has a frequency of 4 and one has a frequency of $(1 + \frac{1}{2}) \times (F) = 6$. A straightforward sub-pulse frequency ensuring both of these durations can be represented is the product of the frequencies for marks and space, 24. Figure F.1 illustrates sub-pulses clocked at 1/24 generating both marks of length.

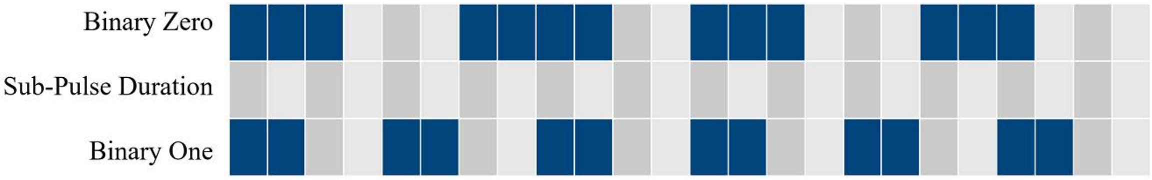

Figure F.1. Timing diagram for marks and spaces based on 24 sub-pulses

Figure F.1 also illustrates that, using these durations, an equal number of high and low pulses are generated for both marks and spaces, providing uniform PWM dimming across both symbols. However, if rather than $F = 4$ we had chosen $F = 8$, we would calculate spaces at 8 and marks at 12 producing a required subpulse frequency of 96. At low frame rates, this is a non-issue since the transition time of the LED is sufficiently fast [181]. However, it is still inefficient and will require processing overhead for the transmitter. Thus, to construct the needed frequencies from sub-pulses, we choose sub-pulse duration, τ, as

$$\tau = \frac{(\alpha F) \times (\alpha + 0.5)F}{\gcd(\alpha F, (\alpha + 0.5)F)} \tag{F.3}$$

based on the Nyquist criterion that we sample at least twice the maximum frequency in the signal. Modulating at baseband, this would mean we are constrained to frequencies less than half the frame rate. Since the end state of undersampling is to generate an alias at baseband, the available spectral bandwidth on either side of the carrier frequency, αF, is $F/2$. Figure F.2 illustrates the effects of undersampling. If a tone is sampled at a sampling frequency, F_S, at the same frequency reconstruction of the signal from samples would produce a straight line with zero frequency. It can also be seen that if the sampling frequency was a divisor of the frequency, the samples would be spaced out, but a zero frequency would still result. Envision only every other sample diamond in Figure F.2, or every thirtieth, and the resultant samples still produce a flat line. This result enables us to modulate the source LED fast enough to avoid perceptible flicker and still use a commodity CMOS sensor in an OCC set up to recover data based on frequency.

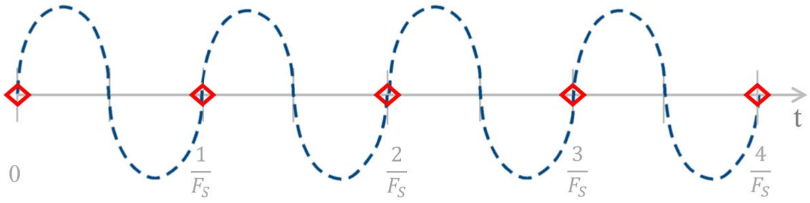

Figure F.2. Sampling at multiples of frequency gives a flat line with no frequency.

This result can also be calculated analytically by applying the discrete Fourier transform (DFT). The complex quantity W_N, appearing in the DFT analysis equation[6] which converts discrete time samples to radial frequency

$$X[k] = \sum_{n=0}^{N-1} x[n] W_N^{-kn} \tag{F.4}$$

is defined as

$$W_N = e^{-j(2\pi/N)} \tag{F.5}$$

and the complex exponential term repeats whenever the exponential is raised to an integer multiple of 2π.

The remaining challenge with using a relatively low frame rate is minimizing the frames — i.e. samples — we need to collect to determine frequency. Ideal, just two adjacent symbols would suffice. If we have any two points that are both the same, we could extrapolate a straight line and detect a zero frequency. There are several challenges with such an over-simplistic approach. The probability that two continuous random values are exactly identical is zero. Testing whether longer runs of samples, a more reliable threshold of sameness can be determined to establish robustness to noise at the expense of throughput.

---

[6] This term also occurs in the DFT synthesis equation, $x[n] = \frac{1}{N}\sum_{n=0}^{N-1} X[k] W_N^{-kn}$ moving from frequency to discrete time, but is not needed in this analysis.

In our simplified model of sampling in Figure F.2 we also implied impulse sampling at very precise moments in time. The CMOS sensor is actually summing energy from photons received over a period of time. The photodetector is an integrator over its sampling window, and not capturing a precise sample point. With a frame rate of 60 FPS, the exposure time is 16.67 ms. All that can be measured with the camera is the total energy arriving in that 16.67 ms. Employing undersampling at the receiver, the source is pulsing several times during that 16.67 ms window. The fewer pulses that are sent, the more likely it is that clock misalignment will smear energy between symbols. Assuming the clock at the transmitter and receiver are synchronized, the integration over sample periods should produce significantly varied values, allowing two samples to be used to gauge whether the transmitted frequency was aligned to a harmonic multiple or offset.

Arriving pulses that would feed the integration in the sensor are illustrated in Figure F.3. For a zero, in the top row, there are always an equal number of light and dark pulses. For a one, there is a one-third/two-thirds split providing a clear distinction between Sample 1 and Sample 2 allowing a frequency to be detected.

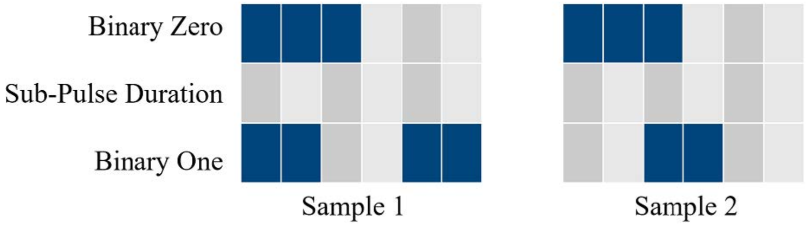

Figure F.3. Sample windows capture the same net value for zero frequency and varied values indicating an undersampled frequency.

If phase drift occurs, zeros will remain zeros, but as the sub-pulse in a one begins to wrap around, the difference between them will compress, making the thresholding decision between one and zero more difficult. If timing is off by a full sub-pulse duration, a zero and a one would become indistinguishable in Figure F.3. Clock synchronization is also required in longer messages to ensure the two samples being compared were a transmission pair. Otherwise, misaligned sample windows with transitions between zeros and ones would cause complete ambiguity with all comparisons being off by a factor of one sub-pulse duration.

Despite the potential challenges with timing, if background noise is relatively constant across sampling intervals, this frequency detection approach is more robust in a high noise environment since we are measuring change between sample intervals and not intensity directly. If the noise becomes so high we cannot differentiate zero and one samples — due to quantization noise, overflow, or some other limiting factor — the system will no longer be able to transmit data.

Binary Channel Probabilities with USFOOK

Assuming USFOOK with the zero and one frequencies as defined in Equations F.2 and F.1, we saw in Figure F.3 that the received signal power will either be 50% of the maximum transmit power of the light or vary between 1/3 and 2/3 of the maximum transmit power in adjacent frames. Specific frame rates are selected so that across any two adjacent samples, the overall PWM strength observe is 50% of the maximum transmit power and the signal is undetectable to human observers. Implementing such a system, knowing that an effective 50% PWM would always be enforced, the instantaneous maximum output power of the fixture could be increased allowing the overall implementation to achieve the required illumination characteristics.

The detector must make a determination if two adjacent receive values in the presence of noise are the same or have varied. For this to work the signal must not saturate the camera quantizer and we must have sufficient dynamic range after quantization to recover the data. If signal and variation compress into one quantization step, the more amplitude variance received through aliasing during camera sampling will be lost.

Beginning our probabilistic channel analysis in a discrete form, we enumerate the likelihood of outputs detected based on the channel input. We initially assume discrete uniform noise with a variation in the daylight amplitude that either zero or ±1 block of the peak received signal power, so the error set, E, is

$$E_i = \{-1, 0, 1\} \tag{F.6}$$

and equal probabilities for each member of the error set.

In the case where two adjacent symbols are equal, we receive a zero. In the case a higher symbol and then a lower symbol are observed, we receive a one. In the case that a low and then high symbol are received, we know we know there has been interference in the channel, but, having constrained the values in error set, we know this output can only occur if the input is a zero. Thus, for a zero sent in this binary channel the probability it is correctly received is

$$\mathrm{P}(0_{Rx}|0_{Tx}) = \mathrm{P}(E_1 = -1) + \mathrm{P}(E_1 = 0) \cdot \mathrm{P}(E_2 = -1^c) + \mathrm{P}(E_1 = 1) \cdot \mathrm{P}(E_2 = 1) \tag{F.7}$$

and the probability a one is errantly received is

$$\mathrm{P}(1_{Rx}|0_{Tx}) = \mathrm{P}(E_1 = 0) \cdot \mathrm{P}(E_2 = -1) + \mathrm{P}(E_1 = 1) \cdot \mathrm{P}(E_2 = 1^c). \tag{F.8}$$

Assuming equal probabilities the set of possible errors in Equation F.6, Equation F.7 becomes $3/9 + 2/9 + 1/9 = 2/3$ and Equation F.8 is $1/9 + 2/9 = 1/3$. These sum to one, with probability favoring that a zero is received if a zero is sent as expected, but still illustrating the clear impact of noise in the channel.

Conversely, in the case a one is sent, the bounds of ±1 in the error set mean the only way to generate an error is if the first symbol is attenuated and the second signal is boosted by the noise. Thus the probability of error given a one is sent is

$$\mathrm{P}(0_{Rx}|1_{Rx}) = \mathrm{P}(E_1 = -1) \cdot \mathrm{P}(E_2 = 1) \tag{F.9}$$

which results in a probability of $1/9$. Leveraging the law of total probability without enumeration we note $\mathrm{P}(1_{Rx}|1_{Tx}) = 8/9$. Detecting variation is more robust than simply assessing sameness in the presence of noise.

Uniform noise in discrete blocks, as presented captured in Equation F.6 is a slight oversimplification of the noise we expect in the system, but — as seen in this dissertation — quantization noise plays a huge role in overall noise using commodity cameras. Adjusting the from a uniform distribution across the error to using the shape of a cosine from $-\pi/2$ to $\pi/2$ as the PDF, the quantized error probabilities would become $\mathrm{P}(E_{-1}) = 0.25$, $\mathrm{P}(E_0) = 0.5$, and $\mathrm{P}(E_1) = 0.25$. Then, reworking Equation F.7

$$\mathrm{P}(0_{Rx}|0_{Tx}) = \mathrm{P}(E_1 = -1) + \mathrm{P}(E_1 = 0) \cdot \mathrm{P}(E_2 = -1^c) + \mathrm{P}(E_1 = 1) \cdot \mathrm{P}(E_2 = 1) \tag{F.10}$$

giving an probability of $1/4 + 3/8 + 1/16 = 11/16$ which is a marginal improvement over the result in F.7 since there is less variance in the noise. Similar, the $\mathrm{P}(1_{Rx}|1_{Tx})$ increases from 8/9 to 15/16. While using far less dynamic range than convention OOK, dark to full brightness, with slightly more SNR to compensate for the reduced detection delta, USFOOK can still reasonably deliver bits of information while simultaneously avoiding any perceptible flicker issues.

List of References

[1] T. Nguyen, A. Islam, and Y. M. Jang, "Region-of-Interest Signaling Vehicular System Using Optical Camera Communications," *IEEE Photonics Journal*, vol. 9, no. 1, pp. 1–20, Feb. 2017. Available: https://doi.org/10.1109/JPHOT.2016.2644960

[2] N. Okasha, A. Zekry, and F. Newagy, "Car To Car Communication Using RF Cognitive Radio with VLC Common Control Channel," In Review, preprint, July 2023. Available: https://doi.org/10.21203/rs.3.rs-3196449/v1

[3] M. Plattner and G. Ostermayer, "A camera-based vehicular visible light communication system using modulated taillights in public road scenarios," *Vehicular Communications*, p. 100651, July 2023. Available: https://doi.org/10.1016/j.vehcom.2023.100651

[4] M. Plattner and G. Ostermayer, "Camera-based Vehicle-to-Vehicle Visible Light Communication - A Software-Only Solution for Vehicle Manufacturers Camera-based Vehicle-to-Vehicle Visible Light Communication - A Software-Only Solution for Vehicle Manufacturers," in *2023 32nd International Conference on Computer Communications and Networks (ICCCN)*. Honolulu, HI, USA: IEEE, July 2023, pp. 1–7. Available: https://doi.org/10.1109/ICCCN58024.2023.10230125

[5] National Highway Traffic Safety Administration, "Federal Motor Vehicle Safety Standards; V2V Communications," Rep., Jan. 2017. Available: https://www.federalregister.gov/documents/2017/01/12/2016-31059/federal-motor-vehicle-safety-standards-v2v-communications

[6] World Health Organization, *Global status report on road safety 2018*. Geneva: World Health Organization, 2018. Available: https://apps.who.int/iris/handle/10665/276462

[7] L. Figueiredo, I. Jesus, J. Machado, J. Ferreira, and J. Martins de Carvalho, "Towards the development of intelligent transportation systems," in *ITSC 2001. 2001 IEEE Intelligent Transportation Systems. Proceedings (Cat. No.01TH8585)*. Oakland, CA, USA: IEEE, 2001, pp. 1206–1211. Available: https://doi.org/10.1109/ITSC.2001.948835

[8] U.S. Department of Transportation, "Intelligent Transportation Systems - ITS in Use Today," 2022. Available: https://www.its.dot.gov/resources/fastfacts.htm

[9] D. Jiang and L. Delgrossi, “IEEE 802.11p: Towards an International Standard for Wireless Access in Vehicular Environments,” in *VTC Spring 2008 - IEEE Vehicular Technology Conference*. Marina Bay, Singapore: IEEE, May 2008, pp. 2036–2040. ISSN: 1550-2252. Available: https://doi.org/10.1109/VETECS.2008.458

[10] “IEEE Standard for Information technology– Local and metropolitan area networks– Specific requirements– Part 11: Wireless LAN Medium Access Control (MAC) and Physical Layer (PHY) Specifications Amendment 6: Wireless Access in Vehicular Environments,” *IEEE Std 802.11p-2010 (Amendment to IEEE Std 802.11-2007 as amended by IEEE Std 802.11k-2008, IEEE Std 802.11r-2008, IEEE Std 802.11y-2008, IEEE Std 802.11n-2009, and IEEE Std 802.11w-2009)*, pp. 1–51, 2010. Available: https://doi.org/10.1109/IEEESTD.2010.5514475

[11] X. Lu, S. E. Shladover, A. Kalias, and O. D. Altan, “Messages for Cooperative Adaptive Cruise Control Using V2V Communication in Real Traffic,” in *Vehicle-to-Vehicle and Vehicle-to-Infrastructure Communications: A Technical Approach*, F. Hu, Ed. CRC Press, Feb. 2018, pp. 167–171. Available: https://doi.org/10.1201/9781315201542

[12] S. Routray, A. Suman, P. Suman, S. Padhy, P. Chatterjee, and S. Shetty, “Vehicular Safety Revolution: A Cutting-Edge Communication Paradigm for Accident Prevention,” in *Proceedings of the Twenty-fourth International Symposium on Theory, Algorithmic Foundations, and Protocol Design for Mobile Networks and Mobile Computing*. Washington, DC, USA: ACM, Oct. 2023, pp. 406–411. Available: https://doi.org/10.1145/3565287.3623389

[13] E. Dahlman, S. Parkvall, and J. Skold, *5G NR: The Next Generation Wireless Access Technology*. San Diego, CA, USA: Elsevier Science & Technology, 2020. Publication Title: 5G NR.

[14] J. Tan and L. Dai, “THz Precoding for 6G: Challenges, Solutions, and Opportunities,” *IEEE Wireless Communications*, vol. 30, no. 4, pp. 132–138, Aug. 2023. Available: https://doi.org/10.1109/MWC.015.2100674

[15] K. G. Rallis *et al.*, “Energy Efficient Cooperative Communications in Aggregated VLC/RF Networks with NOMA,” *IEEE Transactions on Communications*, pp. 1–1, 2023. Available: https://doi.org/10.1109/TCOMM.2023.3292486

[16] H. Sun, C. Wang, Z. Liao, and T. Chen, “A Supermartingale Theory-Based Random Compensation Algorithm for Visible Light Communication/Radio Frequency Hybrid Networks,” *IEEE Access*, vol. 11, pp. 82 192–82 198, 2023. Available: https://doi.org/10.1109/ACCESS.2023.3301154

[17] Y. Tong *et al.*, “Channel Characteristics and Link Adaption for Visible Light Communication in an Industrial Scenario,” *Sensors*, vol. 23, no. 7, p. 3442, Mar. 2023. Available: https://doi.org/10.3390/s23073442

[18] J. Zheng, T. Yamazato, and K. Naito, “A Testbed to Integrate Private 5G Networks with Visible Light Communication for Service Area Expansion,” in *2023 IEEE Symposium on Computers and Communications (ISCC)*. Gammarth, Tunisia: IEEE, July 2023, pp. 1–5. Available: https://doi.org/10.1109/ISCC58397.2023.10218188

[19] “IEEE Standard for Local and metropolitan area networks–Part 15.7: Short-Range Optical Wireless Communications,” Rep., 2018. ISBN: 9781504454315. Available: https://doi.org/10.1109/IEEESTD.2019.8697198

[20] T. Nawaz, M. Seminara, S. Caputo, L. Mucchi, F. Cataliotti, and J. Catani, “IEEE 802.15.7-Compliant Ultra-low Latency Relaying VLC System for Safety-Critical ITS,” June 2019. arXiv:1906.08773 [eess]. Available: http://arxiv.org/abs/1906.08773

[21] Y. Tanaka, S. Haruyama, and M. Nakagawa, “Wireless optical transmissions with white colored LED for wireless home links,” in *11th IEEE International Symposium on Personal Indoor and Mobile Radio Communications. PIMRC 2000. Proceedings (Cat. No.00TH8525)*. London, UK: IEEE, 2000, vol. 2, pp. 1325–1329. Available: https://doi.org/10.1109/PIMRC.2000.881634

[22] “IEEE Approved Draft Standard for Information Technology–Telecommunications and Information Exchange Between Systems Local and Metropolitan Area Networks–Specific Requirements - Part 11: Wireless LAN Medium Access Control (MAC) and Physical Layer (PHY) Specifications Amendment 7: Light Communications,” *IEEE P802.11bb/D7.0, March 2023*, pp. 1–29, Mar. 2023.

[23] S. Dimitrov and H. Haas, *Principles of LED Light Communications: Towards Networked Li-Fi*. Cambridge, UK: Cambridge University Press, 2015.

[24] P. A. Loureiro, F. P. Guiomar, and P. P. Monteiro, “Visible Light Communications: A Survey on Recent High-Capacity Demonstrations and Digital Modulation Techniques,” *Photonics*, vol. 10, no. 9, p. 993, Aug. 2023. Available: https://doi.org/10.3390/photonics10090993

[25] Federal Communications Commission Office of Engineering and Technology Policy and Rules Division, “FCC Online Table of Frequency Allocations 47 C.F.R. \S 2.106,” Feb. 2021. Available: https://transition.fcc.gov/oet/spectrum/table/fcctable.pdf

[26] R. Deng, J. He, M. Chen, and Y. Zhou, “Experimental Demonstration of a Real-Time gigabit OFDM-VLC System with a Cost-efficient Precoding Scheme,” *Optics Communications*, vol. 423, pp. 69–73, Sep. 2018. Available: https://doi.org/10.1016/j.optcom.2018.04.009

[27] Z. Wang, Q. Wang, W. Huang, Z. Xu, IEEE Xplore, and Wiley, *Visible Light Communications: Modulation and Signal Processing*. Hoboken: Wiley, 2017. Available: https://doi.org/10.1002/9781119331865

[28] A. M. Căilean and M. Dimian, “Current Challenges for Visible Light Communications Usage in Vehicle Applications: A Survey,” *IEEE Communications Surveys & Tutorials*, vol. 19, no. 4, pp. 2681–2703, 2017. Available: https://doi.org/10.1109/COMST.2017.2706940

[29] C. E. Shannon, “A mathematical theory of communication,” *Bell System Technical Journal*, vol. 27, no. 4, pp. 623–656, 1948.

[30] R. Huang and T. Yamazato, “A Review on Image Sensor Communication and Its Applications to Vehicles,” *Photonics*, vol. 10, no. 6, p. 617, May 2023. Available: https://doi.org/10.3390/photonics10060617

[31] W. Shen and H. Tsai, “Testing vehicle-to-vehicle visible light communications in real-world driving scenarios,” in *2017 IEEE Vehicular Networking Conference (VNC)*, Nov. 2017, pp. 187–194. ISSN: 2157-9865. Available: https://doi.org/10.1109/VNC.2017.8275596

[32] L. E. M. Matheus, A. B. Vieira, L. F. M. Vieira, M. A. M. Vieira, and O. Gnawali, “Visible Light Communication: Concepts, Applications and Challenges,” *IEEE Communications Surveys & Tutorials*, vol. 21, no. 4, pp. 3204–3237, 2019. Available: https://doi.org/10.1109/COMST.2019.2913348

[33] E. El-Mokadem, N. Tawfik, M. H. Aly, and W. El-Deeb, “Design and performance evaluation of vehicular visible light communication system under different weather conditions and system parameters,” *Opto-Electronics Review*, Apr. 2023. Available: https://doi.org/10.24425/opelre.2023.145580

[34] E. Eso, S. Teli, N. Bani Hassan, S. Vitek, Z. Ghassemlooy, and S. Zvanovec, “400 m rolling-shutter-based optical camera communications link,” *Optics Letters*, vol. 45, no. 5, p. 1059, Mar. 2020. Available: https://doi.org/10.1364/OL.385423

[35] C. Shannon, “Communication In The Presence Of Noise,” *Proceedings of the IEEE*, vol. 86, no. 2, pp. 447–457, Feb. 1998. Available: https://doi.org/10.1109/JPROC.1998.659497

[36] A. Costanzo, V. Loscri, and M. Biagi, “A Noise Mitigation Approach for VLC Systems,” in *2019 Global LIFI Congress (GLC)*, June 2019, pp. 1–5. Available: https://doi.org/10.1109/GLC.2019.8864127

[37] M. S. Islim *et al.*, “The Impact of Solar Irradiance on Visible Light Communications,” *Journal of Lightwave Technology*, vol. 36, no. 12, pp. 2376–2386, June 2018. Conference Name: Journal of Lightwave Technology. Available: https://doi.org/10.1109/JLT.2018.2813396

[38] E. Eso, Z. Ghassemlooy, S. Zvanovec, J. Sathian, and A. Gholami, “Fundamental Analysis of Vehicular Light Communications and the Mitigation of Sunlight Noise,” *IEEE Transactions on Vehicular Technology*, vol. 70, no. 6, pp. 5932–5943, June 2021. Conference Name: IEEE Transactions on Vehicular Technology. Available: https://doi.org/10.1109/TVT.2021.3078576

[39] Polybius, *The Histories of Polybius*. England: Macmillan, 1889.

[40] “Text Tech: Can Navy Vessels Use Shipboard Signal Lamps for Text Messaging?” https://www.nre.navy.mil/media-center/news-releases/text-tech-can-navy-vessels-use-shipboard-signal-lamps-text-messaging (accessed Oct. 23, 2023).

[41] A. G. Bell, “ART. XXXIV. On the Production and Reproduction of Sound by Light: [Read before the American Association for the Advancement of Science, in Boston, August 27, 1880.] Researches of Sumner Tainter and Alexander Graham Bell. Photophonic Transmitters. Experiments to ascertain the nature of the rays that affect selenium. Non-Electric Photophonic Receivers,” *American Journal of Science (1880)*, vol. 20, no. 118, pp. 305–, 1880.

[42] Manned Spacecraft Center National Aeronautics and Space Administration, *Final Report - Laser Communication Transmitter.* Camden, NJ, USA: Applied Research Defense Electronic Products, Radio Corporation of America, 1965.

[43] M. Krishnaswamy, “Bringing light-speed internet to Sub-Saharan Africa,” X Company. Nov. 2020. Available: https://blog.x.company/bringing-light-speed-internet-to-sub-saharan-africa-4e022e1154ca

[44] Y. Shimizu, K. Sakano, Y. Noguchi, and T. Moriguchi, “Light emitting device having a nitride compound semiconductor and a phosphor containing a garnet fluorescent material,” U.S. Patent 5 998 925, Dec., 1999. Available: https://patentimages.storage.googleapis.com/48/0d/42/543c717c21c473/US5998925.pdf

[45] J. Grubor, S. C. J. Lee, K.-D. Langer, T. Koonen, and J. W. Walewski, “Wireless High-Speed Data Transmission with Phosphorescent White-Light LEDs,” in *33rd*

European Conference and Exhibition of Optical Communication - Post-Deadline Papers (published 2008), Sep. 2007, pp. 1–2.

[46] D. Barber, C. Pickle, and Z. White, “Impacts on Multi-pulse Pulse Position Modulation Visible Light Communication from Outdoor Daylight Conditions,” *Proceedings of the 56th Hawaii International Conference on System Sciences*, pp. 6582–6590, Jan. 2023. Available: https://hdl.handle.net/10125/103430

[47] P. Sharda and M. R. Bhatnagar, “Vehicular Visible Light Communication System: Modeling and Visualizing Critical Outdoor Propagation Characteristics,” *IEEE Transactions on Vehicular Technology*, pp. 1–14, 2023. Available: https://doi.org/10.1109/TVT.2023.3282615

[48] Y. Kim and Y. Chung, “Experimental outdoor visible light data communication system using differential decision threshold with optical and color filters,” *Optical Engineering*, vol. 54, no. 4, p. 040501, Apr. 2015. Available: https://doi.org/10.1117/1.OE.54.4.040501

[49] P. Ji, H. Tsai, C. Wang, and F. Liu, “Vehicular Visible Light Communications with LED Taillight and Rolling Shutter Camera,” in *2014 IEEE 79th Vehicular Technology Conference (VTC Spring)*. IEEE, 2014, pp. 1–6. Available: https://doi.org/10.1109/VTCSpring.2014.7023142

[50] J. Lee, S. Kim, and S. Han, “Multi-level optical signal reception by blur curved approximation for optical camera communication,” in *2017 Opto-Electronics and Communications Conference (OECC) and Photonics Global Conference (PGC)*, July 2017, pp. 1–2. ISSN: 2166-8892. Available: https://doi.org/10.1109/OECC.2017.8114779

[51] Y. Goto *et al.*, “A New Automotive VLC System Using Optical Communication Image Sensor,” *IEEE Photonics Journal*, vol. 8, no. 3, pp. 1–17, June 2016. Available: https://doi.org/10.1109/JPHOT.2016.2555582

[52] Y. H. Chung and S. Oh, “Efficient optical filtering for outdoor visible light communications in the presence of sunlight or articifical light,” in *2013 International Symposium on Intelligent Signal Processing and Communication Systems*, Nov. 2013, pp. 749–752. Available: https://doi.org/10.1109/ISPACS.2013.6704649

[53] Y. Imai, T. Ebihara, K. Mizutani, and N. Wakatsuki, “Performance evaluation of high-speed visible light communication combining low-speed image sensor and polygon mirror in an outdoor environment,” in *2016 Eighth International Conference on Ubiquitous and Future Networks (ICUFN)*, July 2016, pp. 51–55. ISSN: 2165-8536. Available: https://doi.org/10.1109/ICUFN.2016.7536978

[54] R. Martinek, L. Danys, and R. Jaros, "Visible Light Communication System Based on Software Defined Radio: Performance Study of Intelligent Transportation and Indoor Applications," *Electronics*, vol. 8, no. 4, p. 433, Apr. 2019. Available: https://doi.org/10.3390/electronics8040433

[55] D. Kim, S. Yang, H. Kim, Y. Son, and S. Han, "Outdoor Visible Light Communication for inter- vehicle communication using Controller Area Network," in *2012 Fourth International Conference on Communications and Electronics (ICCE)*. Hue, Vietnam: IEEE, Aug. 2012, pp. 31–34. Available: https://doi.org/10.1109/CCE.2012.6315865

[56] R. Ghabboun, D. W. Dawoud, E. A. Shabab, and S. Ismail, "Adaptive Real-Time Speed Limit Broadcasting for Autonomous Driving applications Using Visible Light Communication," in *2023 IEEE International Conference on Electro Information Technology (eIT)*. Romeoville, IL, USA: IEEE, May 2023, pp. 191–196. Available: https://doi.org/10.1109/eIT57321.2023.10187303

[57] T. Yamazato *et al.*, "The Uplink Visible Light Communication Beacon System for Universal Traffic Management," *IEEE Access*, vol. 5, pp. 22 282–22 290, 2017. Conference Name: IEEE Access. Available: https://doi.org/10.1109/ACCESS.2017.2759179

[58] C. Beguni, A. M. Căilean, S. A. Avătămăniței, A. D. Potorac, E. Zadobrischi, and M. Dimian, "Increasing Vehicular Visible Light Communications Range Based on LED Current Overdriving and Variable Pulse Position Modulation: Concept and Experimental Validation," *Sensors*, vol. 23, no. 7, p. 3656, Mar. 2023. Available: https://doi.org/10.3390/s23073656

[59] S. Haruyama and T. Yamazato, "Image Sensor Based Visible Light Communication," in *Visible Light Communication*, S. Arnon, Ed. Cambridge, UK: Cambridge University Press, 2015, pp. 181–205.

[60] J. Yoo, J. Jang, J. K. Kwon, H. Kim, D. Song, and S. Jung, "Demonstration of vehicular visible light communication based on LED headlamp," *International journal of automotive technology*, vol. 17, no. 2, pp. 347–352, 2016. Available: https://doi.org/10.1007/s12239-016-0035-8

[61] C. Beguni, E. Zadobrischi, S. A. Avatamanitei, and A. M. Căilean, "Experimental Demonstration of a Visible Light Communications Crosswalk Assistance System," in *2022 International Symposium on Electronics and Telecommunications (ISETC)*. Timisoara, Romania: IEEE, Nov. 2022, pp. 1–4. Available: https://doi.org/10.1109/ISETC56213.2022.10009985

[62] T. Saito, S. Haruyama, and M. Nakagawa, "A New Tracking Method using Image Sensor and Photo Diode for Visible Light Road-to-Vehicle Communication," in *2008 10th International Conference on Advanced Communication Technology*, Feb. 2008, vol. 1, pp. 673–678. ISSN: 1738-9445. Available: https://doi.org/10.1109/ICACT.2008.4493850

[63] F. M. Alsalami *et al.*, "Average Channel Capacity Bounds of a Dynamic Vehicle-to-Vehicle Visible Light Communication System," *IEEE Transactions on Vehicular Technology*, pp. 1–11, 2023. Available: https://doi.org/10.1109/TVT.2023.3320889

[64] A. Căilean, B. Cagneau, L. Chassagne, M. Dimian, and V. Popa, "Novel Receiver Sensor for Visible Light Communications in Automotive Applications," *IEEE Sensors Journal*, vol. 15, no. 8, pp. 4632–4639, Aug. 2015. Available: https://doi.org/10.1109/JSEN.2015.2425473

[65] T. Yamazato *et al.*, "Image-sensor-based visible light communication for automotive applications," *IEEE Communications Magazine*, vol. 52, no. 7, pp. 88–97, July 2014. Available: https://doi.org/10.1109/MCOM.2014.6852088

[66] T. Huynh, T. Pham, and M. Yoo, "Detection Algorithm for Overlapping LEDs in Vehicular Visible Light Communication System," *IEEE Access*, vol. 7, pp. 109 945–109 955, 2019. Available: https://doi.org/10.1109/ACCESS.2019.2933863

[67] S. Okada, T. Yendo, T. Yamazato, T. Fujii, M. Tanimoto, and Y. Kimura, "On-vehicle receiver for distant visible light road-to-vehicle communication," in *2009 IEEE Intelligent Vehicles Symposium*, June 2009, pp. 1033–1038. ISSN: 1931-0587. Available: https://doi.org/10.1109/IVS.2009.5164423

[68] C. Chow, R. Shiu, Y. Liu, Y. Liu, and C. Yeh, "Non-flickering 100 m RGB visible light communication transmission based on a CMOS image sensor," *Optics Express*, vol. 26, no. 6, p. 7079, Mar. 2018. Available: https://doi.org/10.1364/OE.26.007079

[69] X. Wang, M. Zhang, and X. Ren, "Noise Mitigation Using Adaptive Filtering Algorithm for Long-Range VLC System Based on FPGA," in *2020 Asia Communications and Photonics Conference (ACP) and International Conference on Information Photonics and Optical Communications (IPOC)*, Oct. 2020, pp. 1–3.

[70] G. Li *et al.*, "Position-Dependent MIMO Demultiplexing Strategy for High-Speed Visible Light Communication in Internet of Vehicles," *IEEE Internet of Things Journal*, vol. 9, no. 13, pp. 10 833–10 850, July 2022. Available: https://doi.org/10.1109/JIOT.2021.3126798

[71] P. Chavez-Burbano *et al.*, “Optical camera communication system for Internet of Things based on organic light emitting diodes,” *Electronics Letters*, vol. 55, no. 6, pp. 334–336, Mar. 2019. Available: https://doi.org/10.1049/el.2018.8037

[72] M. A. Atta and A. Bermak, “A 160 m visible light communication link using hybrid undersampled phase-frequency shift on-off keying and CMOS image sensor,” *Optics Express*, vol. 27, no. 3, p. 2478, Feb. 2019. Available: https://doi.org/10.1364/OE.27.002478

[73] V. Matus, V. Guerra, S. Zvanovec, J. Rabadan, and R. Perez-Jimenez, “Sandstorm effect on experimental optical camera communication,” *Applied Optics*, vol. 60, no. 1, p. 75, Jan. 2021. Available: https://doi.org/10.1364/AO.405952

[74] P. Chavez-Burbano, V. Guerra, J. Rabadan, and R. Perez-Jimenez, “Optical camera communication for smart cities,” in *2017 IEEE/CIC International Conference on Communications in China (ICCC Workshops)*, Oct. 2017, pp. 1–4. ISSN: 2474-9133. Available: https://doi.org/10.1109/ICCChinaW.2017.8355271

[75] D. Barber, C. Pickle, C. Nelson, O. Walker, and J. McEachen, “550 m low-power outdoor visible light communication system using polarized light,” in *ODS 2023: Industrial Optical Devices and Systems*, R. Katayama and Y. Takashima, Eds. San Diego, CA, USA: SPIE, Oct. 2023, p. 21. Available: https://doi.org/10.1117/12.2676177

[76] P. Zhang *et al.*, “Constraints and Recent Solutions of Optical Camera Communication for Practical Applications,” *Photonics*, vol. 10, no. 6, p. 608, May 2023. Available: https://doi.org/10.3390/photonics10060608

[77] H. Zhu, T. Pu, W. Mou, and P. Chen, “Analysis of beat noise in optical stealth transmission system,” *Optics communications*, vol. 501, 2021. Publisher: Elsevier B.V.

[78] Innovative Automation Inc. “Exploring New Lighting Trends in Automotive Manufacturing, 2022.” Oct. 2019. Available: https://www.innovativeautomation.com/lighting-trends-automotive-manufacturing

[79] The Franklin Institute, “Hidden Power: Light Bulb Efficiency.” University Park, PA, USA, 2018. Available: https://www.mrsec.psu.edu/content/light-bulb-efficiency

[80] J. Kanter, “Europe’s Ban on Old-Style Bulbs Begins,” *New York Times*, Sep. 2009. Available: https://www.nytimes.com/2009/09/01/business/energy-environment/01iht-bulb.html

[81] Department of Energy, “Biden Administration Implements New Cost-Saving Energy Efficiency Standards for Light Bulbs,” U.S. Department of Energy, Rep., Apr. 2022. Available: https://www.energy.gov/articles/biden-administration-implements-new-cost-saving-energy-efficiency-standards-light-bulbs

[82] Z. Ghassemlooy, L. N. Alves, S. Zvánovec, and M.-A. Khalighi, Eds., *Visible light communications: theory and applications*. Boca Raton London New York: CRC Press, Talyor & Francis Group, 2017.

[83] J. Herman, “Ultimate Light Bulb Test: Incandescent vs. Compact Fluorescent vs. LED,” Popular Mechanics, Sep. 2011. https://www.popularmechanics.com/technology/gadgets/reviews/g164/incandescent-vs-compact-fluorescent-vs-led-ultimate-light-bulb-test/ (accessed: May 5, 2016).

[84] Z. Ghassemlooy, W. Popoola, and S. Rajbhandari, *Optical Wireless Communications: System and Channel Modelling with MATLAB®, Second Edition*. Milton, FL, USA: CRC Press, 2019.

[85] C. Danakis, M. Afgani, G. Povey, I. Underwood, and H. Haas, “Using a CMOS camera sensor for visible light communication,” in *2012 IEEE Globecom Workshops*. IEEE, 2012, pp. 1244–1248. ISSN: 2166-0077.

[86] B. Sklar, *Digital communications: fundamentals and applications*, 2nd ed. Upper Saddle River, NJ, USA: Prentice-Hall PTR, 2001.

[87] K. Cui, G. Chen, Z. Xu, and R. D. Roberts, “Traffic light to vehicle visible light communication channel characterization,” *Applied Optics*, vol. 51, no. 27, p. 6594, Sep. 2012. Available: https://doi.org/10.1364/AO.51.006594

[88] H. Qin, J. Liang, and X. Ke, “Vehicular visible light communications noise analysis and modeling,” *Applied Optics*, vol. 62, no. 16, p. 4134, June 2023. Available: https://doi.org/10.1364/AO.485784

[89] M. Conforti, A. Marini, T. X. Tran, D. Faccio, and F. Biancalana, “Interaction between optical fields and their conjugates in nonlinear media,” *Optics Express*, vol. 21, no. 25, p. 31239, Dec. 2013. Available: https://doi.org/10.1364/OE.21.031239

[90] S. Q. Duntley, “The Reduction of Apparent Contrast by the Atmosphere,” *Journal of the Optical Society of America*, vol. 38, no. 2, p. 179, Feb. 1948. Available: https://doi.org/10.1364/JOSA.38.000179

[91] R. E. Walker, *Marine light field statistics* (Wiley series in pure and applied optics). New York, NY, USA: Wiley, 1994.

[92] R. Barrios and F. Dios, “Wireless Optical Communication Through the Turbulent Atmosphere: A Review,” in *Optical Communications Systems*, N. Das, Ed. InTech, Mar. 2012. Available: https://doi.org/10.5772/1807

[93] C. Jellen, J. Burkhardt, C. Brownell, and C. Nelson, “Machine learning informed predictor importance measures of environmental parameters in maritime optical turbulence,” *Applied Optics*, vol. 59, no. 21, pp. 6379–6389, July 2020. Available: https://doi.org/10.1364/AO.397325

[94] A. Khizhnyak and V. Markov, “Beaconless operation for optimal laser beam propagation through turbulent atmosphere,” A. M. J. van Eijk, C. C. Davis, and S. M. Hammel, Eds., San Diego, CA, USA, Sep. 2016, p. 997904. Available: https://doi.org/10.1117/12.2237453

[95] Y. Yitzhaky, I. Dror, and N. Kopleika, “Restoration of atmospherically blurred images according to weather-predicted atmospheric modulation transfer functions,” *Optical Engineering*, vol. 36, no. 11, p. 3064, Nov. 1997. Available: https://doi.org/10.1117/1.601526

[96] P. Luo, H. Tsai, Z. Ghassemlooy, W. Viriyasitavat, H. L. Minh, and X. Tang, “Car-to-Car Visible Light Communications,” in *Visible Light Communications: Theory and Applications*, Z. Ghassemlooy, L. N. Alves, S. Zvánovec, and M. Khalighi, Eds., 1st ed. CRC Press, June 2017, pp. 253–282. Available: https://doi.org/10.1201/9781315367330

[97] Z. Ghassemlooy, M. Khalighi, and D. Wu, “Channel Modeling,” in *Visible Light Communications: Theory and Applications*, Z. Ghassemlooy, L. N. Alves, S. Zvánovec, and M. A. Khalighi, Eds., 1st ed. CRC Press, June 2017, pp. 71–96. Available: https://doi.org/10.1201/9781315367330

[98] L. C. Andrews, R. L. Phillips, and C. Y. Hopen, *Laser beam scintillation with applications*. Bellingham, WA, USA: SPIE Press, 2001.

[99] R. J. Sasiela, *Electromagnetic wave propagation in turbulence: evaluation and application of Mellin transforms*, 2nd ed. Bellingham, WA, USA: SPIE, 2007.

[100] D. A. LeMaster *et al.*, “Differential tilt variance effects of turbulence in imagery: comparing simulation with theory,” E. J. Kelmelis, Ed., Baltimore, MD, USA, May 2016, p. 984606. Available: https://doi.org/10.1117/12.2223470

[101] M. R. Whiteley, D. C. Washburn, and L. A. Wright, “Differential-tilt technique for saturation-resistant profiling of atmospheric turbulence,” R. K. Tyson, D. Bonaccini, and M. C. Roggemann, Eds., San Diego, CA, USA, Feb. 2002, pp. 221–232. Available: https://doi.org/10.1117/12.454795

[102] D. H. Nelson *et al.*, “Huygens-Fresnel wave-optics simulation of atmospheric optical turbulence and reflective speckle in CO2 differential absorption LIDAR (DIAL),” Mar. 1999, p. 14.

[103] E. Eso, O. I. Younus, Z. Ghassemlooy, S. Zvanovec, and M. M. Abadi, “Performances of Optical Camera-based Vehicular Communications under Turbulence Conditions,” in *2020 12th International Symposium on Communication Systems, Networks and Digital Signal Processing (CSNDSP)*. Porto, Portugal: IEEE, July 2020, pp. 1–5. Available: https://doi.org/10.1109/CSNDSP49049.2020.9249598

[104] S. Peters, “Physics of Space and Airborne Sensor Systems,” Monterey, CA, USA, Apr. 2022.

[105] J. Vicent Servera *et al.*, “Systematic Assessment of MODTRAN Emulators for Atmospheric Correction,” *IEEE Transactions on Geoscience and Remote Sensing*, vol. 60, pp. 1–17, 2022. Available: https://doi.org/10.1109/TGRS.2021.3071376

[106] M. Utrillas, J. Boscá, J. Martínez-Lozano, J. Cañada, F. Tena, and J. Pinazo, “A comparative study of SPCTRAL2 and SMARTS2 parameterised models based on spectral irradiance measurements at Valencia, Spain,” *Solar Energy*, vol. 63, no. 3, pp. 161–171, Sep. 1998. Available: https://doi.org/10.1016/S0038-092X(98)00058-9

[107] K. Cui, G. Chen, Z. Xu, and R. D. Roberts, “Experimental characterization of traffic light to vehicle VLC link performance,” in *2011 IEEE GLOBECOM Workshops (GC Wkshps)*. Houston, TX, USA: IEEE, Dec. 2011, pp. 808–812. Available: https://doi.org/10.1109/GLOCOMW.2011.6162566

[108] A. Moreira, R. Valadas, and A. de Oliveira Duarte, “Characterisation and modelling of artificial light interference in optical wireless communication systems,” in *Proceedings of 6th International Symposium on Personal, Indoor and Mobile Radio Communications*. Toronto, Canada: IEEE, 1995, vol. 1, pp. 326–331. Available: https://doi.org/10.1109/PIMRC.1995.476907

[109] G. W. Kattawar and G. N. Plass, “Asymptotic radiance and polarization in optically thick media: ocean and clouds,” *Applied Optics*, vol. 15, no. 12, pp. 3166–3178, Dec. 1976. Available: https://doi.org/10.1364/AO.15.003166

[110] C. S. Williams and O. A. Becklund, *Optics: a short course for engineers and scientists* (Wiley series in pure and applied optics). New York: Wiley-Interscience, 1972.

[111] R. B. Gibbons and C. Moulton, “Enhanced Night Visibility Series, Volume XVII: Phases II and III—Characterization of Experimental Vision Enhancement Systems,” Virginia Tech Transportation Institute, Blacksburg, VA, USA, Rep. FHWA-

HRT-04-148, Dec. 2005. Available: https://www.fhwa.dot.gov/publications/research/safety/humanfac/04148/04148.pdf

[112] H. C. Andrews and B. R. Hunt, *Digital image restoration* (Prentice-Hall signal processing series). Englewood Cliffs, N.J: Prentice-Hall, 1977.

[113] W. B. Davenport and W. L. Root, *An introduction to the theory of random signals and noise*. New York: IEEE Press, 1987.

[114] S. L. Miller and D. G. Childers, *Probability and random processes: with applications to signal processing and communications*. Amsterdam ; Boston: Elsevier Academic Press, 2004.

[115] M. Yaseen, A. E. Canbilen, and S. Ikki, "Channel Estimation in Visible Light Communication Systems: The Effect of Input Signal-Dependent Noise," *IEEE Transactions on Vehicular Technology*, pp. 1–11, 2023. Available: https://doi.org/10.1109/TVT.2023.3282779

[116] C. W. Therrien and M. Tummala, *Probability and random processes for electrical and computer engineers*, 2nd ed. Boca Raton, FL, USA: CRC Press, 2012.

[117] Z. Lyu, T. Goossens, B. A. Wandell, and J. Farrell, "Validation of Physics-Based Image Systems Simulation With 3-D Scenes," *IEEE Sensors Journal*, vol. 22, no. 20, pp. 19 400–19 410, Oct. 2022. Available: https://doi.org/10.1109/JSEN.2022.3199699

[118] D. Kronstein, "Chronos 1.4 Datasheet," Aug. 2021. Available: https://www.krontech.ca/wp-content/uploads/2021/09/FM-ENGR-50001-Chronos-1.4-Datasheet-Rev5.pdf

[119] J. C. Russ, *The image processing handbook*. Boca Raton, FL, USA: CRC Press, 1992.

[120] X. Lu *et al.*, "Red InGaN Micro-LEDs on Silicon Substrates: Potential for Multicolor Display and Wavelength Division Multiplexing Visible Light Communication," *Journal of Lightwave Technology*, pp. 1–13, 2023. Available: https://doi.org/10.1109/JLT.2023.3261875

[121] Apple Inc, "iPhone 14 Pro and 14 Pro Max - Technical Specifications." https://www.apple.com/iphone-14-pro/specs/ (accessed Feb. 8, 2023).

[122] "Google maps." Imagery ©2023 AMBAG, Airbus, Data CSUMB SFML, CA OPC, Maxar Technologies, USA/FPAC/GEO. https://www.google.com/maps/place/Naval+Postgraduate+School/@36.6103149,-121.8889425,4460m/ (accessed Sep. 27, 2023).

[123] “Pixel phone hardware tech specs - Pixel Phone Help.” https://support.google.com/pixelphone/answer/7158570 (accessed July 5, 2023).

[124] Google Support, “Pixel Phone Help,” private communication, July 2023.

[125] T. Yamazato *et al.*, “Vehicle Motion and Pixel Illumination Modeling for Image Sensor Based Visible Light Communication,” *IEEE journal on selected areas in communications*, vol. 33, no. 9, pp. 1793–1805, 2015.

[126] D. Barber, V. Kanth, Z. White, and J. McEachen, “Spatial Frequency Detection of Optical Signals Embedded in the Environment,” in *2022 32nd International Telecommunication Networks and Applications Conference (ITNAC)*. Wellington, New Zealand: IEEE, Nov. 2022, pp. 185–191. Available: https://doi.org/10.1109/ITNAC55475.2022.9998410

[127] S. Vappangi, V. Venkata Mani, and M. Sellathurai, *Visible Light Communication: Comprehensive Theory and Applications with Matlab®*. Boca Raton, FL, USA: CRC Press, 2021.

[128] Z. White, “A Transmit Diversity Scheme for Multipulse-Pulse Position Modulated Visible Light Communications,” M.S. thesis, Naval Postgraduate School, Monterey, CA, USA, Sep. 2022.

[129] D. T. Nguyen and Y. Park, “Performance enhancement of optical camera communication system using optical camera communication coding and region-of-interest detection,” *IET Optoelectronics*, vol. 15, no. 6, pp. 255–263, Dec. 2021. Available: https://doi.org/10.1049/ote2.12041

[130] A. Ashok, M. Gruteser, N. Mandayam, J. Silva, M. Varga, and K. Dana, “Challenge: mobile optical networks through visual MIMO,” in *Proceedings of the sixteenth annual international conference on Mobile computing and networking - MobiCom ’10*. Chicago, Illinois, USA: ACM Press, 2010, p. 105. Available: https://doi.org/10.1145/1859995.1860008

[131] J. Kahn and J. Barry, “Wireless infrared communications,” *Proceedings of the IEEE*, vol. 85, no. 2, pp. 265–298, Feb. 1997. Available: https://doi.org/10.1109/5.554222

[132] D. H. Johnson and D. E. Dudgeon, *Array signal processing: concepts and techniques* (Prentice-Hall signal processing series). Englewood Cliffs, NJ: P T R Prentice Hall, 1993.

[133] K. Dong, X. Ke, and H. Li, “Camera-Based Channel Modeling and Symbol Error Rate Analysis of CSK Modulation for Outdoor OCC Systems,” *IEEE Access*, vol. 10, pp. 50 254–50 264, 2022. Available: https://doi.org/10.1109/ACCESS.2022.3173254

[134] H. L. Minh *et al.*, “100-Mb/s NRZ Visible Light Communications Using a Postequalized White LED,” *IEEE Photonics Technology Letters*, vol. 21, no. 15, pp. 1063–1065, Aug. 2009. Available: https://doi.org/10.1109/LPT.2009.2022413

[135] E. Rosenkrantz and S. Arnon, “Tunable electro-optic filter based on metal-ferroelectric nanocomposite for VLC,” *Optics Letters*, vol. 39, no. 16, p. 4954, Aug. 2014. Available: https://doi.org/10.1364/OL.39.004954

[136] H. Taguchi and M. Enokido, “Technology of color filter materials for image sensor,” p. 4, 2011. Available: http://www.imagesensors.org/PastWorkshops/2011Workshop/2011Papers/I01_Taguchi_ColorFilter.pdf

[137] A. Sevincer, A. Bhattarai, M. Bilgi, M. Yuksel, and N. Pala, “LIGHTNETs: Smart LIGHTing and Mobile Optical Wireless NETworks — A Survey,” *IEEE Communications Surveys & Tutorials*, vol. 15, no. 4, pp. 1620–1641, 2013. Available: https://doi.org/10.1109/SURV.2013.032713.00150

[138] J. Sung, C. Chow, and C. Yeh, “Is blue optical filter necessary in high speed phosphor-based white light LED visible light communications?” *Optics Express*, vol. 22, no. 17, p. 20646, Aug. 2014. Available: https://doi.org/10.1364/OE.22.020646

[139] D. R. Thompson *et al.*, “Retrieval of Atmospheric Parameters and Surface Reflectance from Visible and Shortwave Infrared Imaging Spectroscopy Data,” *Surveys in Geophysics*, vol. 40, no. 3, pp. 333–360, May 2019. Available: https://doi.org/10.1007/s10712-018-9488-9

[140] G. J. M. Forkel, A. Krohn, and P. A. Hoeher, “Optical Interference Suppression Based on LCD-Filtering,” *Applied Sciences*, vol. 9, no. 15, Jan. 2019. Place: Basel, Switzerland Publisher: MDPI AG. Available: https://doi.org/10.3390/app9153134

[141] R. L. Reese, *University physics*. Pacific Grove, CA, USA: Brooks/Cole Pub. Co, 2000.

[142] E. Venkatesulu, K. L. Buglione, N. J. Field, K. D. Doney, and J. A. Shaw, “Contrast enhancement through an air-water interface with polarization imaging,” in *Polarization Science and Remote Sensing XI*, F. Snik, M. K. Kupinski, and J. A. Shaw, Eds. San Diego, CA, USA: SPIE, Oct. 2023, p. 5. Available: https://doi.org/10.1117/12.2678059

[143] R. D. Roberts, “Space-time forward error correction for dimmable undersampled frequency shift ON-OFF keying camera communications (CamCom),” in *2013 Fifth International Conference on Ubiquitous and Future Networks (ICUFN)*. Da Nang, Vietnam: IEEE, July 2013, pp. 459–464. Available: https://doi.org/10.1109/ICUFN.2013.6614861

[144] N. Le, T. Le, T. Nguyen, and Y. M. Jang, “Synchronization issue for optical camera communications,” in *2015 Seventh International Conference on Ubiquitous and Future Networks*. Sapporo, Japan: IEEE, July 2015, pp. 220–224. Available: https://doi.org/10.1109/ICUFN.2015.7182537

[145] K. Dong, X. Ke, and M. Wang, “Equalization of camera-based channel to mitigate uncertain sampling for optical camera communications,” *Optics Express*, vol. 30, no. 26, p. 47776, Dec. 2022. Available: https://doi.org/10.1364/OE.474140

[146] S. B. Wicker, Ed., *Reed Solomon codes and their applications*. Piscataway, NJ, USA: IEEE Press, 1994.

[147] H. Friis, “A Note on a Simple Transmission Formula,” *Proceedings of the IRE*, vol. 34, no. 5, pp. 254–256, May 1946. Available: https://doi.org/10.1109/JRPROC.1946.234568

[148] “49 CFR 571.108 – Standard No. 108; Lamps, reflective devices, and associated equipment.” Oct. 2023. Available: https://www.ecfr.gov/current/title-49/part-571/section-571.108

[149] “29 CFR Part 1926 Subpart D – Occupational Health and Environmental Controls,” Nov. 2023. Available: https://www.ecfr.gov/current/title-29/part-1926/subpart-D

[150] T. Chiba, “Spot Dancing of the Laser Beam Propagated Through the Turbulent Atmosphere,” *Applied Optics*, vol. 10, no. 11, p. 2456, Nov. 1971. Available: https://doi.org/10.1364/AO.10.002456

[151] B. T. Phong, “Illumination for computer generated pictures,” *Communications of the ACM*, vol. 18, no. 6, pp. 311–317, June 1975. Available: https://doi.org/10.1145/360825.360839

[152] S. Woo, S. Lee, J. Yoo, and J. Kim, “Improving Color Constancy in an Ambient Light Environment Using the Phong Reflection Model,” *IEEE Transactions on Image Processing*, vol. 27, no. 4, pp. 1862–1877, Apr. 2018. Available: https://doi.org/10.1109/TIP.2017.2785290

[153] F. M. Alsalami, Z. Ahmad, P. A. Haigh, O. C. L. Haas, and S. Rajbhandari, "The Statistical Temporal Properties of Vehicular Visible Light Communication Channel," in *2020 12th International Symposium on Communication Systems, Networks and Digital Signal Processing (CSNDSP)*. Porto, Portugal: IEEE, July 2020, pp. 1–5. Available: https://doi.org/10.1109/CSNDSP49049.2020.9249538

[154] M. S. Islim and H. Haas, "An investigation of the solar irradiance effect on visible light communications," in *2017 IEEE 28th Annual International Symposium on Personal, Indoor, and Mobile Radio Communications (PIMRC)*. Montreal, Canada: IEEE, Oct. 2017, pp. 1–6. Available: https://doi.org/10.1109/PIMRC.2017.8292621

[155] Y. Wang, X. Chen, and Y. Xu, "Transmitter for 1.9 Gbps phosphor white light visible light communication without a blue filter based on OOK-NRZ modulation," *Optics Express*, vol. 31, no. 5, p. 7933, Feb. 2023. Available: https://doi.org/10.1364/OE.476911

[156] S. Ammar, O. Amin, M. Alouini, and B. Shihada, "Design and Analysis of LCD-Based Modulator for Passive Sunlight Communications," *IEEE Photonics Journal*, vol. 14, no. 5, pp. 1–17, Oct. 2022. Available: https://doi.org/10.1109/JPHOT.2022.3200833

[157] H. Wang, L. liu, and C. Lu, "CPLC: Visible Light Communication based on Circularly Polarized Light," *Procedia Computer Science*, vol. 131, pp. 511–519, 2018. Available: https://doi.org/10.1016/j.procs.2018.04.247

[158] Y. Yang, C. Yeh, S. Liaw, C. Chow, W. Hsu, and B. Wang, "Analysis and Investigation of Dual-Polarized Color LED Based Visible Light Communication System," *Photonics*, vol. 8, no. 6, p. 210, June 2021. Available: https://doi.org/10.3390/photonics8060210

[159] Y. Tang, X. Ding, Z. Li, C. Shao, Z. Huang, and S. Liang, "Crosstalk-Free MIMO VLC Using Two Orthogonal Polarizations Multiplexed Large FOV Fluorescent Antennas," *IEEE Photonics Technology Letters*, vol. 35, no. 23, pp. 1271–1274, Dec. 2023. Available: https://doi.org/10.1109/LPT.2023.3312327

[160] M. Uysal, Z. Ghassemlooy, A. Bekkali, A. Kadri, and H. Menouar, "Visible Light Communication for Vehicular Networking: Performance Study of a V2V System Using a Measured Headlamp Beam Pattern Model," *IEEE Vehicular Technology Magazine*, vol. 10, no. 4, pp. 45–53, Dec. 2015. Available: https://doi.org/10.1109/MVT.2015.2481561

[161] A. Chen, H. Wu, Y. Wei, and H. Tsai, "Time variation in vehicle-to-vehicle visible light communication channels," in *2016 IEEE Vehicular Networking Conference*

(VNC). Columbus, OH, USA: IEEE, Dec. 2016, pp. 1–8. Available: https://doi.org/10.1109/VNC.2016.7835926

[162] B. Aly, M. Elamassie, and M. Uysal, "Vehicular Visible Light Communication with Low Beam Transmitters in the Presence of Vertical Oscillation," *IEEE Transactions on Vehicular Technology*, pp. 1–12, 2023. Available: https://doi.org/10.1109/TVT.2023.3253762

[163] X. Liu, H. Zhang, Q. Ma, X. Zhao, and C. Di, "Channel Performance Analysis of Visible Light Communication Technology in the Internet of Vehicles," *Photonics*, vol. 10, no. 11, p. 1197, Oct. 2023. Available: https://doi.org/10.3390/photonics10111197

[164] A. L. Rodrigues Gonçalves, D. Alves De Lima, and Á. Maia, "Visible Light Communication Applied to Low Cost Embedded Systems," *IEEE Latin America Transactions*, vol. 22, no. 1, pp. 15–21, Jan. 2024. Available: https://doi.org/10.1109/TLA.2024.10375734

[165] Z. White, D. Barber, M. Tummala, and J. McEachen, "A Transmit Diversity Scheme for Multi-pulse Pulse Position Modulated Visible Light Communications," in *MILCOM 2022 - 2022 IEEE Military Communications Conference (MILCOM)*. Rockville, MD, USA: IEEE, Nov. 2022, pp. 723–728. Available: https://doi.org/10.1109/MILCOM55135.2022.10017940

[166] "Performance leap in light technology." Dec. 2022. Available: https://newsroom.porsche.com/en/2022/innovation/porsche-led-main-headlights-with-hd-matrix-beam-light-technology-30770.html

[167] J. C. Zwinkels, E. Ikonen, N. P. Fox, G. Ulm, and M. L. Rastello, "Photometry, radiometry and 'the candela': evolution in the classical and quantum world," *Metrologia*, vol. 47, no. 5, pp. R15–R32, Oct. 2010. Available: https://doi.org/10.1088/0026-1394/47/5/R01

[168] J. Zwinkels *et al.*, "Mise en pratique for the definition of the candela and associated derived units for photometric and radiometric quantities in the International System of Units (SI)," *Metrologia*, vol. 53, no. 3, pp. G1–G1, June 2016. Available: https://doi.org/10.1088/0026-1394/53/3/G1

[169] Y. Zong, "From candle to candela," *Nature Physics*, vol. 12, no. 6, pp. 614–614, June 2016. Available: https://doi.org/10.1038/nphys3787

[170] J. Chen, W. Cranton, and M. Fihn, Eds., *Handbook of Visual Display Technology*. Berlin, Heidelberg: Springer Berlin Heidelberg, 2012. Available: https://doi.org/10.1007/978-3-540-79567-4

[171] Consultative Committee for Photometry and Radiometry, “Report of the 20th meeting (17-18 September 2009) to the International Committe for Weights and Measures,” Bureau International des Poids et Mesures, Sèvres, France, Rep., Apr. 2011. Available: https://www.bipm.org/documents/20126/27313531/20th+meeting.pdf/bcb67cf5-6a1e-11ab-3280-d999f50a4ee8

[172] C. Pickle, “Assessment of Frequency Modulated Outdoor Visible Light Communication,” M.S. thesis, Naval Postgraduate School, Monterey, CA, USA, Sep. 2023.

[173] T. Komine and M. Nakagawa, “Integrated system of white LED visible-light communication and power-line communication,” *IEEE Transactions on Consumer Electronics*, vol. 49, no. 1, pp. 71–79, Feb. 2003. Available: https://doi.org/10.1109/TCE.2003.1205458

[174] M. Hord and P. Makin, “FemtoBuck LED Driver,” Aug. 2022. original-date: 2014-05-13T22:20:48Z. Available: https://github.com/sparkfun/FemtoBuck

[175] Android Open Source Project, “CameraX overview.” https://developer.android.com/training/camerax (acessed Feb. 2, 2023).

[176] Dev47Apps, “DroidCam.” https://www.dev47apps.com/ (accessed July 2, 2023).

[177] Dev47Apps, “DroidCam OBS Android Source Code,” private communication, Sep. 2022.

[178] “Tinkercad | From mind to design in minutes.” https://www.tinkercad.com/ (accessed July 12, 2023).

[179] “UltiMaker Cura.” https://ultimaker.com/software/ultimaker-cura/ (accessed July 12, 2023).

[180] Y. Shiraki *et al.*, “A Demodulation Method Using a Gaussian Mixture Model For Unsynchronous Optical Camera Communication With on-off Keying,” *Journal of Lightwave Technology*, vol. 39, no. 6, pp. 1742–1755, Mar. 2021. Available: https://doi.org/10.1109/JLT.2020.3043046

[181] T. P. Lee, “Effect of Junction Capacitance on the Rise Time of LED’s and on the Turn-on Delay of Injection Lasers,” *Bell System Technical Journal*, vol. 54, no. 1, pp. 53–68, Jan. 1975. Available: https://doi.org/10.1002/j.1538-7305.1975.tb02825.x

THIS PAGE INTENTIONALLY LEFT BLANK

Initial Distribution List

1. Defense Technical Information Center
   Fort Belvoir, Virginia

2. Dudley Knox Library
   Naval Postgraduate School
   Monterey, California

DUDLEY KNOX LIBRARY

NAVAL POSTGRADUATE SCHOOL

WWW.NPS.EDU

WHERE SCIENCE MEETS THE ART OF WARFARE